Title
Quantum Phenomena in Interacting Many-Body Systems: Topological Protection, Localization, and Non-Fermi Liquids

Author
Bahri, Yasaman

Publication Date
2017

Peer reviewed|Thesis/dissertation

Quantum Phenomena in Interacting Many-Body Systems: Topological Protection, Localization, and Non-Fermi Liquids

by

Yasaman Bahri

A dissertation submitted in partial satisfaction of the

requirements for the degree of

Doctor of Philosophy

in

Physics

in the

Graduate Division

of the

University of California, Berkeley

Committee in charge:

Professor Ashvin Vishwanath, Chair
Professor Joel Moore
Professor K. Birgitta Whaley

Spring 2017

Quantum Phenomena in Interacting Many-Body Systems: Topological Protection, Localization, and Non-Fermi Liquids

Yasaman Bahri

Abstract

Quantum Phenomena in Interacting Many-Body Systems: Topological Protection, Localization, and Non-Fermi Liquids

by

Yasaman Bahri

Doctor of Philosophy in Physics

University of California, Berkeley

Professor Ashvin Vishwanath, Chair

This dissertation establishes and investigates new phenomena in diverse interacting many-body quantum systems guided by three distinct, but complementary, themes: (i) symmetry and topology, (ii) localization, and (iii) non-Fermi liquids.

The first theme concerns how the interplay of symmetry and topology can offer robust protection for a many-body system. We investigate low-dimensional quantum fermionic models from a general structural perspective. These phases can exhibit fractionalized Majorana zero-energy modes on their boundary. We devise experimentally relevant nonlocal measurements that can be used to detect these topological phases. While our primary focus is on quantum systems, topologically protected behavior can arise in classical mechanical models as well. We extend a recent connection between the topological band theory of electrons and classical physics by proposing a mechanical analogue of a topological nodal semimetal.

The second theme concerns that of many-body localization. We demonstrate that the combination of localization, symmetry, and topology can have radical consequences for quantum systems at high energies, such as the existence of protected gapless boundary modes. We show that, even at these high energies, quantum information can be preserved, and quantum coherence recovered. Quantum coherent dynamics in this regime is unexpected and of great interest for quantum computation.

The third direction in our study of interacting many-body systems concerns non-Fermi liquids. We construct a non-Fermi liquid by bringing together a spin-orbit coupled Fermi surface and fluctuating magnetic order. Using newly developed analytic tools for strongly coupled systems, we demonstrate the stability of the non-Fermi liquid to ordering. This identifies an experimentally accessible candidate for exploring physics that lies beyond Fermi liquid theory.

To my teachers

Contents

Acknowledgments

I would first like to express my deepest gratitude to my advisor Ashvin Vishwanath for his mentorship. It has been a privilege to be his student. It goes without saying that Ashvin is an exceptionally creative and deep thinker with an overabundance of very interesting research ideas. I have been and remain continually amazed at how Ashvin seeks out and targets the most interesting and important attributes of any problem, always clearly distilling new physics from the old. He is also very generous and humble. His attitude towards research and discovery, as well as his taste in problems and his emphasis on inventive work, have been influential beyond measure. Ashvin fostered and led a highly stimulating research environment at Berkeley during my time in graduate school. I will always be grateful to him for a singularly rewarding experience and his unfailing support and encouragement of me.

Several individuals also played important roles in the topics of this dissertation. I would like to thank Ehud Altman for many interesting discussions and an enjoyable collaboration, not to mention his thoughtful and considerate guidance over time. In particular, Ehud brought to Berkeley new ideas and problems on many-body localization and quantum dynamics during his extended stay in 2013, leading to some of the material contained herein. I thank Andrew Potter for the opportunity to collaborate on a project on non-Fermi liquids. Andrew is a gifted researcher with a broad knowledge of condensed matter, and through this project I was introduced to field theoretic developments for strongly coupled systems. I would also like to thank Adrian Po, a most curious and perceptive collaborator, for a joint project on topological mechanical models.

I thank Birgitta Whaley and Joel Moore for serving on my dissertation committee, as well as for expressing interest in my work and in my scientific development.

I thank all those who passed through Berkeley's condensed matter theory group. Among current and former postdocs and visitors, I particularly appreciate interactions with Andrew Potter, Sid Parameswaran, Frank Pollmann, Norman Yao, Tarun Grover, Maksym Serbyn, Snir Gazit, Xie Chen, Yuan-Ming Lu, and Lukasz Fidkowski. Amongst fellow students, I would particularly like to thank Itamar Kimchi, Michael Zaletel, Gil Young Cho, and Charles Xiong.

It is a pleasure to especially thank three individuals – Adrian Po, Philipp Dumitrescu, and Haruki Watanabe – who kindly shared their insights and understanding on many occasions. Their presence made my research experience quite a rich and memorable one.

Looking farther back, I am indebted to Joel Moore for an early and rare research opportunity during my final undergraduate year at Berkeley. Joel is a patient teacher, and I learned much through that experience. It was also my introduction to quantum tensor networks, which lie at an intersection of quite exciting ideas. That research experience paved

the way for subsequent opportunities in condensed matter theory, which I very much wanted to continue in, following graduation. I could not have chosen a more perfect field than this one, and I thank Joel for having played the pivotal role in that.

I would like to thank professors in the Physics Department at Berkeley whose teaching during my undergraduate years was influential during my physics studies: Robert Littlejohn, Dung-Hai Lee, Martin White, and Steven Louie.

Finally, I give thanks to my family for seeing me through many years of education. To my mother for her involvement in my learning during the early years. To my younger brother for his encouragement and steadfast good humor, especially during my time in graduate school.

This dissertation is dedicated to all the teachers I have had throughout my life, and especially those who, directly or indirectly, aided or encouraged me in the pursuit of physics.

Chapter 1

Introduction

The many-body interacting systems found in condensed matter settings are a fascinating playground for theoretical study. A traveler to this domain discovers some of the richest behavior in the physical world that is nonetheless describable by a rather unified body of theory. Such a balance between diversity and complexity, on the one hand, and theory that is both tractable and powerfully predictive, on the other, is a rare find in the scientific world.

This dissertation, like condensed matter itself, is rather broad in scope. Each of the subsequent chapters here covers a distinct direction of current interest in the field. The focus is almost entirely on quantum systems. There are a few overarching themes that we wish to highlight because they play a fundamental role, both in this dissertation and more broadly:

Entanglement

Quantum entanglement lies at the heart of many problems. Entanglement has shed a great deal of light on why some states are similar and some are different, by allowing us to abstract away particularities of a wavefunction – such as the degrees of freedom that it is composed of, or the exact amplitudes of an expansion – and understand instead the bare structural complexity, the skeleton of quantum states. As we will survey in this dissertation, entanglement plays a fundamental role in how a quantum system thermalizes; it provides an underlying classification for quantum phases; and an understanding of it allows us to identify correct parameterizations for large classes of quantum states.

Identifying the "Right" Variables

Teasing out the variables that simplify a problem is a necessity across all of science and mathematics: in interacting many-body systems, however, the importance of this seems especially stark. Changes in variables, and with it, perspective, are the norm; their identification, in part, is an art. We think of quasiparticles, collective excitations, dualities, novel composite particles, fractionalized degrees of freedom, disorder variables in an ordered setting, and bosonization of a problem, to name just a small sample. Often the natural variables are

not the microscopic ones. Consider the simple fermionic chain we will introduce in Chapter 2. One can identify the nontrivial physics, namely that one is dealing with a symmetry-protected topological phase, by thinking in terms of Majorana degrees of freedom, instead of complex fermions, and considering bond-centered, rather than site-centered, pairing of these variables. With the chapters on topological phases and localization, we will see that we can indeed identify new variables under which a problem simplifies. Frequently we do not have direct access to these "right" variables in measurements. Our example of a non-Fermi liquid, however, is an instance where we do not have yet a simple description or effective theory at low energies.

Dichotomy between Locality and Nonlocality

Historically, it makes sense that the framework of symmetry-breaking orders was investigated thoroughly first: our experimental probes are local, allowing for relatively easier detection of local orders such as magnetism or charge- and spin-density waves. All physical Hamiltonians must have some form of locality, but nonetheless, with the right combinations of interactions, their particles can be arranged in a pattern which seems rather disjoint from this constraint. Topology, as a subject, is by construction concerned with global properties. Likewise, the topological aspects of quantum matter are inherently tied with nonlocality; for instance, one may need a nonlocal change of variables for the topological order to be made apparent.

While these motifs emerge across many quantum condensed matter systems, let us introduce the three primary areas of focus within this dissertation.

Topology as a New Paradigm

Notions borrowed from topology have enriched our understanding of quantum phases of matter in recent years. The distinction between phases was believed to be mostly described by Landau's theory of symmetry-breaking orders. The discovery of the fractional quantum Hall effect, topological quantum spin liquids, and topological insulators – among others – made it clear that the separation between quantum phases can be more subtle. Indeed, there are many different kinds of quantum topological orders, some more exotic than others. In this dissertation, we will be interested in symmetry-protected topological order, which requires both symmetry and topology for interesting behavior. Such systems exhibit protected zero-energy states localized on their boundary and are featureless in their bulk. It might naively seem as though the edge physics is the only manifestation of the nontrivial topological aspects of the system, but this is untrue: there is hidden order in the bulk which can be measured if one has access to nonlocal probes, a subject we will return to. We will also explore a new connection between the topological physics of electron systems and a mechanical model obeying Newtonian equations of motion. Evidently, distinctions arising from topology bear consequences for the classical realm as well.

Localization in Interacting Many-Body Systems

We still lack a full understanding of the combined effects of disorder and interactions on a quantum system. Many-body localization, as it is termed, began as a study of the fate of single-particle localization under the introduction of weak electron interactions. It was shown that localization could indeed be robust, suggesting that the many-body case is, in some ways, a partial continuation or "dressed" version of the noninteracting one. Applying a perturbative viewpoint here is, however, subtle, as it involves states and degenerate energy levels throughout the spectrum, where naively there is no obvious notion of a protecting energy gap. Furthermore, the interactions do effect important distinctions with the noninteracting problem.

In fact, many-body localization is more fundamental than might naively seem. It defines a regime in which quantum systems cannot serve as a thermalizing bath for themselves. This connects it to the fundamental tenets of quantum statistical mechanics, such as ergodicity.

A profound consequence of many-body localization is that it can, surprisingly, offer protection to quantum order. In this dissertation, we will consider a class of systems in which many-body localization is combined with symmetry and topology to obtain protected quantum behavior in regimes hitherto believed to be inaccessible.

A partial understanding of a class of localized systems comes from recognizing that they have a "hidden" simplicity in a different set of variables. However, unlike the topological setting, this simplicity can be accessed using local probes.

Non-Fermi Liquids

Adiabatic continuity can extend the reach of notions that originate in a simple or noninteracting theory. Fermi liquid theory is perhaps the most well-known example of this. We continue to study when and how Fermi liquid theory breaks down, and what kind of physics might take its place. Still, a framework which can describe gapless phases outside this domain in some partially unified way remains elusive. Tackling the problem theoretically in many cases is still a challenging task. Much work on non-Fermi liquids remains to be done, but progress on this problem appears crucial for understanding many important quantum phases.

Diverse Approaches

A simple point, well worth making, is that theoretical investigation of diverse physical phenomena requires an equally diverse set of tools and approaches. In this dissertation, we are not tied to a particular method but use a combination of theoretical arguments, exactly solvable models and perturbations about them, and numerical methods (such as exact diagonalization on small systems). We further rely on dualities and nonlocal change of variables, as well as modern field theoretic methods, which can be controlled in a certain regime but ultimately may be uncontrolled when extended to the domain of physical interest. A guid-

ing approach has been to pinpoint new physics, where relevant, through a combination of interesting ingredients and explicit construction of models.

Layout

Each of the following chapters is meant to be self-contained, with an initial introduction to the topic and review of the relevant prior works before discussing our own advances. We begin the dissertation in Chapter 2 by looking at symmetry-protected topological phases in quasi-one-dimensional systems of spinless fermions. When topologically nontrivial, the surface states can be unusual, consisting of a "half" of a complex fermion – a Majorana fermion – on a boundary. We tackle the question of how the hidden, topological order of such phases can be detected in the bulk, given that they are featureless with respect to local probes. This problem is experimentally relevant because of recent developments in nonlocal measurements in ultracold atomic systems.

In Chapter 3, we combine elements of many-body localization, symmetry, and topology in a class of models and demonstrate that it can have radical consequences for quantum behavior in new regimes. We can store quantum information in a many-body localized topological phase with high energy density (in a loose sense, at "infinite temperature") and show that it can be robustly manipulated and retrieved. This opens up a new direction for exploring quantum coherent dynamics at high energies – involving highly excited states – and is both of theoretical interest in condensed matter, as well as of practical interest for quantum computation and simulation.

In Chapter 4, we discuss our work in constructing a non-Fermi liquid out of a combination of simple ingredients, by bringing together a spin-orbit coupled Fermi surface and fluctuating magnetic order. Coupling a Fermi surface to gapless bosonic degrees of freedom can sometimes lead to non-Fermi liquid behavior. However, the ultimate fate of the coupled system may be altogether different at low energies due to interactions mediated by the bosons. Our proposal is unique and of experimental interest in that the non-Fermi liquid appears stable within our calculations. We rule out the most relevant instabilities with a field theoretic analysis relying on a dual expansion in two parameters.

Finally, in Chapter 5, we explore a recently made connection between mechanical models, consisting of lattices of masses coupled by springs, with the topological band theory of electrons, a direction known as "topological mechanics." We construct the first example of a mechanical model whose spectrum hosts a bulk gapless node that is protected by topology. This serves as a classical analogue of a topological nodal semimetal.

Chapter 2

Nonlocal Order Parameters for Quasi-1D Phases with Majorana Edge Modes

In the past several decades, a new paradigm based on topology and entanglement has emerged in the study of quantum systems. It is possible for a quantum system to be featureless with respect to local probes, and hence to lie outside the scheme of spontaneous symmetry-breaking order, yet nonetheless display certain hidden patterns of order. There are a myriad of such *topological phases* and assembling them into a unified framework is a subject of ongoing work. A major distinction is made between *symmetry-protected topological order* and *intrinsic topological order*. The latter class can be associated with fractional excitations and a robust ground state degeneracy on manifolds with nontrivial topology. In the former case, nontrivial behavior arises only in the presence of certain symmetries which protect the ground state by restricting the deformations that can be made to the Hamiltonian. These *symmetry-protected topological phases* (SPTs) are the primary interest in this chapter.

Our work [1] examines specific classes of SPTs in low dimensions and devises simple order parameters that can be used to identify them. These are necessarily nonlocal order parameters (NLOPs), requiring macroscopically many simultaneous measurements of local operators, because the distinction between the phases is nonlocal. Before diving in, we first illustrate symmetry-protected topological order with the Haldane phase of odd-integer spin chains, a prototypical example of a one-dimensional (1D) SPT. We then discuss efforts to classify all possible 1D SPTs on general grounds. The insight gained from the classification aids in devising NLOPs in low dimensions. Our work, targeting NLOPs for interacting spinless fermion topological superconductors with Majorana edge states, begins in Section 2.3.

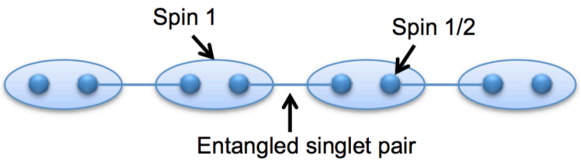

Figure 2.1: Depiction of the AKLT wavefunction for the SPT phase of a spin-1 chain. Reproduced from [2].

2.1 Symmetry-Protected Topological Phases

We illustrate the key characteristics of SPTs with the Haldane phase [3–6] of spin-1 chains. It is instructive to examine an exactly-solvable Hamiltonian, presented by Affleck, Kennedy, Lieb, and Tasaki (AKLT) [5] in 1987, whose ground state is in this phase. It consists of spin-1 biquadratic interactions,

$$H_{AKLT} = \frac{1}{2}\sum_i \left[\mathbf{S}_i \cdot \mathbf{S}_{i+1} + \frac{1}{3}(\mathbf{S}_i \cdot \mathbf{S}_{i+1})^2 + \frac{2}{3}\right] \tag{2.1}$$

$$= \sum_i \mathcal{P}_2(i, i+1). \tag{2.2}$$

$\mathcal{P}_2(i, i+1)$ is an operator projecting the total spin $\mathbf{S}^{tot}_{i,i+1} = \mathbf{S}_i + \mathbf{S}_{i+1}$ of neighboring lattice sites i and $i+1$ onto the spin-2 sector. The exact AKLT ground state can be constructed as follows. Consider two virtual spin-1/2 degrees of freedom, $|\sigma^{z,i}_R\rangle, |\sigma^{z,i}_L\rangle$, labeled left L and right R, per lattice site. Adjacent spin-1/2's on neighboring sites are combined to form a spin singlet; to ensure the result describes a spin-1 wavefunction, it is then projected with operator P^i_1 onto the spin-1 sector per lattice site. This can be written

$$|\psi_{AKLT}\rangle = \prod_i P^i_1 \prod_j \left(|\uparrow^j_R\rangle |\downarrow^{j+1}_L\rangle - |\downarrow^j_R\rangle |\uparrow^{j+1}_L\rangle \right) \tag{2.3}$$

and is depicted in Figure 2.1. We can observe that this is a ground state by looking at two neighboring lattice sites, consisting of four virtual spin-1/2s. The total spin on this pair cannot be greater than one because of the presence of the spin singlet on the bond; the remaining spin-1/2s at best can give rise to a total spin of one, and hence the AKLT state is annihilated by the spin-2 projection operator. It is a unique ground state on a closed system, is gapped, and has exponentially decaying few-point (local) correlation functions. On an open chain, a manifestation of the symmetry-protected topological order will be the existence of edge states: two unpaired virtual spin-1/2s, giving rise to a four-fold degeneracy. The Haldane SPT can by protected by any one of several symmetries: the dihedral group (a $\mathbb{Z}_2 \times \mathbb{Z}_2$ symmetry) of π rotations about the x, y, z axes, time-reversal, or a bond-centered inversion symmetry [7, 8].

Classification of 1D Gapped Quantum Phases

Efforts to completely classify quantum phases of matter, encompassing systems with some combination of intrinsic topological order, symmetry-protected topological order, and broken-symmetry order, have been underway in recent years. Important achievements thus far include the classification of free fermion systems [9, 10], an understanding of interaction effects in certain symmetry classes [11–18], and general methods for many of the symmetry-protected bosonic or fermionic systems with interactions [19–27]. Obtaining a general classification requires identifying the right mathematical structures, and it has been necessary to bring in areas of mathematics, such as group cohomology, that are new to condensed matter physics.

One-dimensional gapped quantum phases were the first to be classified completely [19, 20, 23] because matrix-product states provide a parameterization for ground states of gapped local Hamiltonians. While the literature has primarily discussed bosonic phases, fermionic phases can be incorporated because of the correspondence between bosons and fermions in one dimension [20].

Let us first discuss some properties of matrix-product states before turning to the classification of 1D SPTs, following [19, 20]. Consider an L-site chain with local Hilbert space of dimension d spanned by $|i\rangle$ on each site. Any state $|\psi\rangle$ can be written as a product of matrices [28–30],

$$|\psi\rangle = \sum_{i_1 i_2 ... i_L} c_{i_1 i_2 ... i_L} |i_1 i_2 ... i_L\rangle \tag{2.4}$$

$$= \sum_{i_1 i_2 ... i_L} \mathrm{tr}(A_{i_1} A_{i_2} ... A_{i_L}) |i_1 i_2 ... i_L\rangle. \tag{2.5}$$

A_{i_k} is a $\chi \times \chi$ matrix for each $i_k = 1, ..., d$ and hence contains $d \cdot \chi^2$ parameters.[1] For ground states of gapped, local Hamiltonians, this will amount to only $\mathcal{O}(\mathrm{poly}(d))$ many parameters in total. An alternative way of writing which we will utilize later is

$$|\psi\rangle = \sum_{i_1 i_2 ... i_L} \mathrm{tr}(\Gamma_{i_1} \Lambda \Gamma_{i_2} \Lambda ... \Gamma_{i_L} \Lambda) |i_1 i_2 ... i_L\rangle, \tag{2.6}$$

where $A_{i_k} = \Gamma_{i_k} \Lambda$ and Λ is a $\chi \times \chi$ nonnegative diagonal matrix. If the matrix elements of A_i are $A_{i,\alpha\beta}$, we will refer to i as the physical index and α, β as bond indices.

The transfer tensor $\mathbb{T}$ with elements

[1] We have dropped the site dependence of A_{i_k} for notational simplicity. The notation would be exact for a translationally invariant state. We have also assumed periodic boundary conditions; open boundary conditions can be imposed by capping with appropriate vectors at each end of the matrix product rather than taking the trace.

$$\mathbb{T}_{\alpha\gamma,\beta\delta} = \sum_i A_{i,\alpha\beta} \cdot A^*_{i,\gamma\delta} \tag{2.7}$$

contains much information about the quantum phase of $|\psi\rangle$. Two matrix-product states with the same $\mathbb{T}$ tensor are equivalent up to unitary transformations on the physical index. The tensor can be viewed in two ways. If the indices are grouped together as (α, γ) and (β, δ), $\mathbb{T}$ plays the role of a transfer matrix: it appears in expectation values of observables, and its spectral properties determine the behavior of multipoint correlation functions at long distances. On the other hand, $\mathbb{T}$ viewed as a matrix with indices (α, β) and (γ, δ) is positive semidefinite, and given a tensor $\mathbb{T}$, a spectral decomposition based on this grouping of indices is a simple way to recover component matrices $A_{i,\alpha\beta}$, up to unitary equivalence on the physical index [19].

The symmetry of a state $|\psi\rangle$ constrains the matrices A_i to transform in a particular way. Suppose we have an onsite symmetry group G, one consisting of symmetries g acting on lattice sites. Let $\Sigma(g)$ be a linear matrix representation of g. When the matrix-product state is injective, the matrices must satisfy

$$\sum_j \Sigma(g)_{ij} A_j = \alpha(g) U_g^\dagger A_j U_g \tag{2.8}$$

for $\chi \times \chi$ unitary matrices U_g which contract with A_i on the bond indices, and $\alpha(g)$ is a 1D representation of G. This transformation rule ensures that that state $|\psi\rangle$ will be reproduced up to a phase when the symmetry is applied globally, since neighboring $U, U^\dagger$ contributions will cancel. Let us absorb $\alpha(g)$ into $\Sigma(g)$ to form a different representation of G. The group composition law of G requires that $\Sigma(g_1)\Sigma(g_2) = \Sigma(g_1 g_2)$ for any two symmetries g_1, g_2, i.e.

$$\sum_{jk} \Sigma(g_1)_{ij} \Sigma(g_2)_{jk} A_k = U_{g_2}^\dagger U_{g_1}^\dagger A_i U_{g_1} U_{g_2}, \tag{2.9}$$

$$\sum_j \Sigma(g_1 g_2)_{ij} A_j = U_{g_1 g_2}^\dagger A_i U_{g_1 g_2}, \tag{2.10}$$

and hence $U_{g_1 g_2} = \omega(g_1, g_2) U_{g_1} U_{g_2}$, where $\omega(g_1, g_2) \in \mathbb{C}$. That is, on the bond indices, the group composition law is reproduced by U_g up to a complex number ω termed the *factor system*. This is the definition of a projective representation. Some projective representations, however, are related to each other in trivial ways. For instance, note that if U_g corresponds to factor system ω, a representation satisfying $U'_g = \beta(g) U_g$ for $\beta(g) \in \mathbb{C}$ will have a factor system ω' that is dependent on ω and derivable as

$$\omega'(g_1, g_2) = \frac{\beta(g_1 g_2)}{\beta(g_1)\beta(g_2)} \omega(g_1, g_2). \tag{2.11}$$

The class of inequivalent projective representations, ones that are distinct even with such redefinitions, is the second cohomology group of G, denoted $H^2(G, U(1))$.

The phase of a quantum system can be revealed by a renormalization group transformation [31] on the ground state which removes local entanglement via local unitary transformations. Coarse-graining is accomplished by forming a block transfer tensor $\tilde{\mathbb{T}}$ for multiple neighboring sites (by contraction on all physical indices and the internal bond indices). To find new constituent matrices $\tilde{A}_{\tilde{i}}$, the block tensor can be diagonalized,

$$\mathbb{T}_{\alpha\gamma,\beta\delta} = \sum_{\tilde{i}} \lambda_{\tilde{i}} V_{\tilde{i},\alpha\beta} V^*_{\tilde{i},\gamma\delta} \tag{2.12}$$

and, retaining only eigenvalues $\lambda_{\tilde{i}} > 0$, we set $\tilde{A}_{\tilde{i}} = \sqrt{\lambda_{\tilde{i}}} V_{\tilde{i},\alpha\beta}$. By dropping components where $\lambda_{\tilde{i}} = 0$, only the physical dimensions which are necessary for describing the entanglement of the block and system have been retained [19, 20]. This procedure can be iterated until fixed-point matrices $A_i^{(\infty)}$ are obtained. Two states will be in the same phase if and only if their fixed-point states can be transformed into each other by local unitary transformations. To obtain a classification of SPTs, the renormalization procedure must further respect the symmetries under consideration [19, 20].

With the fixed-point form of the matrix-product state obtained under symmetry-preserving renormalization, it is possible to show that states with different factor systems, neglecting redefinitions, cannot be transformed into each other with any symmetry-preserving local unitary transformation. Likewise, states with the same factor system can. Hence, 1D gapped bosonic SPTs are in one-to-one correspondence with the group $H^2(G, U(1))$ [19, 20].

Let us illustrate in physical terms the form of the fixed-point given by $A^{(\infty)}$. The effective degree of freedom, formerly indexed by i, on a renormalized site will split into two degrees of freedom indexed by i_L and i_R; the fixed-point state will consist of a product of entangled pairs where the right degree of freedom on site k is entangled with the left degree of freedom on site $k+1$, analogous to the pairing in the AKLT wavefunction. The fixed-point form reveals that an SPT is not necessarily transformable to a product state on the renormalized sites. Rather, it appears as a product state when the sites are redefined to be on the bonds, for instance, which on an open chain would reveal unentangled degrees of freedom. One can show that these fractional degrees of freedom transform *projectively* under an application of the onsite symmetry, with opposite factor systems $\omega, -\omega$ so that together they yield a linear representation, as in Figure 2.2.

We also point out a closely related approach [13] for classifying 1D gapped symmetric phases which is formulated so as to address fermionic SPTs directly. Consider partitioning a closed 1D chain with ground state $|\psi\rangle$ into a segment S which shares two boundaries with the remainder of the system, the environment E. The reduced density matrix on the segment $\rho_S = \mathrm{tr}_E |\psi\rangle\langle\psi|$ can be reinterpreted in terms of an entanglement Hamiltonian $\mathcal{H}_S$ defined by $\rho_S \equiv e^{-\mathcal{H}_S}$. Upon examining the symmetry transformation properties of low-lying entanglement energy eigenstates (the most likely states for S in the ground state $|\psi\rangle$),

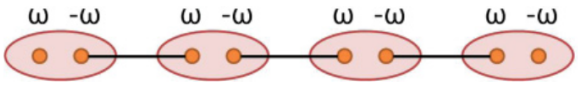

Figure 2.2: Fixed-point representation of a 1D SPT phase with an onsite symmetry group. Entangled pairs are formed by fractionalized degrees of freedom across neighboring renormalized sites. Each fractional degree of freedom transforms projectively under the symmetry, with factor system ω or $-\omega$. Reproduced from [32].

[13] argued that a transformation on this subspace can be approximately represented as a product of two local operators, each acting at one boundary of the segment S. Consequently, symmetry operators will fractionalize in this subspace, with each fraction essentially forming a projective representation of the symmetry.

In 1D, one can choose whether to work in bosonic or fermionic variables. To classify fermionic phases with symmetry G, one can map the system to a bosonic one, determine the nature of the order (SPT and spontaneously broken symmetries), and then map back to fermions, as described in [20].

2.2 Nonlocal Order Parameters

Thus far, we have discussed the nature of symmetry-protected topological order, but the main focus of this chapter is on the detection of this order using NLOPs. We first review some prior work, beginning with the well-known string order discovered for the Haldane phase in spin chains [33, 34, 6]. This example represents a class of NLOP with several features. It is constructed from a product of local, physical operators. It yields a continuously varying value within an SPT phase because it depends not just on a topological fingerprint but also on extraneous information present in the wavefunction. A NLOP constructed in this way has its advantages and disadvantages: it is simple to write down and to measure but may not be robust.

In contrast, the group cohomology classification yields a mathematically precise definition of an SPT; in many respects, it may be more ideal to design a NLOP which detects only this signature, and nothing else, directly. Such NLOPs return fixed values throughout an entire phase and are more robust, in the sense that they will not accidentally vanish or acquire small values. We will not discuss these further but refer the reader to [35–38]. In our work [1], we focused on devising NLOPs of the conventional type because we are primarily motivated by their use in experiments with ultracold atoms (Section 2.5), for which nonlocal measurements of this type have recently been demonstrated[39].

String Order

The string order parameter (OP)

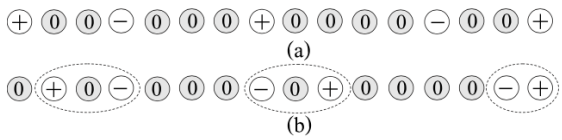

Figure 2.3: The hidden order of particle (+) and holes (−), about average filling (0) of the (a) Haldane insulating and (b) Mott insulating phases of 1D lattice bosons. Reproduced from [40].

$$\mathcal{O}(i,j) = -\left\langle S_i^\alpha \exp\left[i\pi \sum_{k=i+1}^{j-1} S_k^\alpha\right] S_j^\alpha \right\rangle \tag{2.13}$$

was found [33, 34, 6] to take on a finite value as $|i-j| \to \infty$ for $\alpha = x, y, z$ in the $\mathbb{Z}_2 \times \mathbb{Z}_2$ symmetry-protected Haldane phase. It measures a hidden order that is apparent in the AKLT wavefunction and persists away from the exactly-solvable point: in the spin-1 variables, the wavefunction consists of a superposition of patterns of antiferromagnetically ordered spins $S^z = \pm 1$ interspersed with arbitrary lengths of $S^z = 0$ spins. In fact, the string OP form, Eq. 2.13, can be derived [34, 6] by applying a nonlocal transformation to the spins such that, in the new variables, the $\mathbb{Z}_2 \times \mathbb{Z}_2$ symmetry of the Hamiltonian is spontaneously broken. The finite two-point correlations yield finite string order when mapped back to the original variables.

An interesting lattice boson analog of the Haldane phase, termed the Haldane insulator, has been identified in 1D Bose-Hubbard models with power-law repulsive interactions [41, 40]. The analogy can be made precise by truncating the local boson Hilbert space to three states about the average boson filling ($\overline{n}$) when fluctuations are small. Here, too, there is a string OP

$$\mathcal{O}_{HI}(i,j) \equiv \left\langle \delta n_i \exp\left[i\pi \sum_{i \le k < j} \delta n_k\right] \delta n_j \right\rangle. \tag{2.14}$$

($\delta n_i \equiv n_i - \overline{n}$.) $\mathcal{O}_{HI}(i,j)$ remains finite as $|i-j| \to \infty$ in the Haldane insulator. Interestingly, the Mott insulator can also be identified with a string OP

$$\mathcal{O}_{MI}(i,j) \equiv \left\langle \exp\left[i\pi \sum_{i \le k < j} \delta n_k\right] \right\rangle \tag{2.15}$$

which remains finite.

These string OPs are designed to detect the hidden order illustrated in Figure 2.3. The Haldane insulator is realized at an intermediate range of hopping and long-range repulsion.

Hopping favors delocalized particles and holes while repulsion favors alternation. The combined effect is that the Haldane insulator exhibits an alternating (antiferromagnetic) pattern of particles and holes if the sites with average filling are removed, of which there can be arbitrarily many in between. As in the spin-1 realization of the Haldane phase, this is precisely what Eq. 2.14 is designed to capture. In contrast, the Mott insulator is realized with strong onsite interactions; this favors a uniform filling with fluctuations of particle and holes that appear bound because of their common origin. Eq. 2.15 is designed to detect a uniform background but is stable to the creation of confined particle-hole pairs because the signed contributions of the two particles in a pair typically cancel.

The work on lattice bosons [41, 40] illustrates an important point, on which we will elaborate: string order need not be finite only for topologically nontrivial phases. Indeed, Eq. 2.15 also has a spin-1 version which will be finite in the trivial phase and vanish in the Haldane phase.[2]

Selection Rules

Let us review a number of observations about the form of a string OP in a symmetric phase, i.e. a phase which does not break a symmetry, following the discussion in [38, 35, 36]. A global application of any onsite symmetry would preserve the state, so it is plausible that application of the symmetry on a finite string leaves the bulk of the string invariant. This motivates the general from of a string OP, involving application of a symmetry along a string,

$$S = \lim_{|i-j|\to\infty} \left\langle O^A(i) \Big(\prod_{k=i+1}^{j-1} \Sigma(g) \Big) O^B(j) \right\rangle, \tag{2.16}$$

which will, for randomly chosen O^A, O^B, be finite in a symmetric phase. One is free to apply local operators at the string edges, which may alter the value but typically keep it finite. We can make precise the previous intuitions using the matrix-product state (Γ, Λ) form of a wavefunction. A graphical evaluation is illustrated in Figure 2.4 [36]. Using Eq. 2.10, the expectation reduces to an evaluation of the ladder in Figure 2.4(b). The long segments to the left, right, and middle of the local operators O^A, O^B amount to computing Schmidt state overlaps, which vanish unless the states are equal. All in all, the expectation asymptotically results in the product of two local evaluations,

$$S \approx \Big(\text{ tr } \Lambda \overline{O}^A \Lambda U_{g_1}^\dagger \Big) \Big(\text{ tr } \Lambda \overline{O}^B \Lambda U_{g_1}^T \Big), \tag{2.17}$$

as shown in Figure 2.4(c). ($\overline{O}^A_{\alpha'\alpha} \equiv \langle \alpha' L | O^A | \alpha L \rangle$ and $\overline{O}^B_{\alpha'\alpha} \equiv \langle \alpha' R | O^B | \alpha R \rangle$ are matrix elements with respect to left and right Schmidt states $|\alpha L\rangle$, $|\alpha R\rangle$ [36].)

[2] We also highlight, but will not discuss, work assessing the instability of string order to interchain couplings [42, 43, 40].

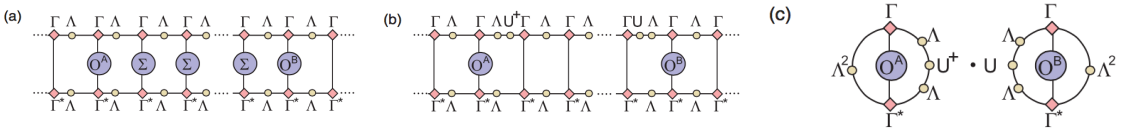

Figure 2.4: Evaluation of a string OP in a matrix-product state. Reproduced from [36].

Eq. 2.17 supports the observation that a string OP typically does not vanish in a symmetric phase. However, additional symmetry constraints could force one or both of the edge evaluations to vanish. Suppose the system has two onsite symmetries g_1, g_2, with matrix representations $\Sigma(g_1), \Sigma(g_2)$. Let a symmetric phase be identified with the angle $\phi \in \mathbb{R}$ in the projective representation of bond unitaries, i.e. $U_{g_2}U_{g_1} = e^{i\phi}U_{g_1}U_{g_2}$. Suppose that g_1 is the symmetry applied in the string of the OP. Further, let O^A not be arbitrary but chosen to satisfy the rule $\Sigma(g_2)O^A\Sigma(g_2)^\dagger = e^{i\sigma}O^A$, under the remaining symmetry g_2, for some angle σ. On the bonds, this enforces $U_{g_2}\overline{O}^A U_{g_2}^\dagger = e^{i\sigma}\overline{O}^A$. The following manipulation [36] reveals

$$\text{tr } \Lambda\overline{O}^A\Lambda U_{g_1}^\dagger = \text{ tr } U_{g_2}\Lambda\overline{O}^A\Lambda U_{g_1}^\dagger U_{g_2}^\dagger = e^{i(\sigma-\phi)} \text{ tr } \Lambda\overline{O}^A\Lambda U_{g_1}^\dagger. \tag{2.18}$$

Consequently, if $\sigma \neq \phi$, the string OP will vanish due to the local evaluation involving O^A. This suggests that to detect an SPT phase, if one chooses $\sigma = \phi$, the string OP is guaranteed to vanish in all others phases with $\phi' \neq \phi$.[3] As in [36], we will refer to this as a *selection rule*.

Indeed, the selection rule is able to explain the choice of operators for the string OP of the Haldane phase. For instance, when $e^{i\pi S^x}$ is used in the string, we terminate with S^x, which is even under $e^{i\pi S^x}$ but odd under the remaining symmetry $e^{i\pi S^z}$, to detect the Haldane phase associated with angle $\phi = \pi$. Likewise, terminating operators which are even under the symmetries (for instance, in Eq. 2.15) give a string OP which is finite in the trivial insulator and vanishes elsewhere.

Selection rules are by no means a full-proof route to constructing NLOPs; they may vanish at special points or yield a small value, and they do not generalize to more complex symmetry groups [36]. Nonetheless, in describing our work [1] beginning in Section 2.3, we will construct NLOPs for spinless interactiong fermion chains by utilizing the idea of selection rules.

2.3 String and Brane Order for Majorana Chains

In the remainder of the chapter, we discuss our construction of NLOPs for two symmetry classes of interacting topological superconductors of spinless fermions. The nontrivial phases

[3]Relying on the same manipulations, note that O^A should be chosen to be exactly invariant under the symmetry g_1 used in the string.

in these classes have Majorana zero-energy modes localized on their edges. Our NLOPs lie along a string for a single chain or cover an area ("brane" [38]) for multiple coupled 1D chains. We will refer to string or brane OPs collectively as NLOPs. The constructions are general in the sense that they hold for an entire phase, not just a particular Hamiltonian. Throughout the chapter, we will see the privileged role played by the fermion parity operator, $\prod_i e^{i\pi n_i}$, where n_i is the fermion occupation of site i.

We first consider single chains of spinless fermionic topological superconductors with interactions. Similar to the Haldane string OP, Eq. 2.13, the SPT phase here can be understood as originating from a spontaneously broken symmetry in a nonlocal set of variables; the string OP can be constructed accordingly from a two-point correlation function.

In Section 2.4, we consider coupled chains where we enforce an additional $\mathbb{Z}_N$ symmetry. The symmetric phases capture vestiges of some interesting 2D phases in a quasi-1D setting. The additional $\mathbb{Z}_N$ symmetry is to be viewed as a translation symmetry arising from stacking N identical 1D chains along a direction transverse to their infinite length. In this way, we can realize *weak* or *strong* versions of 2D SPTs. We use a free fermion model as a special case to understand the kinds of phases that arise from this classification and place them in correspondence with certain free fermion topological indices. NLOPs will be constructed by choosing terminating local operators with the appropriate symmetry transformation to identify a particular phase. We conclude that section by describing how one of the fermionic SPT phases and its OP can be understood in terms of a binding of Ising domain walls, defects of an Ising order.

We discuss the relevance of our NLOPs for ultracold atom experiments in Section 2.5. The quantum gas microscope [44, 45] is a recently developed tool which allows for imaging of an optical lattice with single-site resolution and hence simultaneous measurement of lattice site occupations [39]. This probe is particularly well-suited for identifying topological phases. Measuring topological aspects of free fermion band structures in ultracold atoms has been discussed [46–50]; here, however, we will be concerned with generic interacting systems, in particular topological superconductors. As an example of a measurement within present experimental reach, in Section 2.5 we describe a system of two identical chains for which a topological phase can be detected via measurements of site occupations alone.

The results that follow can be supported by working in either bosonic or fermionic variables. In the primary sections, we mainly take the bosonic point of view and discuss the fermionic description in Section 2.8. Section 2.9 outlines a derivation of selection rules for fermionic nonlocal OPs. Understanding the selection rules in fermionic variables directly may be helpful for classifying phases and constructing OPs for higher-dimensional fermionic systems, beyond the regime of correspondence.

Example: Kitaev's Majorana Chain

Our first symmetry class is particularly simple: topological superconductors of interacting spinless fermions with no additional symmetries. A notable property of all physical fermionic Hamiltonians is that they must be invariant under the $\mathbb{Z}_2$ fermion parity operator, $\prod_i e^{i\pi n_i}$.

This is due to a superselection rule – a fundamental constraint – and is typically not considered a symmetry. To illustrate the general form of the string OPs for this class, let us consider Kitaev's p-wave topological superconductor with Hamiltonian [51]

$$\begin{aligned} H_{Kit} &= \sum_i \left[\Big(-t a_i^\dagger a_{i+1} + |\Delta| a_i a_{i+1} + h.c. \Big) - \mu \Big(a_i^\dagger a_i - \frac{1}{2} \Big) \right] \\ &= \frac{i}{2} \sum_i \left[\Big(-t + |\Delta| \Big) \chi_i \overline{\chi}_{i+1} + \Big(t + |\Delta| \Big) \overline{\chi}_i \chi_{i+1} - \mu \chi_i \overline{\chi}_i \right]. \end{aligned} \tag{2.19}$$

The Majorana operators $\chi_i, \overline{\chi}_i$ are Hermitian operators which anticommute with each other and square to one. The complex lattice fermions are constructed as $a_i = \frac{1}{2}(\chi_i + i\overline{\chi}_i)$. The phase of the superconducting order parameter $\Delta = |\Delta| e^{i\theta}$ has been gauged away. For $|\frac{\mu}{2t}| < 1$, there are gapped topological phases if $|\Delta| \neq 0$ and a gapless normal phase if $|\Delta| = 0$. If $|\frac{\mu}{2t}| > 1$ for any $|\Delta|$, the phase is gapped and trivial.

To have an alternative view of the model, we can use the nonlocal Jordan-Wigner transformation,

$$\sigma_i^x = e^{i\pi n_i}, \qquad \sigma_i^y = \prod_{j<i} e^{i\pi n_j} \overline{\chi}_i, \qquad \sigma_i^z = -\prod_{j<i} e^{i\pi n_j} \chi_i, \tag{2.20}$$

to map the Majorana chain onto an XY-type spin model in a transverse magnetic field. The fermion parity operator transforms to a $\mathbb{Z}_2$ spin symmetry $\prod_i \sigma_i^x$. In the spin model, this symmetry is spontaneously broken or unbroken when the corresponding fermionic model has symmetry-protected topological or trivial order, respectively.

Consider an Ising limit of the corresponding spin Hamiltonian (by setting $t = |\Delta|$), $H_{spin} = -J \sum_i (\sigma_i^z \sigma_{i+1}^z + g \sigma_i^x)$, with $J = |\Delta|$ and $g = -\frac{\mu}{2|\Delta|}$. A two-point spin correlation function is nonzero when the spins are ordered and vanishes elsewhere. It maps back to a string OP in the fermions,

$$\langle \sigma_i^z \sigma_k^z \rangle = \left\langle (-i\overline{\chi}_i) \prod_{j=i+1}^{k-1} e^{i\pi n_j} \chi_k \right\rangle, \tag{2.21}$$

which distinguishes the SPT from the trivial phase in this limit.[4]

A string OP which is finite in the trivial fermionic phase can also be constructed by relying on the self-duality of the quantum tranverse Ising model. The dual mapping,

[4]Note that two-point correlations are insensitive to the linear combination of ground states states used. Fermionic ground states must always have definite fermion parity, and so the physical fermionic ground state in the SPT phase is a cat state consisting of symmetric or antisymmetric combinations of the two $\mathbb{Z}_2$ symmetry-breaking spin ground states.

$$\tau^x_{i+\frac{1}{2}} = \sigma^z_i \sigma^z_{i+1}, \qquad \tau^z_{i+\frac{1}{2}} = \prod_{j>i} \sigma^x_j, \tag{2.22}$$

transforms from spin to domain wall variables which live on the bonds. The Hamiltonian becomes

$$H_{dual} = \sum_i \left(-|\Delta| \tau^x_{i+\frac{1}{2}} + \frac{1}{2}\mu \tau^z_{i-\frac{1}{2}} \tau^z_{i+\frac{1}{2}} \right) \tag{2.23}$$

in the thermodynamic limit ($t = |\Delta|$). A two-point correlation function in the τ variables distinguishes the two phases. We therefore obtain the string OP for the trivial phase,

$$\left\langle \tau^z_{i+\frac{1}{2}} \tau^z_{k+\frac{1}{2}} \right\rangle \sim \left\langle \prod_j \sigma^x_j \right\rangle = \left\langle \prod_j e^{i\pi n_j} \right\rangle. \tag{2.24}$$

These simple limits are indicative of the general form we will discuss next. However, before doing so, we note that the Kitaev model, Eq. 2.19, is quite special since it has extra symmetries, such as time-reversal defined as $\chi \to \chi, \overline{\chi} \to -\overline{\chi}$. This constrains, for instance, the possible two-point correlation functions which can be chosen in the spin language: either σ^z or σ^y orders in the broken symmetry regimes for $t > 0$ or $t < 0$, respectively. This in turn restricts the fermionic operators which terminate the string: either $(\overline{\chi}_i, \chi_k)$ for $t > 0$, as in Eq. 2.21, or $(\chi_i, \overline{\chi}_k)$ for $t < 0$.

Such constrained choices will not occur for models with strictly no other symmetries, which is the class of fermions we are considering. While this appears to be a disadvantage, we see it as not much different than the obstacles to choosing an order parameter to detect a spontaneously broken symmetry: certain operators may be better to use because they typically yield larger magnitudes, while specific models may have larger symmetry groups which can be identified from the outset.

General Form

We used the Kitaev model, and in particular, an Ising limit of it when mapped to a spin model, to illustrate a more general correspondence which holds for all Hamiltonians in this class. These fermionic phases were classified in [20] precisely by mapping to spins (bosons) and identifying the phases in those variables. With a $\mathbb{Z}_2$ spin symmetry (originating in the mapping of fermion parity), only two phases are possible for bosons: symmetry-broken or trivial order. (Bosonic symmetry-protected topological order does not occur for symmetry group $G = \mathbb{Z}_2$.) Mapped back to fermions, however, since the fermion parity operator can never be broken, the distinction between the two phases must be one of symmetry-protected topological order.[5]

[5]Our models have translation symmetry along their infinite dimension, which can multiply the number of possible phases by a factor [20] but we neglect this multiplicity.

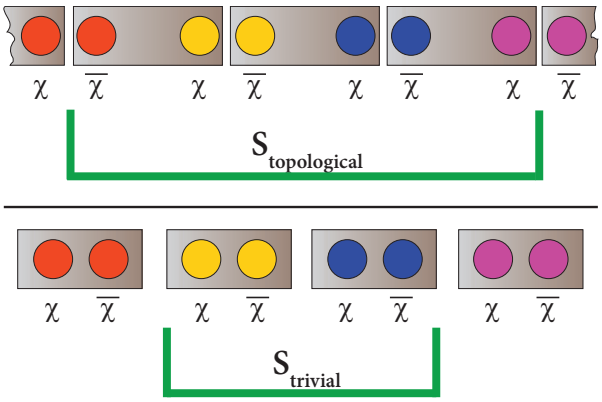

Figure 2.5: Single chain at top shows two Majorana fermions $\chi, \overline{\chi}$ per site (circles with same color) with nontrivial pairing (boxes). The nonlocal order parameter S_{top} for the topological phase measures this pairing by measuring all the operators within the bounds of the green line. It measures a "fractional" part of the physical sites (red, purple) on the edges of the region over which it acts. Bottom chain shows a phase with trivial Majorana pairings, which is measured by S_{triv}.

This correspondence entails string (or brane) OPs with the form

$$S_{top} = \left\langle O_L^f \left(\prod_{j\in\Omega} e^{i\pi n_j} \right) O_R^f \right\rangle,$$
$$S_{triv} = \left\langle O_L^b \left(\prod_{j\in\Omega} e^{i\pi n_j} \right) O_R^b \right\rangle, \tag{2.25}$$

where $O^f_{L/R}, O^b_{L/R}$ are local fermionic or bosonic terminating operators situated near the left, right edges of string or brane Ω. S_{top} is nonzero in the topological phase and vanishes elsewhere; the behavior of S_{triv} is reversed. From the correspondence with bosons, the choice of fermionic terminating operator in S_{top} can be seen to originate from the need to choose operators O, O' which are odd under the $\mathbb{Z}_2$ symmetry in the two-point correlation function $\langle O_i O'_j \rangle$. S_{triv}, on the other hand, is finite in the trivial phase since it amounts to application of the symmetry and is terminated by bosonic operators, as required by the bosonic selection rules [36]. In Section 5.4, we elaborate on why this NLOP vanishes in the broken-symmetry phase of spins.

The appearance of fermionic or bosonic terminations for a NLOP is the fermionic analog of the selection rules in [36]. As an alternative to using the Jordan-Wigner mapping, in Section 2.9 we justify fermionic selection rules for NLOPs directly using ideas from fermion classification [13].

Fermionic Picture

Let us take a different look at the selection rule requiring a fermionic or bosonic terminating operator for a NLOP. Consider the Ising limit of the single Kitaev chain and introduce bond fermions $\tilde{a}_i = \frac{1}{2}(\chi_{i+1} + i\overline{\chi}_i)$ by pairing Majoranas on neighboring sites, neglecting the nonlocal fermion $\tilde{a}_{NL} = \frac{1}{2}(\chi_1 + i\overline{\chi}_N)$ by working on an infinite chain. These variables solve the $t = |\Delta|, \mu = 0$ limit exactly. The topological and trivial phase string OPs, Eqs. 2.21, 2.24, can be rewritten ($k \geq i+1$)

$$S_{top} = \left\langle (-i\overline{\chi}_i) \prod_{j=i+1}^{k-1} e^{i\pi n_j} \chi_k \right\rangle \propto \left\langle \prod_{j=i}^{k-1} e^{i\pi \tilde{n}_j} \right\rangle, \tag{2.26}$$

$$S_{triv} = \left\langle \prod_{j=i}^{k} e^{i\pi n_j} \right\rangle \propto \left\langle (\tilde{a}_{i-1} + \tilde{a}_{i-1}^\dagger) \prod_{j=i}^{k-1} e^{i\pi \tilde{n}_j} (\tilde{a}_k - \tilde{a}_k^\dagger) \right\rangle. \tag{2.27}$$

Evidently, the fermionic or bosonic nature of the terminations depends on the basis used. The topological ground states at $t = |\Delta|, \mu = 0$ have uniform bulk filling in the *bond* fermion basis $\tilde{a}_i$ so that S_{top}, which measures their parity, is nonzero. A weak perturbation $\mu \neq 0$ drives the system away from this bond-centered ordering by favoring onsite Majorana pairings. In perturbation theory, this creates localized pairs of bond fermion defects with respect to the unperturbed state. However, the defects are bound and so do not altogether destroy the measurement of bond fermion parity S_{top}. The value of S_{top} is finite away from this limit and all throughout the SPT phase. A similar, dual picture holds for site fermions a_i deep in the trivial phase, for which site fermions are a good basis to use and defects again are confined pairs.

On the other hand, such string OPs vanish in the complementary phases. To see this, consider perturbatively evaluating S_{top} in the trivial phase of the $t = |\Delta|$ Kitaev model, for instance. The ground state at the point $H_0 = \frac{\mu}{2}\sum_i e^{i\pi n_i}$ with $\mu < 0$ is the site fermion vacuum $|0\rangle$ which is then corrected by the perturbation $V = |\Delta| \sum_i i\overline{\chi}_i \chi_{i+1} = |\Delta| \sum_i (a_i - a_i^\dagger)(a_{i+1} + a_{i+1}^\dagger)$. V corrects $|0\rangle$ by creating bound pairs of fermion defects on top of $|0\rangle$ and preserves fermion parity not just globally but locally, in a certain sense. On the other hand, S_{top} connects states which differ in *site* occupation at two points i, k with distant separation. Such states cannot arise through the effects of a local *and* fermion parity preserving perturbation applied to an initial state with uniform occupation throughout. Hence, S_{top} should remain zero as $|i-k| \to \infty$ even when the Hamiltonian is modified, and this holds for the entire phase.

2.4 Quasi-1D Phases with $\mathbb{Z}_N$ Translation Symmetry

N Coupled Chains on a Cylinder Geometry

We turn to a more complex symmetry class. The symmetry group of interest is $G = \mathbb{Z}_2 \times \mathbb{Z}_N$, where $\mathbb{Z}_2$ originates from fermion parity. For instance, this describes interacting topological superconductors of spinless fermions, where N identical 1D chains have been coupled with periodic boundary conditions in the transverse direction. In other words, the system has the geometry of an infinitely long cylinder with finite circumference N. Before devising NLOPs, let us identify all the symmetric fermionic phases that are possible in this class.

Classification

We map our system to bosons and identify the appropriate classes there. In the Jordan-Wigner transformation, we take a winding path which transforms the cylinder into a 1D infinite bosonic chain. Each bosonic unit cell now accounts for one ring of the fermionic cylinder and contains N spin-1/2 degrees-of-freedom. The $\mathbb{Z}_N$ fermion translation symmetry for the circumference, $a_{i,j} \to a_{i,(j+1) \bmod N}$, maps to a $\mathbb{Z}_N$ symmetry internal to the unit cell, which we note is not translation of the spins. The $\mathbb{Z}_2$ fermion parity symmetry (taking $a_{i,j} \to -a_{i,j}$) maps to a local $\mathbb{Z}_2$ spin symmetry. Consequently, the bosonic system has an onsite $\mathbb{Z}_2 \times \mathbb{Z}_N$ symmetry. Ultimately, we are interested in identifying all symmetric fermionic phases; these can originate from fully or only partially symmetric bosonic phases. Hence, we will specify the unbroken subgroup G' of the full group $G = \mathbb{Z}_2 \times \mathbb{Z}_N$ as well as any symmetry-protected topological orders of G'.

The possible fully symmetric bosonic phases are determined by $H^2(\mathbb{Z}_2 \times \mathbb{Z}_N, U(1))$. The answer depends on the parity of N. Let us see why this is the case. There are two bosonic generators corresponding to the fermionic symmetry generators, parity P and translation T. The projective representation of the two bosonic generators, labeled U_P, U_T, each has an overall phase that can be fixed so that $U_P^2 = U_T^N = 1$. However, the angle $\phi \in [0, 2\pi)$ in $U_P U_T = e^{i\phi} U_T U_P$ cannot be eliminated by redefinition of the matrices U. Moreover, it must satisfy $e^{2i\phi} = e^{Ni\phi} = 1$ because of our gauge fixing. Hence, there are two possible solutions, $\phi = 0$ and $\phi = \pi$, but the latter is forbidden for N odd. The gauge-invariant scalar $e^{i\phi}$ is quantized and consequently preserved under smooth, gap-respecting deformations to the wavefunctions. The two possible values of $e^{i\phi}$ represent two gauge-inequivalent classes of projective representations of the symmetry group $\mathbb{Z}_2 \times \mathbb{Z}_N$. Other complex phases which cannot be gauged away are related to this one, so specifying ϕ is sufficient to label a projective representation. Therefore, we obtain $H^2(\mathbb{Z}_2 \times \mathbb{Z}_N, U(1)) = \mathbb{Z}_2, \mathbb{Z}_1$ for N even, odd, respectively. Since a product state can be represented by scalar Γ_j and hence scalar U_P, U_T, $\phi = 0$ must describe the trivial phase. In contrast, $\phi = \pi$ characterizes a topologically nontrivial phase.

Besides the symmetric bosonic phases identified above, there are some broken-symmetry bosonic phases that correspond to completely symmetric fermionic phases when mapped

Bosonic Label	Fermionic Label (μ, μ')	G.S.D.	Example
1. Trivial symmetric $G' = G$	$(0, 0)$	1	Trivial
2. Nontrivial symmetric $G' = G$	$(0, \pi)$	4	Weak Top. Supercond.
3. Symmetry breaking $G' = \langle T \rangle$	$(\pi, 0)$	2	Strong Top. Supercond.
4. Symmetry breaking $G' = \langle PT \rangle$	(π, π)	2	Strong Top. Supercond.

Table 2.1: Quasi-1D symmetric fermionic phases for even N with symmetry group $G = \mathbb{Z}_2 \times \mathbb{Z}_N$. Ground state degeneracy (G.S.D.) listed is for open boundary conditions and the generic case, where there are no additional symmetries. For odd N, only Classes 1 and 3 exist.

back. This symmetry restoration is possible because of the distinguished role of fermion parity P: since it can not be broken in the fermionic variables, if only a small subset of the symmetry group G is broken in the bosonic variables, those symmetries can also be restored. We label these phases by their unbroken symmetry subgroup $G' \subsetneq G$. The relevant ones are the cyclic subgroups generated by bosonic versions of (i) translation T and, for even N only, (ii) the product of fermion parity and translation, labeled PT. We denote these by $G' = \langle T \rangle$ and $G' = \langle PT \rangle$ respectively.

We also describe the labeling of the phases in the fermionic language of [13]. The effective form $(\hat{P}, \hat{T})$ of fermionic symmetry operators P, T will consist of two fractional pieces: $\hat{P} \sim P_L P_R$ and $\hat{T} \sim T_L T_R$. The phases will be described by the commutation relations of these pieces, identified by the combination of angles (μ, μ') where $P_L P_R = e^{i\mu} P_R P_L$ and $T_L T_R = e^{i\mu'} T_R T_L$.

The correspondence between the bosonic and fermionic labeling of all the phases of interest is given in Table 2.1. Going forward, we will refer to the four possible phases (for N even) or two (for N odd) by their class number $1 - 4$ given in the table. Rather generally, fractionalization of fermionic symmetry P into fermionic pieces ($\mu = \pi$) means it is broken in bosonic variables [12]. This is not true for other fermionic symmetries, such as the $\mathbb{Z}_N$ translation, whose behavior in bosonic variables depends in part on those of parity (see Section 2.9).

Representative Free Fermion Models

To begin developing a picture of the phases in Table 2.1, we write down example Hamiltonians for the three nontrivial classes, momentarily putting aside practical realizations. We work with free fermions for mathematical convenience but emphasize that the distinction between

the phases persists with interactions.

First, an introduction of some notation: we continue to treat the infinite dimension of the chains in real space, with lattice sites i along x, but switch to momentum k_y in the transverse direction y with N sites and periodic boundary conditions. The occupation of the mode with destruction operator $a_{k_y}(i) = N^{-1/2}\sum_{j=1}^{N} e^{ik_y j}a_{i,j}$ is $n_{k_y}(i)$, and the Majorana operators $\chi_{k_y}(i), \overline{\chi}_{k_y}(i)$ are defined by the decomposition $a_{k_y}(i) = \frac{1}{2}\left[\chi_{k_y}(i) + i\overline{\chi}_{k_y}(i)\right]$. Let us examine the fermionic symmetry operators, P and T,

$$P = \prod_{i,k_y} e^{i\pi n_{k_y}(i)}, \qquad\qquad T = \prod_{i,k_y} e^{ik_y n_{k_y}(i)}. \tag{2.28}$$

Note that the $k_y = 0$ modes do not contribute to the translation operator; we will take advantage of this. We would like to identify representative Hamiltonians which lead to specific fractionalization patterns (μ, μ') given in Table 2.1.

The operators $\{a_{k_y}(i)\}_i$ for fixed k_y can be viewed as candidate degrees of freedom for a single realization of a Kitaev model, Eq. 2.19. We can tune each such chain to have SPT or trivial order. Consider Class 3 in Table 2.1 as an example. If we fix the ground state to have uniform site occupations, for instance by tuning all $k_y \neq 0$ chains to be in the trivial phase, then T will act as a scalar in the ground state subspace, i.e. the effective form will be $\hat{T} = 1$ and $\mu' = 0$. Moreover, tuning the $k_y = 0$ chain to be topologically nontrivial will force P to fractionalize in the ground state subspace: that is, $\hat{P} = i\chi_0(1)\overline{\chi}_0(L)$ and hence $\mu = \pi$. This is accomplished with the following Hamiltonian

$$H_3 = \sum_i i\overline{\chi}_0(i)\chi_0(i+1) + \sum_{i,k_y\neq 0} i\chi_{k_y}(i)\overline{\chi}_{k_y}(i). \tag{2.29}$$

By tuning the $k_y = 0$ degrees of freedom into the topological phase, a two-fold degeneracy arises from the occupation or vacancy of the nonlocal complex fermion mode. In the ground state subspace, the only distinction between the two ground states is the parity of this single nonlocal fermion. The ground state subspace in Class 3 will be (minimally) two-fold degenerate on the cylinder, consistent with the bosonic description since $|G/G'| = 2$ with $G' = \langle T\rangle$.

Likewise, we can write down a model for Class 4 (which requires N to be even to exist). By switching the treatments of the $k_y = 0$ and $k_y = \pi$ chains, we can force both the P and T symmetries to fractionalize. In this case, it originates from the $k_y = \pi$ chain having symmetry-protected topological order.

$$H_4 = \sum_i i\overline{\chi}_\pi(i)\chi_\pi(i+1) + \sum_{i,k_y\neq\pi} i\chi_{k_y}(i)\overline{\chi}_{k_y}(i) \tag{2.30}$$

is an example Hamiltonian.

Finally, tuning both the $k_y = 0$ and $k_y = \pi$ chains to the topological phase, while other momentum modes are set to be trivial, yields a Hamiltonian for Class 2 (again requiring N to be even),

$$H_2 = \sum_i \left(i\overline{\chi}_\pi(i)\chi_\pi(i+1) + i\overline{\chi}_0(i)\chi_0(i+1) \right) + \sum_{i,k_y \neq 0,\pi} i\chi_{k_y}(i)\overline{\chi}_{k_y}(i). \tag{2.31}$$

Since P measures contributions from both the $k_y = 0$ and $k_y = \pi$ chains, with H_2 there are effectively two unpaired Majorana fermions per edge and $\hat{P}$ will fractionalize into bosonic pieces. In contrast, since T depends on $k_y = \pi$ modes but not on $k_y = 0$, it will fractionalize into fermionic pieces. Together, this gives the angles $(\mu, \mu') = (0, \pi)$.

Physical Free Fermion Models

The representative Hamiltonians become increasingly nonlocal for large N and hence unphysical. Instead, we turn to connecting the phases to the ground states of a free fermion Hamiltonian with local interactions. A nearest-neighbor interchain hopping $t_\perp$ and, for $N > 2$, a nearest-neighbor interchain pairing $\Delta_\perp$ are allowed by translational invariance. We examine the simple lattice $p + ip$ topological superconductor studied in [52]. Assume that $N > 2$ and N is even. The Hamiltonian is

$$H = \sum_i \sum_{j=1}^{N} \Big(-ta^\dagger_{i,j}a_{i+1,j} + |\Delta| a_{i,j}a_{i+1,j} + h.c. \Big) - \mu \Big(n_{i,j} - \frac{1}{2} \Big) + \Big(\Delta_\perp a_{i,j}a_{i,j+1} - t_\perp a^\dagger_{i,j}a_{i,j+1} + h.c. \Big), \tag{2.32}$$

with i, j indexing sites along the cylinder length and circumference, respectively. We take fixed parameters $|\mathrm{Im}(\Delta_\perp)| > 0, \mathrm{Re}(\Delta_\perp) = 0$ and $|\Delta| > 0$. In this case, there are transitions between phases including quasi-1D versions of the 2D weak and strong TSCs as $t_\perp/\mu$ and t/μ are varied [52]. The experimentally relevant two chain ($N = 2$) version of this model will be considered in Section 2.5.

The phases can be identified by switching to momentum labels in the transverse direction,

$$H = H_{Kit,0}(\mu_+) + H_{Kit,\pi}(\mu_-) + H'_{Kit}, \tag{2.33}$$

where $H_{Kit,0}$ and $H_{Kit,\pi}$ are the Kitaev model, Eq. 2.19, built out of Majorana operators $(\chi_0, \overline{\chi}_0)$ and $(\chi_\pi, \overline{\chi}_\pi)$, respectively, and $\mu_\pm \equiv \mu \pm 2t_\perp$. The remaining piece H'_{Kit} contains all $k_y \neq 0, \pi$ degrees of freedom. Let us change variables further by recombining the four Majoranas for each $k_0 \equiv |k_y| \neq 0, \pi$ into $\eta_{k_0}/\overline{\delta}_{k_0}(i) \equiv \frac{1}{\sqrt{2}}(\chi_{k_0}(i) \pm \chi_{-k_0}(i))$ and $\overline{\eta}_{k_0}/\delta_{k_0}(i) \equiv \frac{1}{\sqrt{2}}(\overline{\chi}_{-k_0}(i) \pm \overline{\chi}_{k_0}(i))$ (upper signs for $\eta_{k_0}, \overline{\eta}_{k_0}$). With this transformation, the remainder H'_{Kit} can be viewed as a collection of Kitaev chains, a pair for each $k_0 \in (0, \pi)$ with its

own set of Majorana operators $(\eta, \overline{\eta})$ and $(\delta, \overline{\delta})$, and the chemical potential modified to $\mu_{k_0} = \mu + 2t_\perp \cos(k_0)$. There is an interchain coupling between the $(\eta, \overline{\eta})$ and $(\delta, \overline{\delta})$. It is proportional to $\mathrm{Im}(\Delta_\perp)$ and gaps out the Majorana zero modes of each chain. Altogether, we have

$$H'_{Kit} = \sum_{k_0 \in (0,\pi)} H_{Kit,(\eta_{k_0}, \overline{\eta}_{k_0})}(\mu_{k_0}) + H_{Kit,(\delta_{k_0}, \overline{\delta}_{k_0})}(\mu_{k_0}) - \sum_{i, k_0 \in (0,\pi)} i\mathrm{Im}(\Delta_\perp) \sin(k_0) \left(\eta_{k_0} \delta_{k_0} + \overline{\delta}_{k_0} \overline{\eta}_{k_0} \right)(i). \quad (2.34)$$

Since the $k_0 \in (0, \pi)$ chains cannot exhibit symmetry-protected topological order due to their coupling, the order of the ground states will be determined by the behavior of the $k_y = 0$ and $k_y = \pi$ chains alone. The $k_y = 0$ chain displays nontrivial order when the associated chemical potential is sufficiently weak, $|t_\perp + \frac{\mu}{2}| < |t|$. In this case, there is a 1D $\mathbb{Z}_2$ topological invariant $\nu_{k_y=0} = 1$ [52]. Likewise, the $k_y = \pi$ chain displays nontrivial order ($\nu_{k_y=\pi} = 1$) for $|t_\perp - \frac{\mu}{2}| < |t|$. Hence, for weak $|t_\perp/\mu|$ and $|t/\mu| > 1/2$, the system has two Majorana zero modes per edge, at $k_y = 0$ and π. As the cylinder circumference increases, $N \to \infty$, this phase will approach the 2D weak topological superconductor, as in this regime the 2D $\mathbb{Z}$ invariant (Chern number) is $\nu = 0$. For intermediate values $|t_\perp| \sim |t|$ and weak chemical potential, the system has a single Majorana zero mode per edge (either at $k_y = 0$ or π) and in contrast will scale to a 2D strong topological superconductor as $N \to \infty$, since the 2D $\mathbb{Z}$ invariant $|\nu| = 1$. When interchain hopping $t_\perp$ dominates over intrachain hopping $|t_\perp/\mu| > |t/\mu| + 1/2$, the system is a weak topological superconductor in the x, rather than y, direction. Figure 2.6 gives a phase diagram.

Since the three sets of degrees of freedom $k_y = 0$, $k_y = \pi$, and $k_y \neq 0, \pi$ decouple from each other, we can tune each into topological or trivial phases independently while maintaining translational invariance. For instance, if the $k_y = 0$ chain exhibits nontrivial order, treating this as a single chain with no other symmetries, we can find a path connecting to the model $\sum_i i\overline{\chi}_0(i)\chi_0(i+1)$ which preserves translation symmetry since it only involves $k_y = 0$ operators. Hence, the quasi-1D phases of Eq. 2.32 – namely the 2D weak topological superconductor associated with stacking along the y direction, and the two strong topological superconductors with $(\nu_{k_y=0}, \nu_{k_y=\pi}) = (1, 0)$ or $(0, 1)$ – would fall into Classes 2, 3, and 4, respectively, of our classification. It appears that for free fermions our classification identifies the 1D $\mathbb{Z}_2$ invariants $\nu_{k_y=0}$ and $\nu_{k_y=\pi}$ and consequently ν mod 2, since $\nu_{k_y=0} + \nu_{k_y=\pi} = \nu \bmod 2$ [52].

The weak topological superconductor with $\nu_{k_x} \neq 0$ for $k_x = 0$ or π, which is associated with stacking in the x direction, appears as a trivial phase. This phase results with strong $t_\perp$, but in the momentum k_y basis this coupling is an effective chemical potential, $\mu_\pm = \mu \pm 2t_\perp$, which favors onsite pairing of y-momentum Majoranas and drives the $k_y = 0$ and $k_y = \pi$ Majorana chains away from nontrivial pairing. It is natural that that our classification is unable to detect the topological index associated with translation symmetry along the x

direction (i.e. along the cylinder length), as translation symmetry along the y direction is the one we have been strictly imposing.

Nonlocal Order Parameters for the Symmetric Phases

We next construct nonlocal order parameters to distinguish the $\mathbb{Z}_2 \times \mathbb{Z}_N$ protected symmetric fermionic phases from each other. We restrict to even N since this encompasses the results for odd N. The NLOPs span a finite size L along the cylinder length, but, as with all order parameters (local or not), our interest lies in the finiteness of their asymptotic $L \to \infty$ values. We will rely on the identification of the phases in the bosonic variables. Where a symmetry is broken, we can use a two-point correlation function. To distinguish symmetric bosonic phases, we chose a symmetry to apply over many unit cells of the bosonic chain (a string), and we terminate the domain with operators obeying proper symmetry transformation rules. Note that the natural unit cell of the bosonic chain (which makes the $\mathbb{Z}_N$ symmetry onsite) corresponds to a cylindrical ring in the fermions. Mapped back to fermions, the NLOP consists of a cylindrical brane in the bulk over which a symmetry is applied, and terminating operators reside on the domain edges. We capture this general form by writing the NLOP as $\langle O_L \left(\prod_{j=1}^{L} \Sigma_j \right) O_R \rangle$. O_L/O_R are possibly different operators acting near the left, right bosonic string (fermionic brane) edges and Σ_j is a symmetry operation on a bosonic unit cell (fermionic cylindrical ring).

Alternatively, we corroborate our conclusions by working directly with fermions in Section 2.9. These rules determine how the terminating operators of the fermion order parameters should be chosen, when fermion parity P is used as the bulk symmetry, to distinguish the symmetric fermionic phases, in analogy with the bosonic derivation [36]. The rules are listed in Table 2.2. The even or odd transformation rule for a terminating operator under P and T symmetries distinguishes among the symmetric phases of any interacting model in this symmetry class.

Construction

Consider, as an example, a NLOP which applies the symmetry P over many bosonic unit cells spanning $[1, L]$ (a large fermionic brane). Define

$$S_1 \equiv \prod_{k_y} \prod_{i=1}^{L} e^{i\pi n_{k_y}(i)}. \tag{2.35}$$

The expectation $\langle S_1 \rangle$, taken with respect to any ground state, vanishes in Classes 3 and 4 because P is broken in the bosonic variables (Section 5.4). For Classes 1 and 2, P remains a symmetry for the bosons. The bosonic selection rules [36] inform us that the operators $O_{L,R}$ which terminate the bosonic string (fermionic brane) can be chosen to transform under symmetries in such a way as to select a quantum phase. The distinction between the two

Phase (Bosonic Variables)	P Trans.	T Trans.	Example
1. Trivial symmetric $G' = G$	Even	Even	$\langle S_1 \rangle \neq 0$
2. Nontrivial symmetric $G' = G$	Even	Odd	$\langle S_2 \rangle \neq 0$
3. Symmetry breaking $G' = \langle T \rangle$	Odd	Even	$\langle S_3 \rangle \neq 0$
4. Symmetry breaking $G' = \langle PT \rangle$	Odd	Odd	$\langle S_4 \rangle \neq 0$

Table 2.2: Transformation rules for O_L, O_R under parity P and translation T which would uniquely distinguish the four symmetric fermionic phases (N even) when fermion parity is used as the bulk symmetry operator. The examples are NLOPs which are asymptotically finite in the listed phase and vanish in the other symmetric fermionic phases.

phases Classes 1 and 2 in the bosonic description is the angle $\phi = 0, \pi$. $O_{L,R}$ must be even under parity because it is the symmetry used in the bulk of the order parameter but transform as $e^{i\phi}$ under translation in order to be finite in the quantum phase labeled by ϕ. The NLOP is guaranteed to vanish in the other symmetric bosonic phase. Mapped back to the fermionic system, the brane termination operators should be bosonic but should be even or odd under translation so that the OP is nonzero in Classes 1 or 2, respectively.

S_1 is, for instance, an order parameter which is nonzero in Class 1 but vanishes in Class 2 since translation invariant operators terminate its bulk. To construct a candidate with reversed behavior, we can choose operators such as $O(i) = i\chi_0(i)\chi_\pi(i)$ or $i\overline{\chi}_0(i)\overline{\chi}_\pi(i)$, which are even under parity but odd under translation, to terminate the fermionic brane. Hence, candidate order parameters which give a nonzero expectation value for Class 2 only include

$$S_2 \equiv \overline{\chi}_0(1)\overline{\chi}_\pi(1)\Big(\prod_{k_y,i=2}^{L-1} e^{i\pi n_{k_y}(i)}\Big)\chi_0(L)\chi_\pi(L) \tag{2.36}$$

and a similarly constructed S_2' with fermionic ends $\chi_0(1)\chi_\pi(1)$ and $\overline{\chi}_0(L)\overline{\chi}_\pi(L)$.

Finally, we can utilize the fact that certain symmetries are broken in the bosonic variables to construct NLOPs that are nonzero in a symmetry breaking bosonic phase but vanish elsewhere. We use two-point functions in the bosonic variables $\langle U_i V_j \rangle$ with $|i-j| \to \infty$. If U, V are odd under P but even under T, the result is nonzero in Class 3 but vanishes in the other symmetric fermionic phases. Likewise, operators odd under P but even under PT yield OPs which can detect Class 4. Mapped back to fermions, a few such candidates are:

$$S_3 \equiv -i\overline{\chi}_0(1)\prod_{k_y,i=2}^{L-1} e^{i\pi n_{k_y}(i)}\chi_0(L), \tag{2.37}$$

$$S_4 \equiv -i\overline{\chi}_\pi(1) \prod_{k_y,i=2}^{L-1} e^{i\pi n_{k_y}(i)} \chi_\pi(L), \tag{2.38}$$

or similar constructions defined as S_3', S_4', with fermionic ends, $-i\chi_0(1), \overline{\chi}_0(L)$ and $-i\chi_\pi(1), \overline{\chi}_\pi(L)$, respectively.

Application

We apply these order parameters to the $p+ip$ model with cylinder geometry. For instance, let us work in the $t = |\Delta|$ limit of the strong topological superconductor where only the $k_y = 0$ chain is in the topological phase. Evaluations decouple into $k_y = 0, \pi$, and $k_0 \in (0, \pi)$ contributions: $\langle S_3 \rangle = \langle S_{top} \rangle_{k_y=0} \langle S_{triv} \rangle_{k_y=\pi} \langle S_{triv} \rangle_{\prod k_0 \in (0,\pi)} \neq 0$. This NLOP would vanish in the other phases because the behavior of the $k_y = 0, \pi$ chains (viewed as topological or trivial) would be different. Regions where the order parameters take nonzero values are shown in Figure 2.6.

The fermion parity operator used in the bulk of the NLOPs given in the previous section can be reduced to parity for just the $k_y = 0, \pi$ DOF, since the degrees of freedom for remaining momenta always maintain trivial order in the $p+ip$ model. This reduction may not be applicable in general, as when interactions are added.

We emphasize that this model, as in the case of the single Kitaev Majorana chain, has additional symmetries beyond $\mathbb{Z}_2 \times \mathbb{Z}_N$ which puts constraints on the construction of the NLOP. For instance, a choice of $O_{L/R} \propto (\chi, \overline{\chi})$ is different from $(\overline{\chi}, \chi)$, as we saw in the single chain. However, for models which only have $\mathbb{Z}_2 \times \mathbb{Z}_N$ symmetry, only these symmetries need to be accounted for. Therefore, order parameters constructed using the general principles described work generically. For instance, S_3, S_3' and similar order parameters are all suitable choices to distinguish Class 3 from the other symmetric fermionic phases.

Dual Defect Condensate as a Model for an SPT Phase

To develop a complementary picture of one of the phases, we consider Class 2 in the bosonic variables for the case of two chains. In this case, the symmetry group is the same as that of the Haldane phase, $G = \mathbb{Z}_2 \times \mathbb{Z}_N$. Our construction will be a one-dimensional version of certain higher-dimensional constructions for SPT phases [53]. Two "dual" defects (where one defect appears as a nonlocal object in the variables in which its partner is local) will be bound together and then condensed. The composite object will carry a nontrivial quantum number under the symmetries.

Let σ, τ be two Ising variables with the $\mathbb{Z}_2$ symmetries $\prod_i \sigma_i^x, \prod_i \tau_i^x$. Condensation of domain walls of σ, created at site j by $\prod_{i<j} \sigma_i^x$, would lead to an Ising disordered phase $\langle \sigma_i^z \rangle = 0$. Conversely, condensation of spin flips created by σ^z realizes the ordered phase. Consider then condensing a bound state of a σ defect and its τ dual defect, for instance the composite object $\rho_j = \prod_{i<j} \sigma_i^x \tau_j^z$. If no symmetries are broken, this will yield a topological phase. To preserve the symmetries, for instance, one can also condense τ domain wall and

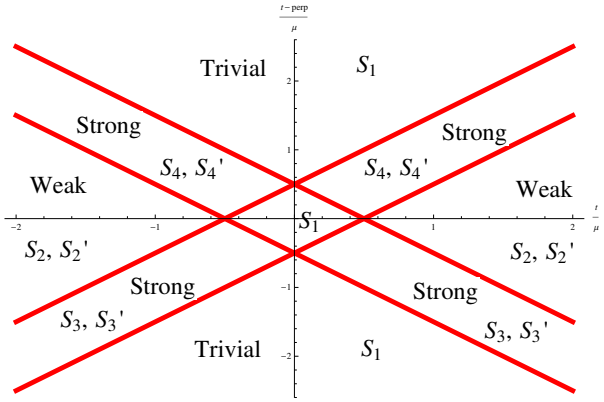

Figure 2.6: Phase diagram and nonlocal order parameter values for the quasi-1D $p + ip$ paired model (Eq. 2.32) with axes $(t/\mu, t_\perp/\mu)$. Phases are labeled as trivial, weak, or strong topological superconductor (center diamond is also trivial). The labels S, S' refer to the order parameters of the main text which take on nonzero values in the regions listed. (Unprimed, primed versions require either $t > 0$ or < 0, respectively.)

σ spin flip pairs, $\delta_j = \prod_{i \le j} \tau_i^x \sigma_j^z$. A string order parameter for this topological phase will be a product of two-point correlations functions,

$$\langle \rho_i \rho_j \delta_i \delta_j \rangle = \left\langle \tau_i^z \sigma_i^y \left(\prod_{i<k<j} \sigma_k^x \tau_k^x \right) \tau_j^y \sigma_j^z \right\rangle. \tag{2.39}$$

The order parameter is of the general form discussed previously. It consists of applying one symmetry over the bulk (here, $\prod_i \sigma_i^x \tau_i^x$) and terminating with operators $\tau^z \sigma^y$ or $\tau^y \sigma^z$ which are even under the symmetry used in the bulk and odd under the remaining symmetries, $\prod_i \sigma_i^x, \prod_i \tau_i^x$.

From these ingredients, we write a Hamiltonian which realizes this topological phase. Consider starting at the critical point of a pair of decoupled Ising models,

$$H_0 = -\sum_i \left(\sigma_i^x + \tau_i^x + \sigma_i^z \sigma_{i+1}^z + \tau_i^z \tau_{i+1}^z \right), \tag{2.40}$$

and adding correlations for the Z_2 charge and domain wall bound pairs in order to induce condensation of these composites,

$$H_1 = -\sum_i \left(\rho_i \rho_{i+1} + \delta_i \delta_{i+1} \right) \tag{2.41}$$

$$= -\sum_i \left(\sigma_i^z \sigma_{i+1}^z \tau_{i+1}^x + \tau_i^z \tau_{i+1}^z \sigma_i^x \right). \tag{2.42}$$

The Hamiltonian $H(\lambda) = H_0 + \lambda H_1$ realizes the nontrivial topological phase for $\lambda > 1$ with nonlocal order parameter $\rho_i \delta_i$. This is made apparent by making a dual transformation

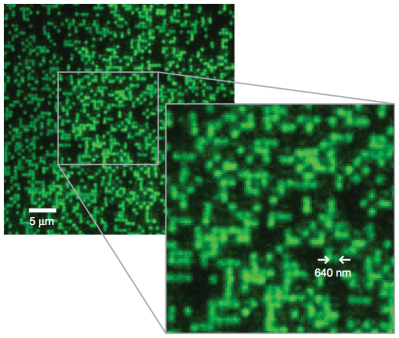

Figure 2.7: Single-site resolved imaging of atoms using the quantum gas microscope in a 640-nm-period optical lattice. Reproduced from [44].

on one of the $\mathbb{Z}_2$ variables and mapping onto the quantum Ashkin-Teller model [54, 55]. Moreover, H_1 itself is exactly solvable and its ground state is a so-called cluster state [56], which will play a key role in the discussions of Chapter 3. There is a four-fold degeneracy on a chain with sites 1 to L. On each edge, we can construct a spin-1/2 algebra with local operators; for instance, $\sigma_1^z\tau_1^x$, $\sigma_1^x\tau_2^z$, and $\sigma_1^y\tau_1^x\tau_2^z$ operate on the left edge while $\sigma_L^x\tau_L^z$, $\sigma_{L-1}^z\tau_L^x$, and $\sigma_{L-1}^z\sigma_L^x\tau_L^y$ operate on the right edge. Since we can map within the ground state manifold via edge and not bulk operators, the distinction between the degenerate states is one of symmetry-protected topological order and not spontaneously broken symmetry.

2.5 Measuring Nonlocal Order in Ultracold Atomic Systems

Ultracold atomic systems are an increasingly attractive platform for simulating and understanding condensed matter systems. Single-site-resolved imaging of optical lattices is now possible with the "quantum gas microscope" [44, 45]. Figure 2.7, for instance, shows simultaneous measurement of single site occupations across a many-atom system, a feat currently impossible in a materials setting. Subsequent experiments [39] established the practicality of identifying a quantum phase by relying on measurements of string order, with a first demonstration on the bosonic Mott insulator [40, 41]. The quantum gas microscope would therefore serve as an especially useful tool for identifying topological phases, which cannot be identified by local means in their bulk, in cold atom settings. We provide two example protocols of how nonlocal order could be measured with current experimental tools, which at present can only make measurements in the occupation number basis.

Example 1: Single Chain Protocol

Although a simple NLOP involving only measurements of fermion parity can be used to identify a trivial phase, and hence indirectly infer the existence of topological phase in a

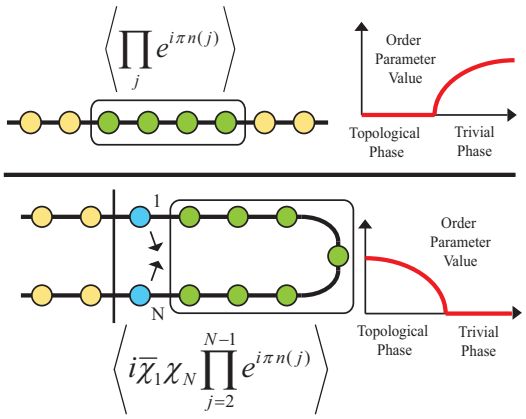

Figure 2.8: Top shows single Majorana chain (sites are circles) and the order parameter for the trivial phase which can be measured in current cold atom experiments since it only involves fermion parity (boxed green circles). Bottom shows a potential scheme for measuring order parameters with fermionic terminations such as Eq. 2.43. Fermion parity is still measured in the bulk (green), but additional measurements for the end sites labeled 1, N (blue circles) must be made to extract the string order parameter value.

known phase diagram, it is preferable to a get a positive signature for an SPT phase directly. Therefore, we consider how one might measure NLOPs with complex terminations. For instance,

$$S_{top} = \left\langle (-i\overline{\chi}_1) \prod_{j=2}^{N-1} e^{i\pi n_j} \chi_N \right\rangle \tag{2.43}$$

directly detects the topological phase by generically yielding a nonzero value. The difficulty with measuring NLOPs such as S_{top} is that they are off-diagonal in the lattice site fermion basis which is imaged in experiments. We suggest a scheme for measuring a string OP such as S_{top} on the interval $[1, N]$ in the bulk of a long Majorana chain. The idea is that by evolving the ground state in a controlled manner, such as with a tunneling Hamiltonian, we may extract the additional information needed to reconstruct the string OP (Figure 2.8).

For instance, let a ground state for the Kitaev model (Eq. 2.19) be

$$|\psi\rangle = \sum_{ijk} \beta_{ijk} |n_i^I\rangle |n_j^O\rangle |n_k\rangle. \tag{2.44}$$

Here, $|n_i^I\rangle$ is a site fermion configuration indexed by i for the inner region, sites 2 to $N-1$; $|n_j^O\rangle$ indexes states for the region outside $[1, N]$; and $|n_k\rangle$ is a configuration for the end sites 1 and N of the string, with $\{|n_k\rangle\}_{k=1}^4 = \{|0\rangle, a_1^\dagger|0\rangle, a_N^\dagger|0\rangle, a_N^\dagger a_1^\dagger|0\rangle\}$. With this form, the expectation value is

$$S_{top} = 2\sum_{ij} P_i \Big(-\mathrm{Re}(\beta_{ij1}\overline{\beta}_{ij4}) + \mathrm{Re}(\beta_{ij2}\overline{\beta}_{ij3}) \Big), \tag{2.45}$$

where P_i is the parity of configuration i for sites $[2, N-1]$. The additional information that is needed, beyond amplitudes $|\beta_{ijk}|$, to reconstruct the value are certain relative phases, such as those in $\beta_{ij1}\overline{\beta}_{ij4}$ and $\beta_{ij2}\overline{\beta}_{ij3}$.

We consider repeatedly initializing the system in a fixed Kitaev chain ground state $|\psi\rangle$. A tunneling Hamiltonian H_T, which for instance couples only sites 1 and N, is turned on rapidly, preserving the state. We may consider changing the experimental geometry to have the single chain folded in two in order to couple sites 1 and N. After dynamic evolution with H_T, the site fermion occupations are measured at specified times. This information, along with accurate knowledge of the Hamiltonian parameters and amplitudes $|\beta_{ijk}|$ determined from repeated measurements, would enable extraction of the necessary relative phases and reconstruction of the string OP value.

Nonetheless, a general challenge appears to be the number of measurements needed, as a ground state for N sites in the deepest regimes of the topological phase consists of an exponential in N number of states in the lattice site basis, all with equal magnitude weights. Design of a detailed protocol to enable extraction of the off-diagonal interference terms would be an interesting development.

Example 2: Two Identical Chains

As an alternative, we show that it is possible to detect a phase with symmetry-protected topological order by making measurements in the lattice site basis only, making it accessible for current ultracold atom experiments. Consider two identical chains A and B, each with parameters $(t, |\Delta|, \mu)$ in the Kitaev model, and further coupled with an interchain hopping $t_\perp$. This high-symmetry model is the $N = 2$ case of the systems considered in Section 2.4

As before, the phases of this system can be easily seen by switching to momentum $k_y = 0, \pi$ in the transverse direction. The resulting Hamiltonian consists of two decoupled Kitaev models for the $k_y = 0, \pi$ variables, $\{a_0(i)\}_i \cup \{a_\pi(i)\}_i$, with modified chemical potentials $\mu_\pm \equiv \mu \pm 2t_\perp$,

$$\begin{aligned} H &= H_{Kit,A} + H_{Kit,B} - 2t_\perp \sum_i (a_{iA}^\dagger a_{iB} + h.c.) \\ &= H_{Kit,0}(\mu_+) + H_{Kit,\pi}(\mu_-). \end{aligned} \tag{2.46}$$

For $|\Delta| \neq 0$, there are phases with two, one, or zero Majorana zero modes per edge as the interchain coupling $t_\perp$ is increased (the phase boundaries are the same as those in Figure 2.6). The phase with two Majorana zero modes per edge is protected by translation symmetry, which here just amounts to exchange. To distinguish the phases, we only need to independently test whether the $k_y = 0, \pi$ chains are in the topological or trivial phases

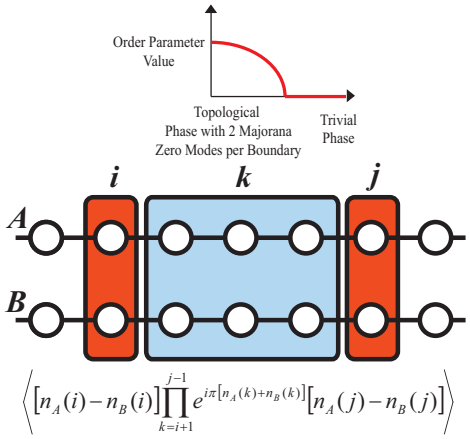

Figure 2.9: Geometry of the nonlocal order parameter Eqs. 2.47, 2.48 for a system of two identical chains A, B (white circles are fermion sites). Bulk (blue) of the order parameter measures fermion parity, while specially chosen terminating operators act on sites of the two chains (orange rectangles) separated by a large distance $|i-j|$. For instance, these terminating operators can be taken to be the fermion number difference $n_A - n_B$. This nonlocal order parameter uniquely identifies the nontrivial phase with two Majorana zero modes per boundary.

using Kitaev model string OPs. In regimes where only one of the $k_y = 0, \pi$ chains is in the topological phase, we use string termination operators such as $\chi_0/\chi_\pi \sim \chi_A \pm \chi_B$ or those built out of $\overline{\chi}$ operators. When both $k_y = 0, \pi$ chains are in the topological phase, the terminating operators are for instance $\chi_0\chi_\pi \sim \chi_A\chi_B$. In other words, two copies of the topological phase OP of the Kitaev model, one for each of the $k_y = 0, \pi$ momentum chains, detects the weakly coupled regime of this two chain system, in which each end has two Majorana zero modes. This is equivalent to a product of topological string OPs for each chain,

$$\left\langle \overline{\chi}_0(i)\overline{\chi}_\pi(i) \prod_{j=i+1}^{k-1} e^{i\pi[n_0(j)+n_\pi(j)]} \chi_0(k)\chi_\pi(k) \right\rangle \rightarrow \left\langle \overline{\chi}_A(i)\overline{\chi}_B(i) \prod_{j=i+1}^{k-1} e^{i\pi[n_A(j)+n_B(j)]} \chi_A(k)\chi_B(k) \right\rangle. \quad (2.47)$$

Taking products of string order parameter works here because of the additional protecting symmetry.

Can we instead choose an order parameter for the two chain system which involves only fermion parity – and hence is easily measurable – but which nonetheless detects a phase with symmetry-protected topological order? In fact, to detect the phase with two Majorana zero-energy modes per edge, the selection rules of Section 2.4 require that the terminating

operators of a NLOP be bosonic (even under parity) but odd under exchange symmetry (see Table 2.2). Therefore,

$$\left\langle (n_A(i) - n_B(i)) \prod_{j=i+1}^{k-1} e^{i\pi[n_A(j)+n_B(j)]} (n_A(k) - n_B(k)) \right\rangle \tag{2.48}$$

will detect the phase labeled Class 2 in Table 2.1 (see Figure 2.9 for an illustration). This NLOP works, for instance, for a model of two identical chains with intrachain pairing and interchain diagonal hopping. While it vanishes for the special model, Eq. 2.46, because of the model's larger symmetry group, for models with no additional symmetries this order parameter detects a topological phase.

2.6 Conclusion

In this chapter, we discussed how to construct string or brane nonlocal order parameters for fermionic phases, focusing in particular on interacting topological superconductors of spinless fermions. These order parameters measure fermion parity in their bulk and are terminated by fermionic or bosonic operators at their edges. We illustrated how they probe the different nature of the Majorana pairings in the topological and trivial phases. The addition of translation to the system as a protecting symmetry (Section 2.4) distinguished among certain interesting 2D phases in the quasi-1D limit. We elaborated on how two 1D $\mathbb{Z}_2$ invariants are identified by the classification in the case of free fermions. In particular, this allows us to distinguish the 2D Chern number mod 2, for instance the $p + ip$ strong topological superconductor and the weak topological superconductor.

We constructed simple general rules (Section 2.4) which the terminating operators of a nonlocal order parameter should satisfy in order to uniquely distinguish among the fermionic symmetric phases (four for N even and two for N odd). Attempts at extending string to brane order for coupled chains have been discussed in other contexts. Crucially, here we were able to make the extension to multiple chains because of the additional protecting $\mathbb{Z}_N$ symmetry, which enabled us to take products of single chain string order parameters.

Our motivations for these simple constructions largely arose from the ability to perform nonlocal measurements in ultracold atomic systems using the quantum gas microscope (Section 2.5). We gave an example of an order parameter for two chains which only involves fermion parity and hence can be used to detect a topological phase using current experimental techniques.

2.7 Appendix A: Applying a Broken Symmetry on a Domain

Consider a quasi-1D spin system with an infinite dimension indexed by j and which has a discrete broken symmetry operator $u = \prod_{j=-\infty}^{\infty} u_j$. We argue that any state $|\psi_0\rangle$ in the ground state manifold obeys $\lim_{N\to\infty}\langle\psi_0|\prod_{j=-N}^{N} u_j|\psi_0\rangle \to 0$, with a special ordering of the limits. It applies even when mapped to fermions because it considers arbitrary ground state choices.

Let $\{|\eta_i\rangle\}_{i=1}^{M}$ be the broken symmetry states which are mapped to each other under u. We explain that $\lim_{N\to\infty}\langle\eta_i|\prod_{j=-N}^{N} u_j|\eta_k\rangle \to 0$ for any i, k. If $i = k$, u creates a finite-sized domain which is orthogonal to the original state as the domain size increases $N \to \infty$. For instance, for the quantum Ising model with a $\mathbb{Z}_2$ broken symmetry,

$$\lim_{N\to\infty}\langle\uparrow,\downarrow|\prod_{j=-N}^{N}\sigma_j^x|\uparrow,\downarrow\rangle \to 0, \tag{2.49}$$

where $|\uparrow\rangle, |\downarrow\rangle$ denote the broken symmetry states in the thermodynamic limit. Off-diagonal matrix elements $i \neq k$ also vanish due to the order of our limiting procedures; since the thermodynamic limit precedes $N \to \infty$, there is always an infinite region outside the domain $[-N, N]$ where the broken symmetry states are orthogonal. Practically, this means that the system size must be much larger than the domain over which the broken symmetry is applied in order to yield an asymptotically vanishing value. We expect that our description can be formalized with matrix product states by considering the eigenvalue problem of the transfer tensor $\mathbb{T}$ governing the behavior of state overlaps.

2.8 Appendix B: Fermionic Classification

We follow the approach developed in [13] for 1D fermionic and bosonic systems. Consider the system Ω with periodic boundary conditions and a unique gapped ground state, and partition $\Omega = \Omega_S \cup \Omega_E$ into a subsystem Ω_S and the environment Ω_E. Let an observable be O. Consider the effective action $\hat{O}$ of this operator in the space spanned by the low entanglement energy (EE) Schmidt states obtained from the ground state on subsystem Ω_S. [13] observed that the action reduces to that of two operators O_L, O_R acting locally near the left and right edges, respectively, of Ω_S, i.e. $\hat{O} \sim O_L O_R$. That is, in this subspace spanned by low EE states, states are distinguished by physics near their edges (as observables have "fractionalized" into two spatially separated pieces) but behave similarly in their bulk. Symmetry-protected phases are distinguished by the commutation relations obeyed by the edge operators.

Our two $\mathbb{Z}_2 \times \mathbb{Z}_N$ commuting symmetry generators are parity and translation P, T. They fractionalize as $\hat{P} \sim P_L P_R$ and $\hat{T} \sim T_L T_R$. We fix $\hat{P}^2 = P_L^2 = P_R^2 = 1$ and $\hat{T}^N = T_L^N =$

$T_R^N = 1$. Define angles μ, μ' with $P_L P_R = e^{i\mu} P_R P_L$, $T_L T_R = e^{i\mu'} T_R T_L$ which are $0, \pi$ since fractional pieces can be fermionic or bosonic.

We claim that μ, μ', along with an additional assumption that $\hat{P} T_L = e^{i\mu'} T_L \hat{P}$, are sufficient to distinguish the quantum phases, since the other commutations follow from these. The complete operator P determines whether operators such as T_L are bosonic or fermionic (value of μ') and it is natural to assume that its effective form does also. Parity is in this way a more fundamental operator for fermionic systems compared to other symmetries. Other commutation relations follow, such as $P_L \hat{T} = \hat{T} P_L e^{i\mu'}$.

An equation such as $P_L \hat{T} = \hat{T} P_L e^{i\mu'}$ imposes a constraint since $P_L^2 = \hat{T}^N = 1$; namely, $\mu' = \pi$ is not allowed if N is odd. Hence, we recover the same symmetric fermionic phases as we would by mapping the bosonic group cohomology classification to fermions: $(\mathbb{Z}_2)^2$ for N even and $\mathbb{Z}_2$ for N odd. We additionally have a direct fermionic description of the phases based on effective forms of symmetry operators. Finally, to establish a correspondence between the bosonic and fermionic descriptions, we should understand when the Jordan-Wigner mapped versions of the fermionic symmetry operators are broken or unbroken in the bosonic variables. This leads us to find that parity is broken when $\mu = \pi$, while translation is broken when $\mu' = \pi$ *and* $\mu = \pi$; this is summarized in Table 2.1.

2.9 Appendix C: Fermionic Selection Rules

We sketch a proof that the terminating operators should satisfy certain selection rules in order for the NLOP to remain nonzero in one symmetric fermionic phase and vanish in the others; the result is Eq. 2.53. We will evaluate the long-distance limit of the string or brane OP $\langle O_L \left[\prod_{j\in\Omega_S} \Sigma_j\right] O_R\rangle$ in the ground state, with O_L, O_R local terminating operators and Σ_j an onsite symmetry. The asymptotic form of a nonlocal order parameter in a symmetric phase is really a two-point function of certain operators because symmetries reduce to acting on the edges of the domain over which they are applied. We use the effective forms for fermionic symmetries from the fermionic classification; though they are state dependent, we only rely on properties of the phases.

We consider as in Section 2.8 a closed system Ω partitioned into a subsystem Ω_S over which the symmetry Σ acts and an environment Ω_E, on whose edges O_L, O_R act. The ground state has Schmidt decomposition $|\psi\rangle = \sum_a e^{-E_a} |\phi_a\rangle |\eta_a\rangle$ where ϕ_a, η_a are for Ω_S, Ω_E, respectively. We specialize to the case of interest where fermion parity P_{Ω_S} is applied in the bulk. The idea of [13] is that $\langle \phi_a | P_{\Omega_S} | \phi_{a'} \rangle \approx \langle \phi_a | P_{\Omega_S,L} P_{\Omega_S,R} | \phi_{a'} \rangle$ (with effective forms $P_{\Omega_S,L}, P_{\Omega_S,R}$ on Ω_S) for states with low entanglement energy (EE), so that $a, a' < \chi$ with χ a cutoff. The forms $P_{\Omega_S,L}, P_{\Omega_S,R}$ are localized to a distance l near the edges of Ω_S which increases with χ. While the replacement by effective forms is approximate, it is good because states with high EE contribute less to evaluations of observables. Hence,

$$\langle \psi | O_L P_{\Omega_S} O_R | \psi \rangle \approx \sum_{a,a'<\chi} e^{-E_a - E_{a'}} \langle \phi_a | P_{\Omega_S,L} P_{\Omega_S,R} | \phi_{a'} \rangle \langle \eta_a | O_L O_R | \eta_{a'} \rangle$$

$$= \sum_{a,a'<\chi} e^{-E_a - E_{a'}} \langle \phi_a | \langle \eta_a | O_L P_{\Omega_S,L} P_{\Omega_S,R} O_R | \phi_{a'} \rangle | \eta_{a'} \rangle$$
$$\equiv \langle \tilde{\psi} | O_L P_{\Omega_S,L} P_{\Omega_S,R} O_R | \tilde{\psi} \rangle, \tag{2.50}$$

where $|\tilde{\psi}\rangle \equiv \sum_{a<\chi} e^{-E_a} |\phi_a\rangle |\eta_a\rangle$ is a good approximation to ground state ψ. We first take the thermodynamic limit of the closed system and then Ω_S so that the evaluations at the left and right boundaries of Ω_S near Ω_E decouple. The NLOP reduces to an evaluation of local operators,

$$\langle \psi | O_L P_{\Omega_S} O_R | \psi \rangle \approx \langle \tilde{\psi} | O_L P_{\Omega_S,L} | \tilde{\psi} \rangle \langle \tilde{\psi} | P_{\Omega_S,R} O_R | \tilde{\psi} \rangle. \tag{2.51}$$

We then take the limit $\chi, l \to \infty$, so $P_{\Omega_S,L}, P_{\Omega_S,R}$ penetrate further into the bulk of the (infinite) subsystem S, $|\tilde{\psi}\rangle \to |\psi\rangle$, and the approximation improves.

Consider the transformation properties of just one edge evaluation, $\langle \tilde{\psi} | O_L P_{\Omega_S,L} | \tilde{\psi} \rangle$, for instance. $P_{\Omega_S,L}$ has known transformation rules under the symmetries which are characteristic of the quantum phase. How must O_L transform in order to force the expression to vanish? $|\tilde{\psi}\rangle$ is approximately an eigenstate of the effective forms of the total symmetries P_Ω, T_Ω, becoming exact in the above limits. Consider introducing translation, for instance,

$$\langle \psi | O_L P_{\Omega_S,L} | \psi \rangle = \langle \psi | T_\Omega^\dagger O_L P_{\Omega_S,L} T_\Omega | \psi \rangle$$
$$T_\Omega^\dagger O_L P_{\Omega_S,L} T_\Omega = (T_{\Omega_E}^\dagger O_L T_{\Omega_E})(T_{\Omega_S}^\dagger P_{\Omega_S,L} T_{\Omega_S}) \tag{2.52}$$

(Note that $T_{\Omega_S}, P_{\Omega_S}$ are bosonic). From Section 2.8, we have $T_{\Omega_S}^\dagger P_{\Omega_S,L} T_{\Omega_S} = e^{i\mu'} P_{\Omega_S,L}$. In order to have $\langle O_L P_{\Omega_S,L} \rangle \neq 0$, we need $T_{\Omega_E}^\dagger O_L T_{\Omega_E} = e^{-i\mu'} O_L$. Applying the same argument with parity symmetry and using $P_{\Omega_S}^\dagger P_{\Omega_S,L} P_{\Omega_S} = e^{i\mu} P_{\Omega_S,L}$ implies $P_{\Omega_E}^\dagger O_L P_{\Omega_E} = e^{-i\mu} O_L$ is needed also. When the terminating operator O_L satisfies transformation laws different from the one characterizing the quantum phase (μ, μ') of the system, the local evaluation $\langle \psi | O_L P_{\Omega_S,L} | \psi \rangle$ will vanish asymptotically. In summary, we need,

$$P^\dagger O_L P = e^{-i\mu} O_L$$
$$T^\dagger O_L T = e^{-i\mu'} O_L \tag{2.53}$$

so that the NLOP vanishes in the fermionic symmetric phases characterized by angles different from (μ, μ'). These selection rules support the conclusions reached using bosonic selection rules and local order parameters for bosonic symmetry breaking. For instance, a NLOP for Class 2 $(\mu, \mu') = (0, \pi)$ should have O_L, O_R chosen to be even under fermion parity and odd under translation, as described in the main text.

Chapter 3

Many-body Localization, Topological Phases, and Quantum Coherence

Many of the earliest advances in solid-state physics originated from the study of crystalline systems. The treatment of electronic behavior in a periodic lattice can be simplified mathematically because of translation symmetry; for instance, energy eigenstates can be labeled by their crystal momentum $\vec{k}$, as expressed by Bloch's theorem. This laid the foundations for the many developments in and successes of electronic band theory.

In contrast, it has taken longer to understand the effects of quenched disorder. A seminal advance was made in 1958 by P.W. Anderson [57] who identified the hallmark phenomenon known as *Anderson localization*. Anderson's work demonstrated that disorder can induce localization of single-particle wavefunctions. This physics is already evident in a simple non-interacting model,

$$H = \sum_i W_i c_i^\dagger c_i + \sum_{i \neq j} t_{ij} c_i^\dagger c_j, \tag{3.1}$$

where, for instance, W_i can be drawn from a distribution with bandwidth W and $t_{ij} \equiv t$ can be taken to be uniform and finite for nearest neighbors. When the dimensionless ratio W/t exceeds a critical value, the single-particle wavefunctions are localized: they are concentrated in real space $\psi(\vec{r}) \sim e^{-|\vec{r}-\vec{r}_0|/\xi}$ with ξ the *localization length.* This behavior can be understood qualitatively by thinking of a perturbative expansion in small t/W. Unperturbed single-particle eigenstates are of the form $c_i^\dagger|0\rangle$ with a broad distribution of energies $\{W_i\}$ due to large W. Nonzero hopping causes a weak mixing of these states: when the randomness is strong, states that are near in real space are generally off-resonant, with a large energy difference ΔE, while states that are close to resonant have weak overlap. The effect of near resonances in higher orders of perturbation theory must be treated carefully, but for the noninteracting problem the localization is stable even for finite t/W.[1]

[1] These resonances arise in the interacting version of the same problem and are mathematically nontrivial to treat.

A prolific body of theoretical and experimental work on disordered systems followed that of Anderson. Among these, single-particle localization was established for all energies in one [58] and two spatial dimensions. In three dimensions, states above a critical energy, the mobility edge, transition from being localized to extended. These results are encompassed within the scaling theory of localization, starting with early work by Thouless and subsequently in [59].

Transport is, of course, directly affected by localization. Due to the absence of a mobility edge, in one and two dimensions the conductivity $\sigma(T) = 0$ at all temperatures T in the absence of inelastic processes. In three dimensions, conductivity follows an Arrhenius law due to thermal excitations above the mobility edge. Inelastic processes make interesting modifications to the conductivity. Mott's theory of variable-range hopping [60], for instance, established how transport can be restored due to coupling of the electronic system with a bath of gapless excitations, such as phonons, available in the medium. Electrons are able to hop between localized single-particle states by exchanging energy with the bath while remaining below the mobility edge. The predicted temperature dependence for the nonzero conductivity is

$$\sigma(T) = \sigma_0(T) \exp\left[-\left(\frac{T_0}{T}\right)^{\frac{1}{d+1}} \right] \tag{3.2}$$

in d dimensions. While the form of $\sigma_0(T)$ depends on the particular bath coupled to, the presence of the exponential is a rather universal feature.

The possibility of recovering transport by coupling to a bath raises some interesting physics question. What are the necessary ingredients for such a bath? In particular, for localized electrons, could electron-electron interactions by themselves play the role of the reservoir? In the other words, must the properties of single-particle localization necessarily be washed out in the presence of only weak and short-range electron-electron interactions?

3.1 Introduction to Many-Body Localization

In 2006, Basko, Aleiner, and Altshuler [61] provided a rigorous mathematical treatment of precisely this question – the effect of electron-electron interactions on a localized and isolated electronic system – using infinite-order perturbation theory. They established the possibility of a localized phase that is stable to weak, short-range interactions and whose DC conductivity $\sigma(T)$ vanishes *exactly* below a critical temperature T_c. Above T_c, a metallic phase is stable. Such a phenomenon is termed *many-body localization* (MBL). The vanishing of the DC conductivity at finite temperatures makes such an insulator quite different from other insulators.

While the calculations in [61], which rely on the self-consistent Born approximation, are mathematically involved, we recapitulate some of the physics with the following Hamiltonian,

$$H \equiv H_0 + H_1 = \sum_{\alpha} \epsilon_\alpha c_\alpha^\dagger c_\alpha + \sum_{\langle \alpha\beta\gamma\delta \rangle} V_{\alpha\beta\gamma\delta} c_\alpha^\dagger c_\beta^\dagger c_\gamma c_\delta, \tag{3.3}$$

consisting of a noninteracting problem H_0 with localized single-particle eigenstates at all energies $\{\epsilon_\alpha\}$ and weak, short-range interactions $V_{\alpha\beta\gamma\delta}$ which couple these states. We can imagine the many-body eigenstates in the $V_{\alpha\beta\gamma\delta} = 0$ limit as occupying the corners of a high-dimensional hypercube, d^N corners for a system with N sites and local Hilbert space of dimension d. Nonzero $V_{\alpha\beta\delta\gamma} \neq 0$ creates particle-hole excitations which couple these unperturbed eigenstates and could in principle lead to delocalization. It is surprising and nontrivial, then, that [61] found $V_{\alpha\beta\delta\gamma}$ need not modify the fundamental nature of the unperturbed eigenstates, rather creating "dressed" eigenstates that are locally modified, akin to localization in many-body Fock space.

Connection to Thermalization and Quantum Statistical Mechanics

As alluded to by the earlier analogy of an electronic system serving as its own bath, there turns out to be an intimate connection between many-body localization and quantum thermalization. The results of [61] in essence entail that for a fully isolated system of interacting electrons which is many-body localized, in any generic partition of the system into a small subsystem A (whose size remains $\mathcal{O}(1)$ in the thermodynamic limit) and its complement A^c, the complement cannot act as a reservoir, in the thermal sense, for A. The assumption that a quantum system thermalizes is a key prerequisite in applying statistical mechanics. Hence, quantum statistical mechanics cannot be applied to MBL.

It is tempting to fundamentally define MBL, and pinpoint the lack of equilibrium, as originating from the blocked transport of matter quantities. However, MBL can be extended to systems where there are no conserved quantities. Instead, it is now better understood and appreciated that the more fundamental attributes behind equilibration, involved in the exchanges of subsystem and reservoir, appear to be related to entanglement and decoherence. The reservoir's role is to provide degrees of freedom with which the subsystem can entangle.

With further study, MBL has come to serve as and increasingly be defined as an antithesis to thermalization, thereby partitioning systems into two broad classes: (i) many-body localizing or (ii) thermalizing. Hence, in order to define the full spectrum of MBL characteristics, we next turn to defining quantum thermalization more precisely.

Consider a system with density operator ρ under time evolution according to the Hamiltonian H. Partition the system S into a subsystem A and remainder A^c and take the thermodynamic limit by adding degrees of freedom to A^c. A quantum system thermalizes if, in the long time and large system limit (taken simultaneously), the reduced density operator for every generic subsystem A, $\rho_A(t) \equiv \text{ tr}_{A^c}\rho(t)$, approaches a Boltzmann-Gibbs distribution, $\rho_A^{eq}(T) = \text{ tr}_{A^c} Z^{-1} e^{-H/k_B T}$.

From our understanding of quantum thermalization thus far, it appears that when a system does thermalize at a given temperature, it thermalizes for all choices of initial states.

[62]. If that is the case, the initial state can, in particular, be chosen to be a many-body eigenstate of H. However, since an energy eigenstate has trivial dynamics, we conclude that such a state much be thermal to begin with. This is the content of the *Eigenstate Thermalization Hypothesis* (ETH), a key feature of statistical mechanics in the quantum setting [63–66] which we will equate with thermalization.

One consequence of ETH concerns the entanglement entropy. If energy eigenstate $|n\rangle$ of Hamiltonian H is thermal, then since the reduced density matrix for any subsystem A is equal to a Boltzmann density operator – $\lim_{t\to\infty} \rho_A^n(t) = \rho_A^{eq}(T_n)$ – the entanglement entropy $S = -k_B \operatorname{Tr}_A(\rho_A^n \log \rho_A^n)$ between A and the remainder A^c must be the equilibrium thermal entropy of the smaller subsystem, A, which is extensive in the size of A. Hence, we find that entanglement entropy in thermal eigenstates must obey *volume-law* scaling.

ETH is a hypothesis, rather than a theorem, that has been investigated in numerous contexts and believed to describe the physics behind quantum thermalization. It is difficult to test numerically, since exact calculations are often for small systems and require extrapolation to the thermodynamic limit. The distinction between MBL and ETH will appear in dynamics – for instance, in retention of some local aspects of initial conditions. Hence the transition between the two is termed a "dynamical phase transition," in contrast to an equilibrium one. We note in passing that integrable systems, which have an infinite set of extensive conserved quantities, were studied before MBL and do not thermalize to the usual Boltzmann ensemble. However, MBL is a more general class of nonthermalizing systems; it is, for instance, more robust to generic perturbations, while integrable systems often require fine tuning.

If energy eigenstates are thermal, but a generic initial state is not, how does thermalization come about in the quantum setting? In the basis of energy eigenstates, the diagonal terms of the density operator $\rho(t)$ are independent of time, while the off-diagonal terms oscillate at different frequencies, $\langle n|\rho(t)|m\rangle = \rho_{nm}(t) = \rho_{nm}(0)\exp[i(E_m - E_n)t/\hbar]$. The off-diagonal terms will overall give vanishing contribution to observables due to essentially random phases, leaving behind a diagonal ensemble.

Quantum thermalization is particularly interesting when viewed from an information theoretic perspective. Information cannot be erased from a closed system as a whole because of the unitary dynamics. On the other hand, a thermal system is characterized by only a few macroscopic properties, such as temperature and chemical potential. The essence of quantum thermalization is that the initial information contained in the system – in the form of expectations of local observables – is still present but inaccessible to local probes at long times. Decoherence crucially scrambles any memory of local initial conditions. In contrast, in a localized system, the long-time dynamics of subsystems retain some memory of the local features of the initial state. In our model for a prototypical 1D SPT-MBL, this retention of local memory will be made apparent. Hence, as hinted at earlier, the essence of quantum thermalization appears to be more fundamentally tied to the propagation of information, and the ability of distant degrees of freedom to entangle at long times, rather than originating from lack of transport.

Features of Many-Body Localization

The work of Basko and collaborators [61] presented strong evidence for interesting physics in the MBL regime and spurred numerous further studies. Many of these studies were numerical in nature – as there are limited tractable analytic approaches for disordered interacting systems – and used spins model as testbeds for MBL.

Studies by Oganesyan and Huse [67] and Pal and Huse [68] critically examined the many-body localized and thermal phases and the transition between them. A spin model which captures both phases is the one-dimensional spin-1/2 random field Heisenberg Hamiltonian,

$$H = \sum_i \left(h_i \sigma_i^z + J \vec{\sigma}_i \cdot \vec{\sigma}_{i+1} \right), \tag{3.4}$$

with h_i drawn from a distribution of bandwidth h. The conservation of total z-spin in this model is not a necessary feature. With no interactions $J = 0$, this model is localized in all energy eigenstates. These features remain for nonzero J and the system is many-body localized in all eigenstates of the spectrum. A thermal phase exists at large J. Various diagnostics can be used to distinguish the phases, such as (i) partial memory of an initial condition, for instance the ability to relax an initially inhomogeneous spin density, and (ii) comparison of local observables in or subsystem density operators of full density operators ρ^n, ρ^{n+1} of adjacent energy eigenstates with energies E_n, E_{n+1}. If they are thermal, adjacent energy eigenstates must thermalize to temperatures which are exponentially close in system size, and averages of local observables should become increasingly similar. In contrast, adjacent localized states have local differences which persist even in the thermodynamic limit [68].

Another distinction between MBL and thermal phases manifests in the statistics of spectral gaps of adjacent eigenstates of the Hamiltonian. Thermal phases are known to exhibit spectral statistics given by the Gaussian Orthogonal Ensemble (GOE). A key feature of the distribution dictated by the GOE is level repulsion, characteristic of avoided level crossings: the probability density governing the distribution of energy gaps vanishes as the gap itself vanishes. In contrast, nearby energy states which are localized appear different locally and, qualitatively speaking, are invisible to each other under perturbations. They display Poisson level statistics and no level repulsion. Studying the distribution of spectral gaps is therefore helpful in separating localized and thermal phases [67].

At the time of writing, many-body localization continues to be vigorously studied through a combination of numerical and analytical approaches as well as experiments. An early paper by [69] used creative modifications to strong disorder renormalization group [70–72] – an approach that had been of great use in studying ground state properties of strongly disordered low-dimensional quantum systems – to obtain the physics of the localized phase after long time evolution. A Hamiltonian with strong quenched disorder has a hierarchy of energy scales, and the strong disorder renormalization group tracks the flow of the probability distribution of Hamiltonian couplings by perturbatively eliminating the largest terms in the

Thermal Phase	**Single-particle Localized**	**MBL**
ETH holds	ETH false	ETH false
May have nonzero DC conductivity	Zero DC conductivity	Zero DC conductivity
Continuous local spectrum	Discrete local spectrum	Discrete local spectrum
Volume-law entanglement of eigenstates	Area-law entanglement of eigenstates	Area-law entanglement of eigenstates
Power-law spreading of entanglement	No spreading of entanglement	Logarithmic spreading of entanglement
Dephasing, dissipation	No dephasing or dissipation	Dephasing, no dissipation

Table 3.1: Several key differences among thermal, single-particle localized, and MBL phases. Reproduced from [62].

Hamiltonian first. Likewise, time evolution for a strongly disordered system will contain a hierarchy of time scales. [69] perturbatively eliminated the fastest time scales in favor of slower ones and was able to identify a fixed point of the MBL dynamics. Their approach revealed that, in the localized phase, the long time limit is characterized by an emergent, infinite set of *local* integrals of motion which become exact conservation laws at the fixed point. This finding was an early indicator of the hidden local integrability of fully localized systems, as we will discuss in Section 3.2.

The setting for observing features of MBL is a fully or nearly isolated interacting system. Conventional materials have hitherto been a difficult platform because of the multitude of uncontrolled gapless modes which are present and can serve as a thermalizing reservoir for the electronic subsystem. Ultracold atomic systems, on the other hand, can be more easily isolated or controllably connected to a bath, as well as tuned through a variety of phases, and hence are a natural setting for studying localization. [73] was the earliest conclusive experimental study for MBL at finite-energy density. They prepared a one-dimensional system of ultracold fermions in a quasi-random disordered lattice. Relaxation of an initial charge density distribution indicated the MBL or ETH nature of the phase.

We close with Table 3.1 from [62] which highlights some of the key distinctions between thermal, single-particle localized, and many-body localized systems. A few remaining properties will be discussed in the following section.

3.2 Emergent Local Integrability

The dynamical renormalization group implemented by [69] offered early hints that a MBL system might have emergent integrals of motion. Indeed, for systems with Hamiltonian H whose entire energy spectrum is many-body localized, it was initially argued [74–77] and later rigorously proven [78, 79] that they are governed by a complete set of *quasi-local* integrals of

motions, that is, a set of local operators (with possibly exponentially decaying tails) which commute with each other and with H. The understanding of fully many-body localized systems as ones with emergent integrability, in terms of local operators, provides a deeper explanation for the key features of the MBL phase highlighted previously.

We describe this most simply for a spin-1/2 system following the example and terminology in [74]. Consider a random, short-range interacting Hamiltonian H defined in terms of Pauli operators $\{\vec{\sigma}_i\}$ which live on the physical sites. We term these operators "p-bits" for physical bits; they are the observables accessible experimentally via local probes. If the full spectrum of H is many-body localized, it will have a complete set of local integrals of motion, $\{\tau_i^z\}$. Each τ_i^z is one component of a set of Pauli operators $\vec{\tau}_i$. We will refer to the $\{\vec{\tau}_i\}$ as "ℓ-bits" for localized bits. Furthermore, the statement of local integrability posits that the many-body localized Hamiltonian will take the form [74],

$$H = \sum_i h_i \tau_i^z + \sum_{ij} J_{ij} \tau_i^z \tau_j^z + \sum_{n=1}^{\infty} \sum_{i,j\{k\}} J^{(n)}_{i\{k\}j} \tau_i^z \tau_{k_1}^z ... \tau_{k_n}^z \tau_j^z, \tag{3.5}$$

consisting of one-body, two-body, and higher-order interaction terms. The interactions $\{J_{ij}, J_{i\{k\}j}\}$ decay exponentially with distance between the coupled ℓ-bits. Evidently, the eigenstates of H are simultaneous eigenstates of all the τ_i^z operators.

The ℓ-bit operators are to be thought of as dressed versions of the p-bit operators. If the Hamiltonian H were noninteracting and fermionic, for instance, the τ_i^z could be taken to be the occupation numbers of single-particle localized orbitals, and many-body eigenstates would be constructed accordingly. With weak interactions, the stability of the MBL phase and the statement of local integrability results in dressed versions of these which continue to serve as conserved quantities. One avenue towards constructing the ℓ-bit operators is to begin with the p-bits and perturbatively add correction terms to yield operators which commute with H and with each other, order by order in the strength of the p-bit interactions in H. This method is mathematically subtle to implement, giving rise to questions of uniqueness as well as issues surrounding "resonances" – degeneracies at high order in perturbation theory due to distant localized degrees of freedom with similar energies. The formal justification for the statement of hidden integrability lies in a mathematical proof [78, 79], relying on what appears to be a physically reasonable assumption of "limited level attraction," and is similar in spirit to the order-by-order construction described.

A construction of local integrability is not possible in the thermal phase. While every local Hamiltonian has a complete set of integrals of motion – namely, the set of projection operators onto each energy eigenspace, which commute with H by construction and with each other – they are not *local* operators. They can yield a local operator when they are combined together in a specific way, for instance to yield H.

The form Eq. 3.5 underlies many of the properties of the MBL phase. The dynamics of the ℓ-bits is trivial, involving precession at a rate set by the interactions with other ℓ-bits. In a generic state, the ℓ-bits will entangle, but crucially, Eq. 3.5 contains no spin flips – τ_i^x or τ_i^y

terms – which would cause dissipation. In fact, the lack of dissipation suggests a spin echo procedure which attempts to reverse the effect of dephasing has potential for success [80, 81]. The possibility of using a spin echo measurement in the bulk of a many-body localized system was explored in [81] and the calculated response was found to distinguish MBL from single-particle localized and thermal phases. The possibility of spin echo protocols for MBL will be further discussed in the coming sections which describe one contribution of this dissertation [80]. Theoretical support for our conclusions relies heavily on the characterization of fully many-body localized systems in terms of a hidden local integrability.

Entanglement Perspective

The local integrability Eq. 3.5 explains the characteristic growth in entanglement entropy for initially unentangled states in MBL phases, an early indicator of the unusual physics present [82]. From numerical calculations on the dynamics of an initial state under a one-dimensional random-field XXZ Hamiltonian, [82] found a slow, logarithmic growth of entanglement entropy which converged to a final extensive but nonthermal value. This logarithmic growth distinguishes the MBL phase both from the thermal phase and its noninteracting counterpart. An intuitive way [74] to see the origin of the growth is to note that, due to the form of Eq. 3.5, the effective interaction between two ℓ-bits i, j is

$$J_{ij}^{eff} = J_{ij} + \sum_{n=1}^{\infty} J_{i\{k\}j}^{(n)} \tau_{k_1}^z ... \tau_{k_n}^z \tag{3.6}$$

and is expected to fall off exponentially with distance, $J^{eff} \sim J_0 e^{-|i-j|/\xi}$, for some decay length ξ. The effective interaction will take effect past a time scale set by $J^{eff} t \gtrsim 1$, at which points ℓ-bits within a distance $L \lesssim \xi \log(J_0 t)$ will be entangled with each other.

Another striking consequence of MBL is the area-law entanglement entropy in localized eigenstates [83]. In stark contrast, as pointed out earlier, ETH requires that thermalized many-body energy eigenstates have volume-law entanglement entropy. Beyond its deep physical implications, the limited entanglement contained in MBL energy eigenstates enables the development of efficient algorithms for numerical simulations, following analogous methods for area-law ground states of gapped Hamiltonians.

3.3 Order Protected by Localization

Equilibrium statistical mechanics enforces strong constraints on when many-body classical or quantum systems can exhibit order; MBL systems, however, are free from such constraints. One of the most exciting consequences of MBL is that it can in fact *protect* order, giving rise to it in regimes forbidden in equilibrium systems. A variety of orders can be protected in this way [84, 80, 85, 86] including certain symmetry-breaking, symmetry-protected topological, and intrinsic topological orders.

To illustrate how this comes about [84], we restrict attention to the prototypical one-dimensional model for phase transitions, the quantum Ising Hamiltonian. Let the full interacting Hamiltonian H consist of H_0, the noninteracting piece,

$$H_0 = -\sum_i J_i \sigma_i^z \sigma_{i+1}^z + \sum_i h_i \sigma_i^x, \tag{3.7}$$

and an additional Hamiltonian H_1 consisting of weak interactions. For instance, H_1 can be taken to consist of two-body σ^x interactions $H_1 = \sum_i V \sigma_i^x \sigma_{i+1}^x$. The $\{J_i, h_i\}$ are random couplings drawn from distributions with means $\bar{J}, \bar{h}$. MBL allows for the existence of spin-glass long range order in all eigenstates throughout the Hamiltonian spectrum when $\bar{J}$ dominates the other energy scales.

Consider the noninteracting, zero-field limit $V, h_i = 0$. Energy eigenstates contain domain wall excitations localized between lattice sites, as in the state $|\uparrow\uparrow ... \uparrow\downarrow\downarrow\rangle$ written in a basis of σ^z eigenstates. In this one dimensional setting, the domain wall, which lives between lattice sites, is effectively a point particle. The effect of nonzero h_i is to induce motion of the domain walls – hopping of the defects – from site to site. If the system were not localized, as would be the case with uniform $J_i = J, h_i = h$, for instance, the addition of even a weak $h \neq 0$ would cause the eigenstates within a degenerate multiplet, consisting of all possible positions of k domain walls against a background of ordered spins, to immediately split and yield resultant states with delocalized domain walls. In the presence of disordered couplings, however, the problem is that of single-particle localization – the domain wall defects are particles which hop due to h_i and experience a disordered background potential J_i – and hence will remain localized. The localization of domain walls is furthermore stable to turning on weak interactions, such as $V_i \neq 0$, due to the stability of MBL. Localization of domain wall defects implies correlation of spins at long distances; the long range spin-glass order will manifest in $\lim_{|i-j|\to\infty} |\langle \sigma_i^z \sigma_j^z \rangle|$ approaching a constant value. The many-body eigenstates in the large $\bar{J}$ limit will come in pairs corresponding to the breaking of $\mathbb{Z}_2$ symmetry. Strikingly, this will hold in *every energy eigenstate* in the spectrum of H.

This chain of reasoning is equally valid for fermionic Hamiltonians, such as the Majorana chain with weak density-density interactions obtainable from the interacting quantum Ising model above. In this case, the spin-glass order at high energy densities manifests itself as symmetry-protected topological order.

We now turn to the main contributions of this thesis to the intersection of many-body localization, symmetry-protected topological order, and quantum coherence. A key result will be our demonstration that the unique combination of SPT and MBL, which we will abbreviate as SPT-MBL, enables preservation and manipulation of quantum information in quantum bits at arbitrarily high energy densities.

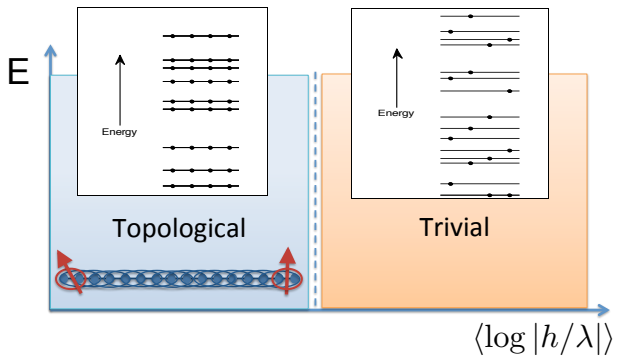

Figure 3.1

3.4 A 1D Model for SPT-MBL

The model we will use to demonstrate the existence of protected edge states and quantum coherence at high energies is the following one-dimensional spin-1/2 Hamiltonian,

$$H = \sum_i \left(\lambda_i \sigma_{i-1}^z \sigma_i^x \sigma_{i+1}^z + h_i \sigma_i^x + V_i \sigma_i^x \sigma_{i+1}^x \right). \tag{3.8}$$

The couplings λ_i, h_i and V_i are independent random variables. The Hamiltonian has two $\mathbb{Z}_2$ symmetries corresponding to the mapping $\sigma_a^{z,y} \to -\sigma_a^{z,y}$ independently on the even and odd numbered sites, which, as we will see, are important protecting symmetries for symmetry-protected topological order. The first two terms of Eq. 3.8 can be mapped to a noninteracting Majorana fermion model using a Jordan-Wigner transformation [87]. However, probe fields which couple to the spins may appear in a nonlocal and hence unnatural manner in the fermionic variables, limiting the usefulness of the mapping; our natural variables will be the spins. The last term V_i adds interactions in the fermionic language, making the model generic. We will work in the limit of strong disorder and weak interactions so that the stability of the MBL phase is guaranteed.

There are two simple limits in which the Hamiltonian Eq. 3.8 is trivially diagonalizable and which characterize the physics of two distinct dynamical phases. With only local fields $\{h_i\}$ present, the system is single-particle localized with trivial topological properties. All eigenstates are unentangled product states of the spins in the σ_i^x basis. In contrast, with only the three-spin couplings $\{\lambda_i\}$ present, the system exhibits a single-particle localized phase which is topologically nontrivial at all energy denstities. On a chain with open boundary conditions, this manifests as edge states in each eigenstate. Each energy eigenspace will also be four-fold degenerate. Crucially, the distinction between the two phases persists away from the simple limits described and in the presence of interactions V_i due to the localization. This is yet another example of the protection of quantum order by MBL described in Section 3.3.

A schematic view of the phase diagram, depicting the transition from the trivial to the topological eigenstates with decreasing transverse field h_i, is shown in Figure 3.1. The verti-

cal axis is energy density such that the maximum corresponds to infinite temperature in an equilibrium state. The horizontal axis is a measure of the typical strength of the transverse field h to the three-spin term λ, with spin-1/2 edge states shown in the caricature for small h. The lines show the energy levels for a particular realization of the disordered Hamiltonian Eq. 3.8 corresponding to zero-mean Gaussian couplings with standard deviations of $(\sigma_V, \sigma_\lambda, \sigma_h) = (0.1, 1.0, 0.05)$ on the left, $(\sigma_V, \sigma_\lambda, \sigma_h) = (0.1, 0.1, 1.0)$ on the right. Degenerate multiplets are depicted by the presence of multiple solid dots on a line (displaced from each other for visibility). The topological phase displays a four-fold degeneracy throughout the energy spectrum. While the phase transitions are of interest by themselves, in the remainder of the chapter we focus on the properties deep within a phase, which we turn to next.

Symmetry-Protected Topological Phase

We examine the features of the SPT phase [19, 8] by first considering the integrable limit in which only the λ_i are nonzero in Eq. 3.8. In this limit, the Hamiltonian can be written as the sum of mutually commuting operators $K_i = \sigma^z_{i-1}\sigma^x_i\sigma^z_{i+1}$ called stabilizers, $H_0 = \sum_i \lambda_i K_i$. The eigenstates are mutual eigenstates of all the K_i, labeled by the respective eigenvalues ± 1. Such states, termed cluster states in the quantum information literature, can be constructed by applying projection operators, one choice of P_i^+ or P_i^- per K_i, to an initial state, where $P_i^\pm = \frac{1}{2}(1 \pm K_i)$.

With open boundary conditions, the cluster states display edge modes that behave as free spin-1/2 particles. This is easily seen by constructing a spin-1/2 algebra of edge operators,

$$\Sigma^x_L = \sigma^x_1\sigma^z_2, \Sigma^y_L = \sigma^y_1\sigma^z_2, \Sigma^z_L = \sigma^z_1, \tag{3.9}$$

on the left edge and similarly on the right edge. We say that these edge degrees of freedom behave as free spins because H_0 commutes with them. The $\mathbb{Z}_2 \times \mathbb{Z}_2$ symmetry of odd and even sites described earlier is a protecting symmetry because it prevents the edge spin operators, which are not invariant, from appearing in the Hamiltonian. The protection of the topological phase by the product $\mathbb{Z}_2 \times \mathbb{Z}_2$ symmetry [88] is analogous to the protection of the Haldane phase discussed in Chapter 2.

Note that the free edge spins are not adiabatically connected to the limit of a decoupled physical spin, σ^α_i, but are a genuinely nontrivial quantity (as long as the symmetry is preserved). For example, their components in this limit consist of a product of two spins. Hence, the physics manifest here is different from that of weakly coupled independent spins.

The topological nature of the cluster states is also encapsulated in a string order parameter [1] given by $O_{\rm st}(i,j) = \langle \sigma^z_i \sigma^y_{i+1} \left(\prod_{k=i+2}^{j-2} \sigma^x_k\right) \sigma^y_{j-1}\sigma^z_j \rangle$, assuming the symmetry remains unbroken. In a specific eigenstate and disorder realization, the string order parameter takes random values $O_{\rm st}(i,j) = \pm 1$. We can disorder average the square of this to get a nonlocal analogue of the Edwards-Anderson order parameter for spin glasses, $\Psi_{sg} = \overline{\langle O_{\rm st}\rangle^2}$, which

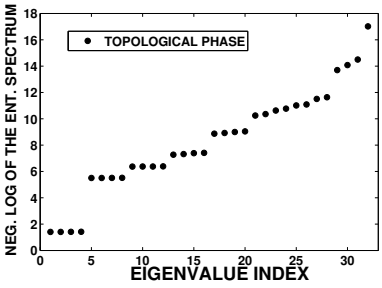

Figure 3.2

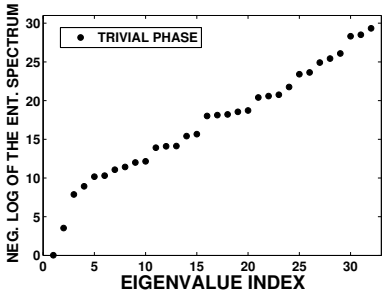

Figure 3.3

here gains a nonzero expectation value in the topological glass. We emphasize that this order is found in eigenstates of H_0 at all energies.

Another manifestation of symmetry-protected topological order lies in the entanglement spectrum [7]. To demonstrate this, we pick an eigenstate of the system on a ring and compute the reduced density matrix ρ_A for half of the ring, subsystem A, tracing over the degrees of freedom of its complement, A^c, from the full density matrix, $\rho_A \equiv \text{tr}_{A^c}\rho$. The eigenspectrum of ρ_A yields the entanglement spectrum and will be four-fold degenerate in the SPT phase, which can be understood as a reflection of a "virtual" spin-1/2 at each end of the cut.

Figure 3.3 contrasts the entanglement spectrum of an excited state in the topological state and the trivial state. The four-fold degeneracy is evident in the topological phase. The vertical axis plots the negative logarithm of the eigenvalues of ρ_A, i.e. the eigenvalues of the entanglement Hamiltonian $\mathcal{H}_A$ constructed as $\rho_A = e^{-\mathcal{H}_A}$. The numerical results are for an eigenstate near the middle of the spectrum on a periodic system of ten sites. Finite-size effects are also evident and expected for contributions with higher index on the horizontal axis.

Effect of Interactions

We now consider adding to the Hamiltonian H_0 generic perturbations such as h_i and V_i in Eq. 3.8 which destroy its integrability but still preserve the $\mathbb{Z}_2 \times \mathbb{Z}_2$ symmetry of the problem. Due to the limit of strong disorder, we are guaranteed that eigenstates at all energies will be localized. Consequently, in this fully MBL state, one can identify the quasi-local integrals of motion of Section 3.2. We will rely on this connection heavily to describe the localized topological phase and interpret numerical results for the dynamics.

The eigenstates of the toy model discussed above were the strictly localized cluster states. Assuming localization persists on adding the interaction terms, the local stabilizers K_i will map to a set of commuting integrals of motion $\tilde{K}_i$ that are still local up to an exponentially decaying tail. Like the original stabilizers K_i, each $\tilde{K}_i$ is one projection of a spin-1/2 variable. Similarly, in a semi-infinite system, the edge operator Σ_L^α localized on the open edge will map to a quasi-local left edge operator $\tilde{\Sigma}_L^\alpha$ that remains decoupled from the bulk Hilbert space.

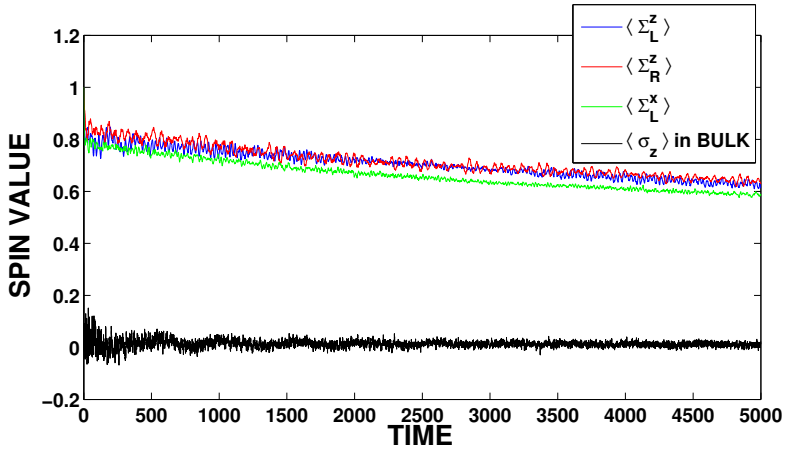

Figure 3.4

Experiments can have direct access only to simple, strictly local operators such as the original edge operators Σ_L^α and not to the operators that are exactly conserved $\tilde{\Sigma}_L^\alpha$. However, because the system is in the localized phase, the measurable quantity Σ_L^α has strong overlap with the true edge operator. More precisely, we can write the original edge operator as a sum of a left edge contribution and a bulk contribution,

$$\Sigma_L^\alpha = Z_\alpha \tilde{\Sigma}_L^\alpha + c_\alpha \tilde{O}_B^\alpha. \tag{3.10}$$

If we start the dynamics with Σ_L^α fully polarized in the α direction, then a polarization of Z_α will remain after arbitrarily long time evolution. However, for a finite size system, rather than a semi-infinite chain, the nonlocal tails of the new edge operators can lead to interactions between the two edges and the bulk of the system through terms of the form

$$H_{\text{edge}} = \sum_{\alpha,\beta,m} J_m^{\alpha\beta} \tilde{\Sigma}_L^\alpha \tilde{B}_m \tilde{\Sigma}_R^\beta \tag{3.11}$$

A large number of non-local bulk operators B_m are possible and the respective coefficients are all exponentially small in the system size. The different terms give rise to oscillations at a large number of frequencies. This in turn will lead to decay of the edge spin over a time T_0 that scales exponentially in the system size N. For the integrable system with $V_i = 0$, only a few interedge coupling terms can occur. This is observed explicitly in the oscillation of the edge spin at a small number of frequencies, as shown in Figure 3.10.

Results from numerical diagonalization of the model Eq. 3.8 on a chain with up to eleven spins are shown in Figures 3.4, 3.5, 3.7. In one set of calculations, done in a parameter regime deep in the topological phase, the system is initialized in a product state with all spins polarized along σ^z, so that the bare edge operator Σ_L^z has a definite value +1. In another set of calculations, we retain the initial conditions above except polarize the first spin along polarized along σ^x so that Σ_L^x has a definite value. In both cases the spin expectation value

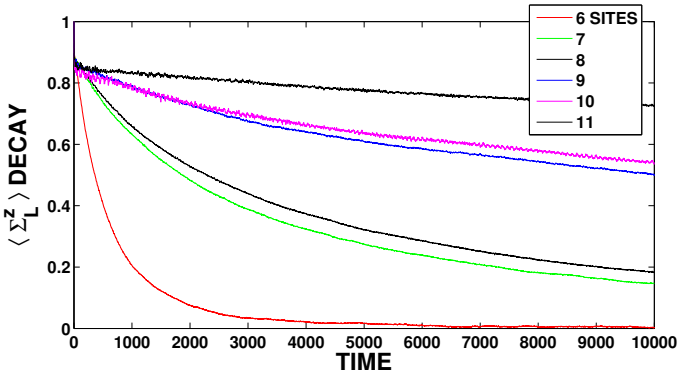

Figure 3.5

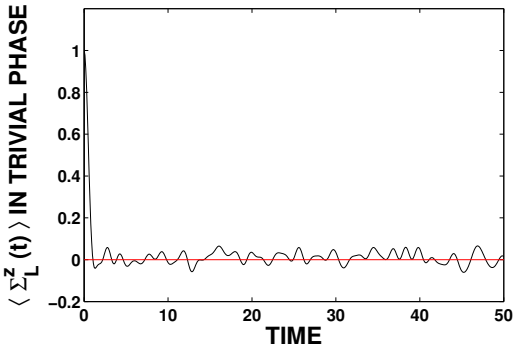

Figure 3.6

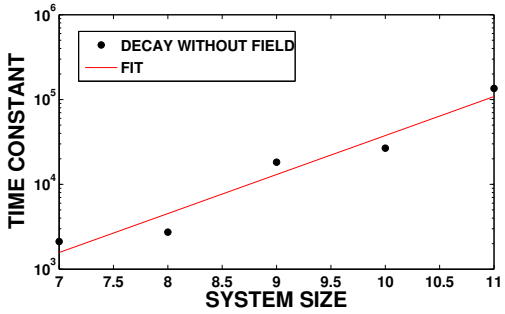

Figure 3.7

first drops to a smaller nonvanishing value, which later decays to zero on a much longer time scale which we label T_0 (Figure 3.4).[2] A σ^z measurement in the bulk, in contrast, does not persist and decays rapidly to zero.

Moreover, Figure 3.6 provides further evidence that the persistence of the edge spin is a property of the SPT phase only. In the trivial phase of an eight-site chain, the same edge spin operator $\Sigma^z_L = \sigma^z_1$ decays rapidly to zero.[3]

The strong dependence of T_0 on the system size is evident in Figure 3.5, and in Figure 3.7 we demonstrate the exponential growth of this time. Hence, the SPT-MBL phase has free spin-1/2 edge states at all energies in the thermodynamic limit.

[2]Refer to Section 3.8 for details on how T_0 was extracted.

[3]Note that while $\langle \sigma^x_i \rangle$ may persist in the trivial phase both in the bulk and on the edge, other spin components are not conserved and hence there is no preserved *quantum* spin.

3.5 Quantum Dynamics and Spin Echo

Even without thermalizing, it is not *a priori* obvious that a many-body quantum system in practice can have retrievable quantum coherence. While the hidden local integrability of Section 3.2 did argue for dephasing, rather than dissipative, dynamics from the Hamiltonian, there are further issues to address. The time evolution of an initial state generally involves unbounded growth of the entanglement entropy in the MBL state [82], which might suggest some irreversible loss of information: how would one implement a protocol to try to reverse this in a useful way, and over which degrees of freedom? Furthermore, in practice our quantum state preparation and measurements are done in a different basis (the basis of p-bits rather than ℓ-bits, using the language of Section 3.2), which slightly complicates the analysis.

Dephasing Time in a Symmetry-Breaking Field

First, we discuss the degree to which the edge spin can be manipulated coherently. Consider coupling the addressable edge spin to a local, albeit symmetry-breaking, field $H_{\text{ext}} = g\Sigma_L^x$. Since we are in the MBL phase, there is still a constant of motion $\tilde{\Sigma}_L^x$ directly related to Σ_L^x. However, because the field breaks the protecting $\mathbb{Z}_2 \times \mathbb{Z}_2$ symmetry, it induces coupling between the edge operator and the bulk,

$$g\Sigma_L^x = gZ\tilde{\Sigma}_L^x + g\sum_{n,\alpha} c_\alpha^n \tilde{\Sigma}_L^\alpha \tilde{B}_\alpha^n. \tag{3.12}$$

While in the idealized cluster model where only $\lambda_i \neq 0$, such a field would have caused oscillations at a single frequency $\omega = g$, the edge spin now precesses with many frequencies, leading to decoherence. The decoherence time is independent of system size, set only by the magnitude of the field g and the intrinsic interactions that determine the coefficients c_α^n. By weak analogy with terminology from nuclear magnetic resonance (NMR), we term this a dephasing time T_2^*. Figure 3.13 shows that indeed T_2^* is, to a good approximation, independent of system size. The dephasing time which we extract from disorder averaging over independent realizations is shown in Figure 3.9, where it can be compared to several other times scales.

At a glance, this kind of dephasing with an infinite number of intrinsic modes appears deadly to the quantum coherence of the edge spin. However, note that all the terms causing the dephasing of the edge modes are proportional to the external field g, or more generally to an odd power of it (see Section 3.7). Reversing this field reverses the oscillations terms and can lead to a spin echo. The overlap between initial and final states is less than unity but finite and expected to persist to infinite time in the thermodynamic limit. In a finite-size system, there is an additional imperfection due to the field-independent coupling between the two edges which is exponentially small in the system size. We now describe the field reversal protocol more precisely.

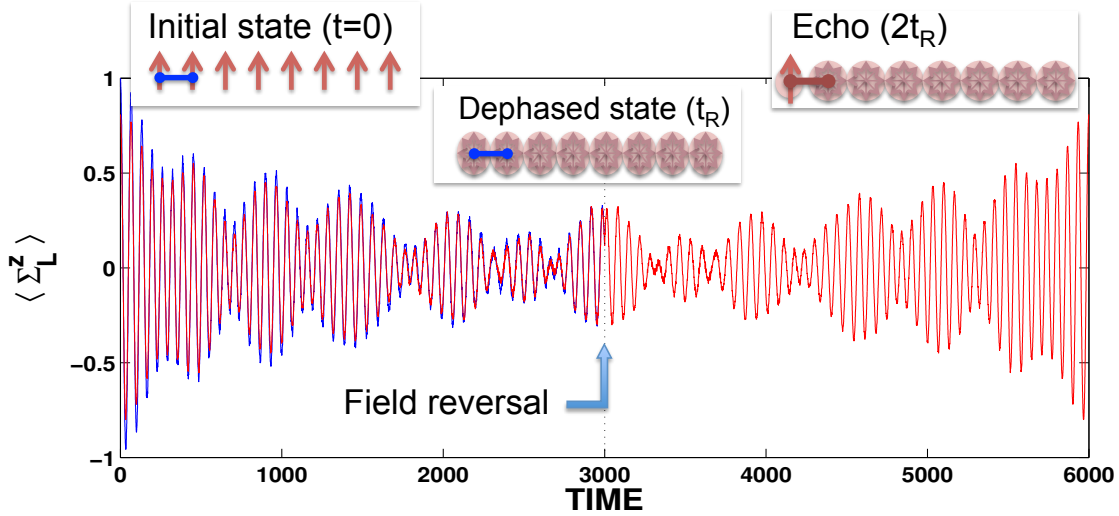

Figure 3.8

Fidelty of a Spin Echo Protocol

To test the degree of edge coherence, we compute the time evolution of the edge spin in the model Eq. 3.8 supplemented by a local field $g\Sigma_L^x$ applied at one end of a chain. Figure 3.8 shows an example of the dynamics in a specific disorder realization for an eight-site chain, starting from a definite value of the left edge Σ_L^z. As expected, oscillations of $\langle\Sigma_L^z\rangle$ are visible and decay on the time scale characterized as T_2^*. At time t_R, we reverse the field g and observe a near perfect retracing of the oscillations. We then compute the overlap of the final state at $2t_R$ with the initial state. The edge spin echo fidelity degrades slowly with increasing the reversal time t_R, from which we can extract a relaxation time which we term T_2, again by analogy with NMR terminology. It is remarkable that here T_2 increases exponentially with growing system size, as shown in Figure 3.9. This implies that in the thermodynamic limit, the edge spin can indeed maintain truly perfect coherence in spite of it being embedded in an interacting many-body system with high energy density.

In spite of the numerous integrals of motion, the bulk of the system reaches, for all practical purposes, an infinite temperature. This is because the initial product states we are using do not constrain the value of those integrals of motion. The edge spin on the other hand remains dynamically decoupled from the bulk. While it is possible to perform spin echo protocols in the bulk by constraining those integrals of motion, this would only recover classical information. The presence of the underlying topological phase is crucial for providing a free quantum bit, on the edge of the system, which can be manipulated.

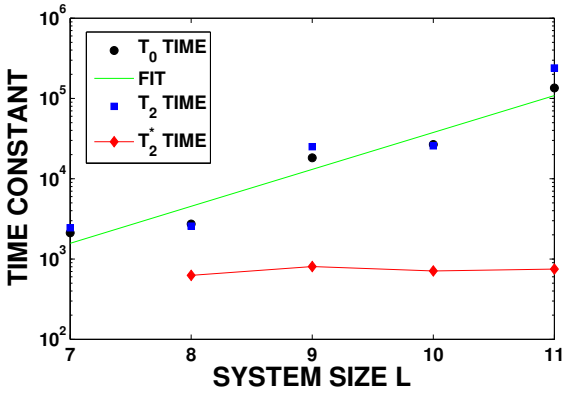

Figure 3.9: Scaling of all the time constants with system size. The zero-field decay time T_0 and spin echo decay time T_2 are nearly identical and scale exponentially with system size, whereas the oscillations decay time T_2^* is size independent. Parameters were zero-mean Gaussians with standard deviations were $(\sigma_V, \sigma_\lambda, \sigma_h) = (0.1, 1.0, 0.05)$.

3.6 Conclusion

The combination of SPT-MBL enables quantum edge states which can persist in arbitrarily high energy eigenstates. Furthermore, a quantum bit at the edge can (i) preserve information in its state, and (ii) this information can be recovered from interacting dynamics which mix the edge with bulk degrees of freedom. These phenomena are summarized in Figure 3.9 by the three characteristic times we have discussed. One of the characteristic times, T_2^*, reflects dephasing at a hierarchy of time scales in the presence of an edge field which mixes the edge and bulk but in a manner that is independent of system size. The remaining two time constants – T_0, characterizing the decay of the spin persistence, and T_2, characterizing decay of the spin echo fidelity – grow exponentially with system size. Hence, edge spin preservation and spin echo fidelity are effects that will remain, saturating at some diminished but nonzero value rather than vanishing, in the thermodynamic limit. These effects serve as a smoking gun signature of the SPT-MBL phase.

These results are more general than the specific model Eq. 3.8 because our numerical demonstration is supported by theoretical analysis relying only on two powerful concepts, namely (i) symmetry and (ii) the existence of a complete set of quasi-local integrals of motion for MBL, which is known to hold in system without a many-body mobility edge. Since MBL is not fine tuned, there is a finite region of parameter space in which the existence of high-energy topological edge states and high-energy quantum coherence will be realized.

The theoretical and numerical investigation of dynamics with physically preparable initial states is one important step in better understanding the consequences of SPT-MBL, particular for experiments. While [84, 83] outlined how a distinction between phases may appear in correlations measured in individual eigenstates, there still remained the question of a physical distinction between them, something that can be probed in an experiment when

working with a generic initial state. Preparing a many-body system in an energy eigenstate, while possible in numerics, is experimentally impossible as it would require performing highly nonlocal operations on the system. Further investigations, such as [89], have extended the study of the SPT-MBL phase to more practical settings for quantum manipulation, where for instance there may be a need to transport information in the protected edge qubits by shifting the SPT boundary.

3.7 Appendix A: Analysis of Spin Echo Protocol

In this section, we work through the effects of the spin echo protocol from Section 3.5 step-by-step to obtain the dependence of the final spin echo fidelity on various parameters.

Consider the time evolution of the system with Hamiltonian Eq. 3.8 as well as an edge field acting on the "bare" edge spin, $H(g) = H + g\Sigma_L^x = H + g\sigma_1^x\sigma_2^z$. In the initial state,

$$|\psi_0\rangle = |\uparrow\uparrow \dots \uparrow\rangle, \tag{3.13}$$

the bare edge spin points along $\Sigma_L^z = \sigma_1^z$. Our protocol is the following: we evolve under $H(g)$ for a time t_R, reverse the field $g \to -g$ by evolving under $H(-g)$ for an additional time t_R, and measure the value of the edge spin. The signature of the SPT-MBL phase is a non-vanishing overlap between the edge spin value at $t = 2t_R$ compared to $t = 0$, even when $t_R \to \infty$.

We will track the time evolution in the eigenbasis of the interacting Hamiltonian in weak edge field. Because of the integrability of the MBL phase, eigenstates can be labeled with quantum numbers of local operators. We write the zero-field interacting basis as $|\tilde{\sigma}, \tilde{\alpha}, 0\rangle$, which denotes a state with edge spin $\tilde{\Sigma}_L^x$ equal to $\tilde{\sigma} = \pm 1$ and bulk conserved operators $\tilde{K}_i$ equal to $\{\tilde{\kappa}_i^\alpha\}$. For brevity of notation we will sometimes combine the two labels $\tilde{\sigma}$ and $\tilde{\alpha}$ to a single label a. Our initial state can be expanded as

$$|\psi_0\rangle = \sum_{\tilde{\sigma}\tilde{\alpha}} \eta_{\tilde{\sigma}\tilde{\alpha}} |\tilde{\sigma}, \tilde{\alpha}, 0\rangle. \tag{3.14}$$

Crucially, the MBL eigenstates in weak edge field can be labeled with the quantum numbers of the zero-field states, e.g. $|\tilde{\sigma}, \tilde{\alpha}, g\rangle$ denotes the eigenstate at finite g continuously connected to $|\tilde{\sigma}, \tilde{\alpha}, 0\rangle$. This tracking is valid for g within the radius of convergence of perturbation theory, which is finite because MBL is stable to weak perturbations. In fact, g can even be of order one; because the perturbation $g\Sigma_L^x$ is localized, eigenstates with and without the field differ only within a distance roughly ξ of the edge and there is strong overlap between the states,

$$\langle a, g | a', 0\rangle = B_a(g, V, h)\delta_{aa'} + g\gamma_{aa'}(g, V, h)(1 - \delta_{aa'}), \tag{3.15}$$

where $B_a(g,V,h)$ has the form $(1-\mathcal{O}(g^2))e^{i\psi_a}$ and ψ_a starts at order g. Similarly,

$$\langle a,-g|a',g\rangle = C_a(g,V,h)\delta_{aa'} + g\chi_{aa'}(g,V,h)(1-\delta_{aa'}). \tag{3.16}$$

In time evolution ($U_g(t_R) \equiv e^{-iH(g)t_R}$) below, we keep only the components of the state which will contribute a coherent response,

$$|\psi_0\rangle = \sum_a \eta_a |a,0\rangle, \tag{3.17}$$

$$U_g(t_R)|\psi_0\rangle = \sum_a \eta_a B_a(g) e^{-iE_a(g)t_R}|a,g\rangle, \tag{3.18}$$

$$\begin{aligned} U_{-g}(t_R)U_g(t_R)|\psi_0\rangle &= \sum_a \eta_a B_a(g)C_a(g)e^{-i[E_a(g)+E_a(-g)]t_R}|a,-g\rangle \\ &= \sum_a \eta_a R_a(g) e^{-i[E_a(g)+E_a(-g)]t_R}|a,0\rangle, \end{aligned} \tag{3.19}$$

where $R_a(g) \equiv B_a(g)C_a(g)B_a(-g)^*$. In particular, we measure $\langle\psi(2t_R)|\Sigma_L^z|\psi(2t_R)\rangle$:

$$\begin{aligned} \langle\Sigma_L^z(2t_R)\rangle &= Z\langle\tilde{\Sigma}_L^z(2t_R)\rangle + ... \\ &= Z\sum_{\sigma,\alpha}\eta_{\sigma\alpha}\eta^*_{-\sigma\alpha}R_{\sigma\alpha}(g)R^*_{-\sigma\alpha}(g)e^{-i[E_{\sigma\alpha}(g)+E_{\sigma\alpha}(-g)]t_R}e^{+i[E_{-\sigma\alpha}(g)+E_{-\sigma\alpha}(-g)]t_R} + ... \end{aligned} \tag{3.20}$$

The energies for $\pm g$, with power expansion $E_{\sigma\alpha}(g) = E^0_\alpha + f_1(\tilde{\sigma},\tilde{\alpha})g + f_2(\tilde{\sigma},\tilde{\alpha})g^2 + ...$, can be related. The edge field weakly breaks the symmetry $S = \prod_i \sigma^x_{2i}$ which transforms $H(g) \to H(-g)$. Hence if $|\psi\rangle$ is an eigenstate of $H(g)$ with energy E, $S|\psi\rangle$ is an eigenstate of $H(-g)$ with the same energy. If $|\psi\rangle$ is labeled $|\sigma,\alpha,g\rangle$, $S|\psi\rangle$ has flipped $\tilde{\Sigma}^x_L$ spin quantum number since

$$S|\sigma,\alpha,g\rangle = e^{i\theta_a(g)}|-\sigma,\alpha,-g\rangle. \tag{3.21}$$

The energies of states with these quantum numbers are therefore degenerate:

$$E_{\sigma\alpha}(g) = E_{-\sigma\alpha}(-g). \tag{3.22}$$

Consequently, the even in g terms in the energy expansion are σ-independent while odd terms are not:

$$E_{\sigma\alpha}(g) = E^0_\alpha + f_1(\tilde{\alpha})\tilde{\sigma}g + f_2(\tilde{\alpha})g^2 + ... \tag{3.23}$$

As a result, the t_R-dependent phases accumulated in time evolution cancel:

$$\begin{aligned}\langle \Sigma_L^z(2t_R)\rangle &= Z\langle \tilde{\Sigma}_L^z(2t_R)\rangle + ... \\ &= Z\sum_{\sigma,\alpha}(\eta_{\sigma\alpha}\eta^*_{-\sigma\alpha})R_{\sigma\alpha}(g)R^*_{-\sigma\alpha}(g) + ...\end{aligned} \tag{3.24}$$

Note also that:

$$\begin{aligned}R_{\downarrow\alpha}(g) &= \langle\tilde{\downarrow}, 0|\tilde{\downarrow}, -g\rangle\langle\tilde{\downarrow}, -g|\tilde{\downarrow}, g\rangle\langle\tilde{\downarrow}, g|\tilde{\downarrow}, 0\rangle \\ &= \langle\tilde{\uparrow}, 0|\tilde{\uparrow}, g\rangle\langle\tilde{\uparrow}, g|\tilde{\uparrow}, -g\rangle\langle\tilde{\uparrow}, -g|\tilde{\uparrow}, 0\rangle \\ &= \Big(\langle\tilde{\uparrow}, 0|\tilde{\uparrow}, -g\rangle\langle\tilde{\uparrow}, -g|\tilde{\uparrow}, g\rangle\langle\tilde{\uparrow}, g|\tilde{\uparrow}, 0\rangle\Big)^* \\ &= R^*_{\uparrow,\alpha}(g) \equiv R^*_\alpha(g).\end{aligned} \tag{3.25}$$

Consequently, we obtain:

$$\langle \Sigma_L^z(2t_R)\rangle = Z\sum_\alpha 2\ \mathrm{Re}\left[\eta_{\uparrow\alpha}\eta^*_{\downarrow\alpha}R^2_\alpha(g)\right] + ... \tag{3.26}$$

Compare this to:

$$\begin{aligned}1 = \langle \Sigma_L^z(0)\rangle = Z\langle \tilde{\Sigma}_L^z(0)\rangle + ... = Z\sum_{\sigma,\alpha}\eta_{\sigma\alpha}\eta^*_{-\sigma\alpha} + ... \\ = Z\sum_\alpha 2\ \mathrm{Re}\left[\eta_{\uparrow\alpha}\eta^*_{\downarrow\alpha}\right] + ...\end{aligned} \tag{3.27}$$

We drop other terms ... in the series and the remaining is expected to be close to 1 for small h, V. Eq. 3.26 shows that after the protocol, we have accumulated additional overlap factors proportional to $R^2_\alpha(g)$. Crucially, these are also small, having the form $R_\alpha(g) \approx (1 - \mathcal{O}(g))$. Consequently, the final value of the edge spin is close to the initial value, with small corrections,

$$\begin{aligned}\langle \Sigma_L^z(2t_R)\rangle &= Z\sum_{\sigma,\alpha} 2\ \mathrm{Re}\left[\eta_{\uparrow\alpha}\eta^*_{\downarrow\alpha}\right] - \mathcal{O}(g) + ... \\ &= Z\langle \tilde{\Sigma}_L^z(0)\rangle - \mathcal{O}(g) + ...\end{aligned} \tag{3.28}$$

One of the key ingredients is that with finite g we work perturbatively close to the $g = 0$ interacting problem. In the latter case, we evolve with $H(g = 0)$ which treats $\uparrow, \downarrow$ edge spins on equal footing and results in a large response to the protocol. Turning on

a localized edge field for a general (thermal) phase would cause nonperturbative changes throughout the energy spectrum. Due to MBL, however, the changes in the case above are only perturbative at all energy densities. The response to the protocol is therefore only weakly modified despite the fact that we are dealing with dynamics and hence a large fraction of states of the spectrum. We expect a large response to the protocol studied above to be one probe of the presence of a MBL-SPT phase.

3.8 Appendix B: Additional Figures

This section contains additional figures and context referenced in the main text of this chapter.

Comparing Integrability and Non-Integrability: Figures 3.10 and 3.11 compare the evolution of the edge spin in the SPT-MBL phase in the noninteracting and fully interacting Hamiltonian. Numerics are for a single disorder realization on an open eight-site chain, with parameters set to be zero-mean Gaussians with $(\sigma_V, \sigma_\lambda, \sigma_h) = (0, 1, 0.15)$, $(0.1, 1, 0.05)$, respectively. The integrability puts a strong constraint on the finite-size interedge coupling terms which can appear in Eq. 3.11, so that Figure 3.10 displays oscillations with fewer frequencies than Figure 3.11. In either case, these terms lead to a dephasing of the edge spin on a system-size dependent time scale.

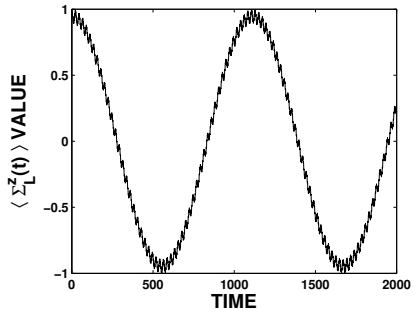

Figure 3.10

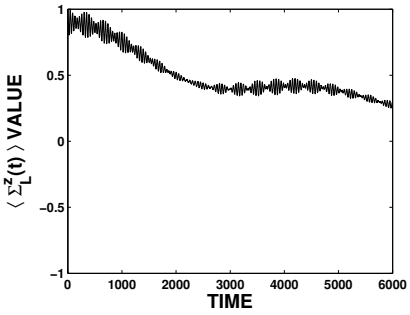

Figure 3.11

Extraction of T_0 time: For the numerics, we used exact diagonalization on the Hamiltonian Eq. 3.8 for an open chain with between six and eleven sites. Parameters followed a zero-mean Gaussian distribution with $(\sigma_V, \sigma_\lambda, \sigma_h) = (0.1, 1, 0.05)$. Disorder realizations were selected to have characteristics closely matching the mentioned parameters per sample (within 0.01 tolerance). We computed $\overline{\langle \Sigma^z_L(t) \rangle}$, averaging over disorder and the two sample edges to get smooth curves, and found it fit well to a stretched exponential $C_0 \exp(-\sqrt{t/T_0})$ at longer times (fits shown in Figure 3.12). We used, for $N = 6 - 11$, $\{8000, 2000, 6400, 1900, 235, 290\}$ disorder realizations, respectively.

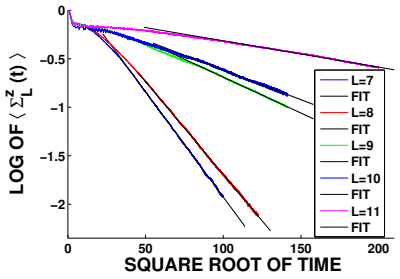

Figure 3.12

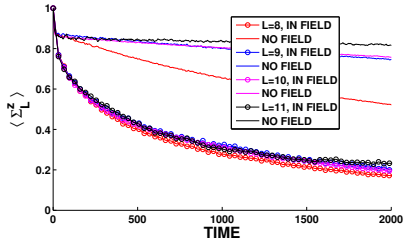

Figure 3.13

Extraction of T_2^* time: We considered the Hamiltonian $H_0 + g\Sigma_L^x$ with $g = 0.05$ for system sizes $N = 8 - 11$. We chose the value $g = 0.05$ because (i) for much smaller fields it is more difficult to separate the field-dependent time scale T_2^* from the size dependent T_2 for the system sizes we can access and (ii) much larger fields move the edge inwards and thus reduce the overlap between the local operators Σ_L^α and the true edge operators $\tilde{\Sigma}_L^\alpha$.

To obtain the time constant T_2^*, we first disorder average, $\overline{\langle \Sigma_L^z(t) \rangle}$, to obtain a smoothly oscillating curve. We found that the envelope of its decay fit well to a stretched exponential $\exp(-\sqrt{t/T_2^*})$ at early times. We extract from this a T_2^* decay time which does not scale exponentially with system size. In Figure 3.13 we plot both the envelope of the averaged oscillations as well as decay of the edge spin in zero-field (with characteristic time T_0) for comparison. Parameters followed a zero-mean Gaussian distribution with $(\sigma_V, \sigma_\lambda, \sigma_h) = (0.1, 1, 0.05)$.

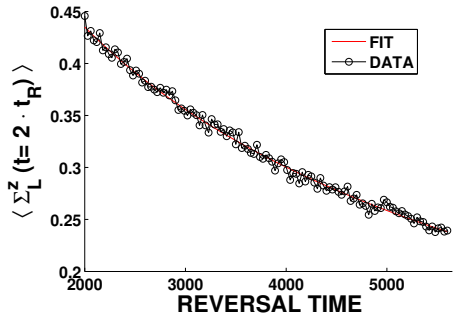

Figure 3.14

Extraction of T_2 time: We computed the disorder averaged fidelity $\overline{\langle \Sigma_L^z(2 \cdot T_R) \rangle}$ at the end of the spin echo protocol. Exact diagonalization on system with $N = 7 - 11$ was done with $\{8000, 5000, 5000, 2000, 3000\}$ samples (for the five system sizes, respectively), for intermediate values of the echo reversal time. The computations were done with an edge field value $g = 0.05$ and initial state polarized along σ^z. The data fit well to a stretched exponential of the form $\overline{\langle \Sigma_L^z(2 \cdot T_R) \rangle} \sim C_1 \exp(-\sqrt{T_R/T_2})$. Figure 3.14 shows an example of the disordered averaged spin echo fidelity decaying on the time scale T_2 for an open chain

with $N = 7$ sites. In this case, parameters followed a zero-mean normal distribution with $(\sigma_V, \sigma_\lambda, \sigma_h) = (0.1, 1, 0.05)$.

Chapter 4

Construction of a Stable Non-Fermi Liquid Phase

Fermi liquids are states with well-defined gapless fermion quasiparticles. The theory of Fermi liquids has formed the basis of our understanding of interacting quantum metals since its conception by Landau in the 1950's [90–92]. However, some interacting gapless systems, generically termed non-Fermi liquids (NFLs), cannot be described in this framework, and we do not yet have a cohesive understanding of them. A common route towards realizing an NFL is by strongly coupling a Fermi surface to gapless bosonic modes. These types of NFLs may ultimately be unstable at low energies, with a different kind of physics setting in. Our advance in this chapter is to construct an NFL out of rather ordinary ingredients and to demonstrate its stability within well-motivated field theoretic calculations. Its simplicity and stability set it apart as a candidate for experimental realization. Before commencing discussion of our work [93], we introduce some essential elements of Fermi liquid theory and give a brief survey of NFLs.

4.1 Fermi Liquids

Despite the existence of potentially strong interactions, many metals exhibit thermodynamic signatures or physical responses which bear some similarity to that of the free Fermi gas. This suggests that some concepts from the free theory may carry over to interacting metals. Indeed, a key part of Landau's insight in developing Fermi liquid theory was that the labels for the noninteracting problem [94, 95] could still remain valid with interactions, being robust as long as no phase transition occurs. Quantities like momentum $\vec{k}$ and spin σ could hence continue to be used to label states. This one-to-one correspondence between single-particle states of the Fermi gas and and their continuation to the Fermi liquid, which defines the quasiparticles, lies at the heart of Fermi liquid theory. In fact, as we will see, it only holds at sufficiently low energies. The quasiparticles are not the true eigenstates of the problem and have a finite lifetime τ which increases upon approaching the Fermi surface.

To motivate the physicality of quasiparticles states, consider a thought experiment, following the discussion given by Anderson [95], in which interactions are turned on slowly over a time R^{-1} starting from the Fermi gas. This rate R must be chosen in a manner consistent with some constraints. The time R^{-1} needs to be long enough to provide resolution over the excitation energies of interest, set by the temperature T, but short enough so that the quasiparticles, if they are indeed well-defined, have not decayed. This translates to the condition

$$\frac{\hbar}{k_B T} < R^{-1} < \tau. \tag{4.1}$$

The lifetime τ can be estimated using Fermi's Golden Rule. Let us look at a scattering process in which an electron with momentum $\vec{k}$ and excitation energy $\epsilon_{\vec{k}}$ above the Fermi surface transitions to a state with momentum $\vec{k}+\vec{q}$ while scattering another electron from $\vec{k}'$ to $\vec{k}'-\vec{q}$. The lifetime for the state $\vec{k}$ will be proportional to

$$\frac{1}{\tau} \sim \int d^3\vec{q} \int d^3\vec{k}' \, |V(\vec{q})|^2 \, \delta(\epsilon_{\vec{k}+\vec{q}} + \epsilon_{\vec{k}'-\vec{q}} - \epsilon_{\vec{k}'} - \epsilon_{\vec{k}}). \tag{4.2}$$

Crucially, the phase space available for this scattering process is strongly restricted, requiring one to simultaneously satisfy the Pauli exclusion principle, momentum, and energy conservation. Each of the two integrals will give a restriction proportional to $\epsilon_{\vec{k}}$ so that the final results scales as $\tau^{-1} \sim V^2 \epsilon_{\vec{k}}^2 / E_F^3$ [95]. The important result is the dependence of the lifetime on the excitation energy $\epsilon_{\vec{k}}$. Sufficiently close to the Fermi surface there is a separation of the two scales, since $k_B T \sim \epsilon_{\vec{k}} \gg \tau^{-1} \sim \epsilon_{\vec{k}}^2$, and a rate R can be chosen. Formally, the quasiparticle inverse lifetime is measured by the imaginary part of its self-energy, which is affected by various scattering processes with other quasiparticles or gapless modes. The scaling of this inverse lifetime relative to the energy $\epsilon_{\vec{k}}$ is the key indicator of Fermi or non-Fermi liquid behavior.

While the Fermi gas labeling of states continues to hold in the interacting Fermi liquid, other features may not translate directly. New features – such as new collective modes – may arise as well [94]. The total energy of the interacting system, which functionally depends on the quasiparticle distribution $\delta n_{\vec{k}\sigma}$, is given by

$$E = E_g + \sum_{\vec{k}\sigma} \delta n_{\vec{k}\sigma} \epsilon_{\vec{k}\sigma} + \frac{1}{2} \sum_{\vec{k}\vec{k}'\sigma\sigma'} f_{\vec{k}\sigma,\vec{k}'\sigma'} \delta n_{\vec{k}\sigma} \delta n_{\vec{k}'\sigma'}, \tag{4.3}$$

where for an isotropic system $\epsilon_{\vec{k}\sigma} = \frac{k_F}{m^*}(|\vec{k}| - k_F)$. This equation brings forth key parameters in Fermi liquid theory: m^* is the quasiparticle mass, possibly different from the bare electron mass, and the function $f_{\vec{k}\sigma,\vec{k}'\sigma'}$ parameterizes quasiparticle interactions. A computation of thermodynamic signatures reveals that many display the same temperature dependence

as the free Fermi gas (since these originate from sharply defined quasiparticles) but with modified coefficients [94], such as the specific heat and magnetic susceptibility

$$c_v = \frac{1}{3}\frac{m^* k_F}{\hbar^3} k_B^2 T, \qquad \chi = \frac{m^* k_F}{\pi^2 \hbar}\frac{\mu_B^2}{1+F_0^a}, \tag{4.4}$$

where F_0^a derives from the interaction function $f_{\vec{k}\sigma,\vec{k}'\sigma'}$.

How are the Landau quasiparticles related to more physical degrees of freedom we might have access to? A quasiparticle state with creation operator $Q^\dagger_{\vec{k}\sigma}$ will have an expansion in the bare electron states, with creation operators $c^\dagger_{\vec{k}\sigma}$, as

$$Q^\dagger_{\vec{k}\sigma}|0\rangle = \sqrt{Z_{\vec{k}}}\, c^\dagger_{\vec{k}\sigma}|0\rangle + \sum_{\alpha\beta\gamma} \Gamma_{\alpha\beta\gamma} c^\dagger_\alpha c^\dagger_\beta c_\gamma |0\rangle + ..., \tag{4.5}$$

where we have dropped higher-order electron-hole terms, and the summation is over all composite labels of the form $\alpha = (\vec{k}', \sigma')$ consistent with momentum and spin conservation to yield a resultant with momentum $\vec{k}$ and spin σ. $Z_{\vec{k}}$ is known as the quasiparticle residue and measures the overlap between quasiparticle and bare electron. The overlap is manifest, for instance, in the electron spectral function, which is no longer sharply peaked about a single momentum and energy as in the free Fermi gas [94]. Eq. 4.5 is very reminiscent of an expansion for many-body localized systems in Chapter 3, wherein the "p-bits" – the physical or bare operators – were expanded in terms of the "ℓ-bits" – the localized integrability operators which diagonalized the Hamiltonian. Although in the setting of this chapter the operators are not localized, both expansions, whether for Fermi liquid theory or many-body localization, illustrate and make precise the notion that we can view one set of operators and states as dressed versions of the other.

Fermi liquid theory can in fact be derived as a fixed point of a renormalization group (RG) procedure, where the effective mass and f function appear naturally [96–98]. RG for fermions at finite density differs from the conventional momentum approaches because, in the latter context, one is typically dealing with a bosonic order parameter and integrating out momentum shells towards a point or set of points rather than towards an extended manifold.[1] The RG identifies superconductivity (of BCS type) as an instability of the Fermi surface: a weak but attractive interaction in any angular momentum channel leads to a flow away from the Fermi liquid fixed point. This is the only relevant weak-coupling instability in two and three dimensions.

Fermi liquid theory has held up remarkably well against a tremendous body of experimental investigations. It can provide an accurate description even for strongly interacting metals, such as the heavy fermion UPt_3, where tightly bound f electrons can mix with conduction electrons to form heavy quasiparticles [94]. We turn our attention now to less understood gapless phases which lie outside this framework.

[1] This difference between RG for bosons and fermions with a Fermi surface is an important consideration in devising RG procedures for systems where the two are coupled, as we will see.

4.2 Non-Fermi Liquids

"Non-Fermi liquids" is a general name given to gapless fermion systems that do not have well-defined quasiparticles. This terminology is rather all-encompassing, and we will discuss several examples which illustrate how disparate their origins can be.

Spatial dimensionality can impose phase space constraints which lead to NFL behavior. Luttinger liquid theory is the correct low-energy description for 1D metals, applicable to quantum wires and the chiral edge states in the quantum Hall effect, for instance. One dimension is special in that the Fermi surface consists of only two points. It turns out that the correct low-energy modes of such a system are bosonic, rather than the usual fermion quasiparticles, and consist of of charge and spin-density waves.

Other NFLs can be *local*. A well-known example [99] is the family of generalized Kondo problems: couple a spin-1/2 magnetic impurity to one or more baths of conduction electrons. The single-channel Kondo problem – in which there is one conducting bath – is known to be a Fermi liquid at temperatures far below the Kondo temperature. The impurity is rather inert after forming the Kondo singlet. In contrast, the two-channel Kondo problem, where the impurity couples to two independent baths, results in an NFL at low energies. In that case, theoretical analysis reveals an interesting feature in the impurity spin entropy: it behaves as if there is a fractional degree of freedom remaining, saturating at $\ln \sqrt{2}$ at low energies rather than vanishing. This constitutes an example of a local NFL since the low-energy bulk behavior is modified near the site of the impurity and not the bulk. As a whole, the family of generalized Kondo models provides an interesting source of theoretically well-studied, and sometimes experimentally realizable, NFLs [94, 99].

A third and quite important class of NFLs originates from coupling a Fermi surface to gapless bosonic modes. A common source is the amplitude fluctuations of a quantum critical point. NFLs arising from proximity to a quantum critical point have been studied in a variety of settings, including in magnetic, nematic, and charge density-wave transitions. They may also bear important clues as to the nature of high-temperature superconductivity. Alternatively, coupling to gauge bosons also typically gives rise to an NFL. This bears relevance for quantum spin liquids where emergent gauge fields can couple to a Fermi surface of fractional spinon or composite fermion excitations [100–103].

It is noteworthy that the very same bosons that strongly couple to the Fermi surface mediate interactions between (incoherent) fermions which could lead to an altogether different low-energy state. In many of the relevant examples of NFLs obtained from quantum criticality, the system is unstable to some form of boson-mediated ordering. Our proposal [93] for an NFL does not appear to be plagued by an instability, at least within the applicability of our calculations. The ultimate fate of the NFL is a difficult question to settle theoretically, and we will describe some recent novel RG approaches for these strongly coupled systems.

Goldstone modes are another source of gapless bosonic modes. One setting of this kind that does give rise to an NFL is the Goldstone mode of an electronic nematic, a Fermi surface with spontaneously broken continuous rotational symmetry [104]. To leading order in perturbation theory, it was shown [104] that the imaginary part of the electron self-energy

acquires a correction Im $\Sigma(\omega) \sim |\omega|^{\frac{2}{3}}$ at nearly all points on the Fermi surface apart from a few special symmetry directions. The usual mechanistic understanding of how this comes about – Landau damping of the bosonic mode giving rise to corrections in the electron self-energy – will be discussed in the context of our work [93] in Section 4.4. The perturbative calculation of [104] accurately signals the breakdown of Fermi liquid theory but cannot capture the ultimate fate of the system at low energies.

Besides the nematic metal, it remained unclear whether Goldstone modes arising from other kinds of spontaneous symmetry breaking could also couple strongly to the Fermi surface, resulting in an NFL. [105] was able to provide a general criterion to resolve such cases. Couplings which lead to an NFL must necessarily be non-derivative couplings, ones that remain finite even in the limit of zero momentum transfer. This can be translated to a statement about the broken symmetry: strong coupling results when the broken symmetry generator, Q_a, of the continuous symmetry fails to commute with any of the conserved momenta P_i, $[Q_a, P_i] \neq 0$. The NFL arising in the electronic nematic satisfies this since the symmetry generators are angular momentum operators, which do not commute with momentum. The generality of the criterion also enabled [105] to identify a previously unknown setting, spontaoneous breaking of magnetic translation symmetry, as giving rise to an NFL. In contrast, phonons – the Goldstone bosons of broken translation symmetry – result in weak coupling and leave the Fermi liquid intact.

Analytic Techniques for a Strongly Coupled Fermi Surface and Gapless Bosons

Devising a correct effective field theory is often tractable when degrees of freedom are weakly coupled. However, describing the low-energy behavior of a system with strongly coupling is generally quite difficult. Progress on this question on the theoretical front would be important for capturing the ultimate fate of an NFL originating from a Fermi surface coupled to gapless bosons.

Hertz theory [106] constitutes one of the earliest treatments of the Fermi surface and boson system, but its technical correctness is questionable. Hertz argued for deriving an effective theory for the bosons by integrating out the fermionic modes entirely. The effective boson action is, in principle, an infinite series of all orders in the boson field, where Landau damping can be observed explicitly in the quadratic terms. To be amenable for analysis, however, series truncation is required. This step can typically invalidate Hertz theory though: integrating out gapless fermions produces singularities which affect the coefficients in the infinite series, as was demonstrated in [107, 108].

In fact, these issues were analyzed closely by [108], building on earlier work [109–112] suggesting the problem could simplify under a particular decoupling. [108] confirmed that the leading singularities plaguing Hertz theory appear only for terms where the momenta of the bosonic fields are nearly collinear. Effectively, bosons with noncollinear momenta decouple from one another. Moreover, bosons with collinear momenta couple most strongly

to regions of the Fermi surface where their momentum is tangent. This suggests that an effective description of a strongly coupled Fermi surface-boson system at low energies would involve decoupled patches. In 2D for a single Fermi surface, a good theory might be written in terms of a collection of pairs of antipodal patches, each pair treated independently and coupled to bosonic modes with tangent momenta. A pair of patches would constitute a (2+1)D field theory; while this makes the description redundant, it can be accounted for when sewing the patches together. Nonetheless, a large N expansion was used in some of these approaches and subsequent higher loop calculations [112, 108] suggested the use of large N alone could not provide adequate control over the expansion.

Instead, it was found [113] that a dual expansion in parameters N and ϵ could be used to control the series in the limit $N \to \infty, \epsilon \to 0$ in a way so as to keep ϵN finite. N refers to the number of fermion flavors that may be artificially introduced, and ϵ is related to the boson dynamic critical exponent z_b as $\epsilon = z_b - 2$. A dynamic exponent in principle can be renormalized; using it as an expansion parameter is most useful when renormalization is not expected, for instance when the exponent controls a nonlocal term in the Lagrangian, since integrating out only high frequency shells will not contribute any of the needed singularities. [113] also found that many random phase approximation (RPA) results can be used, with possible deviations appearing at higher order in the expansion, so that the one-loop corrections to the boson propagator and electron self-energy which give the NFL are essentially correct. The physics in the patch theory appears governed by a scale-invariant fixed point with scaling transformations

$$\begin{aligned} \omega' &= \omega b^{z_b/2}, \\ k'_\perp &= k_\perp b, \\ k'_\parallel &= k_\parallel \sqrt{b}, \end{aligned} \qquad \begin{aligned} \psi'(\boldsymbol{k}', \omega') &= b^{-(z_b+5)/4} \psi(\boldsymbol{k}, \omega), \\ \phi'(\boldsymbol{k}', \omega') &= b^{-(1+z_b)/2} \phi(\boldsymbol{k}, \omega), \end{aligned} \tag{4.6}$$

for the patch variables: frequency ω, momentum parallel $k_\parallel$ and perpendicular $k_\perp$ to the Fermi surface, and fermion and bosons fields, ψ and ϕ.

These transformations can be used to follow how correlation functions and susceptibilities in particular channels behave and whether any singularities, which would suggest a propensity towards order, would appear. [113] used these to characterize both (i) the Fermi surface coupled to a gauge field as well as (ii) quantum critical metals near a nematic transition. Which susceptibilities are enhanced or suppressed by the presence of the boson depends in large part on how the boson couples to two antipodal Fermi surface patches in a pair. In the gauge field case, the coupling mediates an attractive interaction between particle and hole (thereby enhancing the susceptibility in this channel) and a repulsive interaction between particles (suppressing the Cooper channel susceptibility). For the nematic problem, the two cases are reversed, so that there is a stronger response to Cooper pairing. In our treatment of an NFL [93], we rely heavily on the combined (N, ϵ) expansion [113] – in particular, the scaling transformations in Eq. 4.6 above – to calculate susceptibilities.

Nonetheless, there are settings for which the decoupled patch description is insufficient. In particular, this is the case for the Fermi surface near a nematic quantum phase transition, considered in [113]. A single scattering event between two particles in the Cooper pair channel keeps the pair near the Fermi surface – they are perfectly nested – while this is not the case for particle-hole scattering. Quantitatively, this translates to the observation that an RG procedure which integrates out boson momentum and fermion momentum parallel to the Fermi surface generates relevant inter-patch interactions [114, 115]. This motivated [115] to lay the foundation for a simultaneous boson and Fermi surface RG procedure, building on a treatment in [114] used to analyze color superconductivity in non-Abelian gauge theory. In the multi-patch RG, patches are no longer decoupled. In addition to the parameters of the decoupled two-patch theory, here one must keep track of inter-patch interactions as momentum parallel to the Fermi surface is eliminated. [115] found that, within the regime where the RG calculation is controlled, the NFL obtained at the nematic critical point is unstable to superconductivity and furthermore, that it sets in at an energy scale higher than the onset of the NFL. This could mean that the NFL is obscured by subsidiary order and might be experimentally unobservable. It is therefore important to identify a setting in which an NFL, obtained in this manner by coupling a Fermi surface to bosons, remains intact, at the very least within an experimentally accessible window.

4.3 Coupling a Spin-Orbit Fermi Surface to Fluctuating Magnetization

The remainder of this chapter discusses our contribution [93] to these topics. The setting is that of itinerant ferromagnets with (i) broken continuous rotation symmetry and (ii) spin-orbit coupling (SOC). We bring together these ingredients to realize an NFL and then demonstrate, using presently available state of the art field theoretic methods, the stability of the NFL to boson-mediated ordering. This represents one of our key findings and is to be contrasted with instabilities in many other NFLs, in particular the one arising in the electronic nematic studied by [115].

The origin of NFL behavior is such systems can be understood qualitatively by comparison to ordinary ferromagnets (Figure 4.1). In the latter case, ferromagnetic order splits the initially spin degenerate Fermi surface into two spin-polarized Fermi surfaces with a gap Δ. Fluctuations of the order parameter can create electronic spin-flip excitations only by supplying either nonzero energy or momentum. Hence, there are no accessible spin-carrying electron-hole excitations at small energies and wavevectors, and in this region the ferromagnetic spin-waves effectively decouple from the electronic particle-hole continuum and exist as sharp, undamped excitations. This dynamical decoupling of low-energy order parameter fluctuations is typical of most Goldstone modes of a broken continuous symmetry [105]. By contrast, with SOC the electron spins are tied to momentum and are not fully polarized by the ferromagnetic order. Spin-flip excitations can be made at arbitrarily low energy

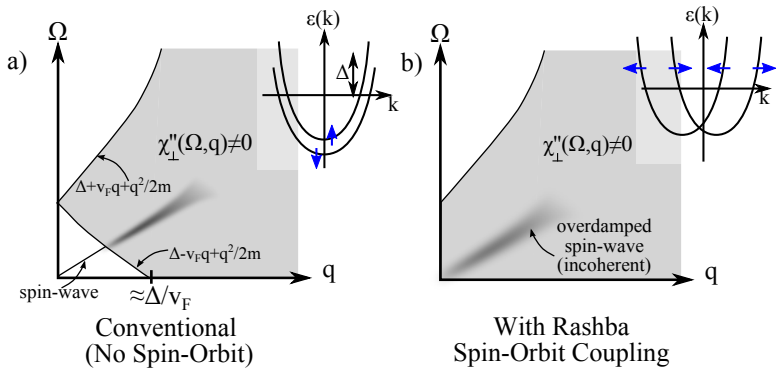

Figure 4.1: Spin excitations with and without Rashba spin-orbit coupling. (a) The imaginary part of the transverse spin susceptibility χ'' of a conventional ferromagnet (dispersion shown as an inset) has a gap at small frequency, Ω, and wavevector, q, in which a sharp spin-wave excitation can exist. In contrast, the Rashba spin-orbit coupled ferromagnet (b) has finite χ'' for small (Ω, q), leaving only an overdamped spin-wave that is strongly coupled to the electrons, resulting in NFL behavior.

and momenta over nearly the entire Fermi surface. To propagate, spin-waves must excite particle-hole pairs but will be overdamped by them, attaining a modified dispersion, $\Omega \sim q^3$, as we will illustrate diagrammatically. A boson with softer dynamics scatters electronic quasiparticles more strongly, and the effect will be to destroy the Landau quasiparticles near the Fermi surface.

We finally provide the specifics of the setting. Our system of spin-orbit coupled electrons is described by an imaginary time Lagrangian density $\mathcal{L} = \psi^\dagger \left[\partial_\tau + \mathcal{H}\right] \psi$ that is invariant under combined spatial and spin rotations about $\hat{\boldsymbol{z}}$. In this paper, we focus on 2D electron liquids with Rashba SOC,

$$\mathcal{H}_{\rm R} = \frac{k^2}{2m_0} - \mu + \alpha_R \hat{\boldsymbol{z}} \cdot (\mathbf{k} \times \boldsymbol{\sigma}). \tag{4.7}$$

We will also present calculations for the closely related topological insulator (TI) surface state with Hamiltonian

$$\mathcal{H}_{\rm TI} = v_D \hat{\boldsymbol{z}} \cdot (\vec{\boldsymbol{k}} \times \vec{\boldsymbol{\sigma}}) - \mu. \tag{4.8}$$

Suppose the system has spontaneous magnetization $\mathbf{M}$ with an easy-plane (XY) anisotropy. The long wavelength dynamics of the magnetization alone is given by the Lagrangian density

$$\mathcal{L}_M^0 = |\partial_\tau \mathbf{M}|^2 + c^2 |\nabla \mathbf{M}|^2, \tag{4.9}$$

while the spin-spin coupling of the magnetization to electrons is written as

$$H_{e-M} = -\lambda_0 \mathbf{M} \cdot \psi^\dagger \boldsymbol{\sigma} \psi. \tag{4.10}$$

The XY magnetization could, for instance, originate from the polarization of local moments, due to magnetic doping or proximity to a ferromagnetic insulator. Alternatively, it could originate from the ferromagnetism of the electrons themselves, a leading candidate ground state at low densities because of the enhanced density of states [116, 117]. Because of this propensity towards ferromagnetism, we are chiefly interested in this low-density regime of the Rashba bands, where the nonmagnetic Fermi surface has annular topology. However, we also present a complete set of calculations for the high-density regime of the Rashba bands, where there is a simply connected Fermi sea consisting of two concentric sheets.

In a regime well below the magnetic ordering temperature T_M, only fluctuations in the direction, not the amplitude, of $\mathbf{M}$ are important. These can be parameterized by a Goldstone (magnon) field $\phi(\mathbf{r}, t)$ as follows,

$$\mathbf{M}(\mathbf{r}, t) = M_0 \left[\hat{\boldsymbol{e}}_{\boldsymbol{M}} \cos\phi + (\hat{\boldsymbol{z}} \times \hat{\boldsymbol{e}}_{\boldsymbol{M}}) \sin\phi \right] \approx M_0 \left[\hat{\boldsymbol{e}}_{\boldsymbol{M}} + (\hat{\boldsymbol{z}} \times \hat{\boldsymbol{e}}_{\boldsymbol{M}}) \phi \right], \tag{4.11}$$

where the fluctuations have been linearized about the ordering direction.[2] We hereafter absorb a factor of M_0 into the magnon field, redefining $M_0 \phi \to \phi$.

Because of the SOC, the magnons are strongly coupled to low-energy electrons. We will utilize the decoupled patch theory following [113] and earlier work [108–112]. The electron-magnon interaction, Eq. 4.10, can be conveniently treated by dividing the Fermi surface into patches of small but nonzero extent tangent to the Fermi surface. Magnons with wavevector $\mathbf{q}$ couple most strongly to patches of the Fermi surface for which $\mathbf{q}$ is tangent. We therefore decompose the full Hamiltonian into independent sets of collinear patches. For the TI surface, the Fermi surface decouples into pairs of antipodal patches except precisely at the Dirac point. For the 2D Rashba liquid, the Fermi surface generically has quartets of collinear patches as shown in Figure 4.2.

In imaginary time, the uncorrected linearized Lagrangian density decomposed into patches indexed by j is

$$\begin{aligned} \mathcal{L}_{\text{patch}} = \sum_j \psi^\dagger_{j,\omega,\mathbf{k}} \Big(-i\omega + v_j k_\perp + \frac{k_{||}^2}{2m_j} \Big) \psi_{j,\omega,\mathbf{k}} \cdots \\ + \Big(\omega^2 + c^2 k^2 \Big) |\phi_{\omega,\mathbf{k}}|^2 + \sum_{j,\Omega,\mathbf{q}} \lambda(\hat{\boldsymbol{n}}_{\boldsymbol{j}}) \phi_{\Omega,\mathbf{q}} \psi^\dagger_{j,\omega+\Omega,\mathbf{k}+\mathbf{q}} \psi_{j,\omega,\mathbf{k}}, \end{aligned} \tag{4.12}$$

where $\hat{\boldsymbol{n}}_{\boldsymbol{j}}$ is a unit vector in the direction of patch j and $k_\perp, k_\parallel$ are coordinates perpendicular, parallel to the Fermi surface and fixed for a set of collinear patches. For the 2D Rashba liquid,

$$\lambda(\hat{\boldsymbol{n}}_{\boldsymbol{j}}) = \pm \lambda_0 (\hat{\boldsymbol{e}}_{\boldsymbol{M}} \cdot \hat{\boldsymbol{n}}_{\boldsymbol{j}}) X_j$$

[2] Quadratic contributions [108, 113] (analogous to diamagnetic terms for the problem of a Fermi surface coupled to a gauge field) are automatically incorporated by a proper choice of order of integration.

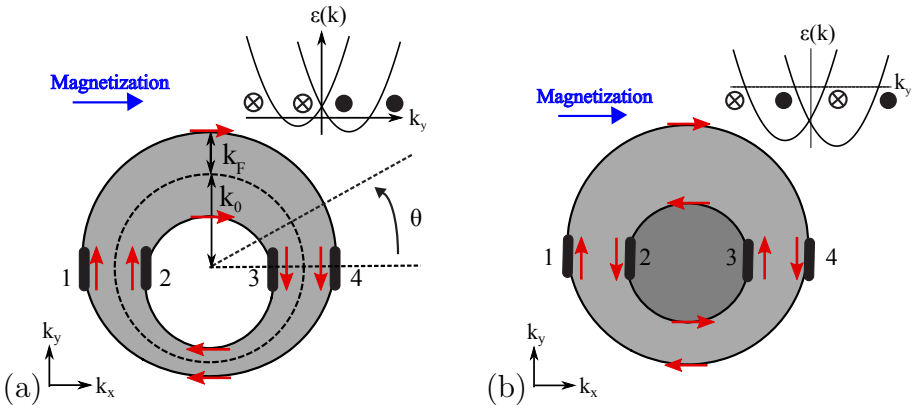

Figure 4.2: Fermi surfaces with magnetization. (a) Annular Fermi surface, obtained in the lower doping regime. Clockwise winding arrows denote electron spin orientation, which is the same on both surfaces. A representative set of collinear patches 1 – 4 is shown at special angle $\theta = 0$ (θ measured from the x axis), where the coupling to the Goldstone mode is strongest. The dashed circle is of radius k_0, while the annulus half width is $k_F(\theta)$. In this case, the Fermi momenta are $k_F^{>,<} \equiv k_0 \pm k_F(\theta)$. A cross section of the band dispersions at angle $\theta = \pi/2, 3\pi/2$ is shown, with the directions of the electron spin pointing into (cross) or out (black) of the page. The horizontal line is the Fermi level. (b) Similar diagram for the concentric Fermi surface regime, obtained at higher doping. Note that inner, outer Fermi surfaces have opposite windings of the electron spin. The Fermi momenta are $k_F^{>,<} \equiv k_F(\theta) \pm k_0$.

$$X_j \equiv \frac{\alpha_R k_{F,j}}{\sqrt{\left(\alpha_R k_{F,j}\hat{z}\cdot(\hat{\boldsymbol{e}}_{\boldsymbol{M}}\times\hat{\boldsymbol{n}}_{\boldsymbol{j}})+\lambda_0 M_0\right)^2+\left(\alpha_R k_{F,j}\hat{\boldsymbol{e}}_{\boldsymbol{M}}\cdot\hat{\boldsymbol{n}}_{\boldsymbol{j}}\right)^2}} \leq 1 \tag{4.13}$$

where $k_{F,j}$ is the Fermi momentum of the j^{th} patch, and $+(-)$ is for the lower (upper) Rashba bands. For the TI, $\lambda(\hat{\boldsymbol{n}}_{\boldsymbol{j}}) = \mp\lambda_0 \hat{\boldsymbol{e}}_{\boldsymbol{M}}\cdot\hat{\boldsymbol{n}}_{\boldsymbol{j}}$ for the electron $(-)$ or hole $(+)$ doped Fermi surfaces. When the spin-orbit coupling is strong, $\lambda_0 M_0 \ll \alpha_R k_{F,j}$, the Rashba and TI couplings are approximately the same, but for weak spin-orbit coupling $\lambda_0 M_0 \gg \alpha_R k_{F,j}$, the Rashba coupling is suppressed by a factor of $X_j \lesssim \frac{\alpha_R k_{F,j}}{\lambda_0 M_0}$ compared to the TI case.

Our calculations rely on the dual (N, ϵ) expansion proposed in [113]. All calculations are discussed in the appendices, Sections 4.8 – 4.10, and in the following primary sections we focus on a description of the results. In Section 4.4, we discuss the mechanics behind the NFL in SOC itinerant ferromagnets. While the existence of NFL phases in SOC ferromagnets was pointed out earlier in [118], our work focuses on Rashba systems and, crucially, investigates the issue of stability to subsidiary order, covered in Section 4.5. We also give an extensive discussion of experimental phenomenology and candidate materials in Section 4.6.

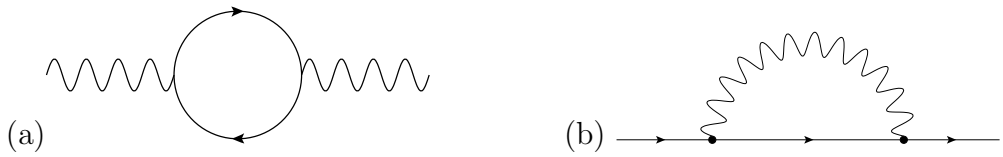

Figure 4.3: One-loop diagrams. (a) Boson polarization. (b) Fermion self-energy.

4.4 Landau Damping and the Breakdown of Electron Quasiparticles

We turn to the effect of the Goldstone modes and the electron quasiparticles on each other. This is often understood by first computing the one-loop correction to the boson propagator, which reveals the overdamping of the boson, termed *Landau damping*, and the resultant soft dispersion. In turn, this is fed back into a one-loop computation of the electron self-energy; with a softer boson dispersion, quasiparticles near the Fermi surface are scattered more strongly. The feedback effect of these fluctuations can essentially be treated in the RPA because deviations from this appear at higher order in the (N, ϵ) expansion.[3]

The calculations layed out in Section 4.8 result in a modified spin-wave propagator with the characteristic Landau damped form

$$D(\Omega, \mathbf{q}) \approx \left[\gamma(\hat{\boldsymbol{q}})\frac{|\Omega|}{|q_{\|}|} + c^2 q^2\right]^{-1}, \tag{4.14}$$

which is valid when $v_F q \gg \Omega$. We have dropped the bare Ω^2 term, since at energies below $E_{\mathrm{LD}} \approx \sqrt{\gamma(\hat{\boldsymbol{q}})v_F}$, the Landau damping term dominates the dynamics of the order parameter fluctuations, leading to overdamped spin-waves with dynamic exponent $z_b = 3$ ($\Omega \sim q^3$). The damping coefficient γ depends on the coupling of a collinear set of patches at angle θ to the Goldstone mode as $\gamma \sim \lambda(\hat{\boldsymbol{n}}_{\boldsymbol{j}})^2$, which for the case of strong spin-orbit coupling yields

$$\gamma(\theta) \approx \sum_j \lambda_0^2 \cos^2\theta \frac{|m_j|}{4\pi|v_j|}. \tag{4.15}$$

Here, θ is the patch angle on the Fermi surface as in Figure 4.2. The Landau damping parameter γ is nonzero over most of the Fermi surface except for special isolated points where the local patch spin is parallel to the ordered magnetization and couples only at quadratic order to the fluctuations. The spin-waves are maximally coupled to patches whose normals lie parallel or anti-parallel to the magnetic ordering direction (corresponding to $\theta = 0$).

[3]Typically, RPA treatments are justified by a large N expansion; however, as discussed in Section 4.2, the large N expansion is known to break down [112]. The use of RPA is formally justified by the double expansion [113] and also by uncontrolled higher loop calculations [108] which show that $z_b = 3$ RPA scaling is valid through three-loop order.

The overdamped fluctuations scatter electrons at energy ω from the Fermi surface with rate $\Gamma \approx |\omega|^{2/3}$ (Section 4.8) corresponding to a fermion self-energy [109, 110, 119, 120]

$$\Sigma_{f,j}(\omega) \approx i \, \mathrm{sgn}(\omega) E_{\mathrm{NFL,j}}^{1/3} |\omega|^{2/3}. \tag{4.16}$$

This is the key signature of the breakdown of the Fermi liquid. Sharp, long-lived Landau quasiparticles require $\lim_{\omega \to 0} \Gamma(\omega)/\omega \to 0$, as described in Section 4.1. In contrast, here the lifetime of electronic excitations becomes much shorter than their inverse frequency. We find that the NFL behavior takes over at energies below the characteristic scale

$$E_{\mathrm{NFL,j}} \approx \frac{\lambda(\hat{\boldsymbol{n}}_{\boldsymbol{j}})^6}{v_j^3 \gamma(\theta) c^4} \sim \frac{\lambda_0^4 \cos^4\theta}{k_0^2 c^4} \frac{m_0}{x(1 + x + |1 - x|)}, \tag{4.17}$$

where $x \equiv k_F/k_0 \approx \sqrt{\mu}$. At high dopings, E_{NFL} vanishes as μ^{-1}. In contrast, the Landau damping scale $E_{\mathrm{LD}} \sim \lambda_0 \sqrt{\frac{m_0}{x}} (x + 1 + |x - 1|)^{\frac{1}{2}}$ (considering the patches at $\theta = 0$) and hence approaches a constant at high doping.

The effects of nonzero temperature might be concerning: it is well known that the long-range magnetic order in two dimensions present at zero temperature washes out and becomes quasi-long-range order with algebraically decaying correlations of the order parameter, $\langle \mathbf{M}(r) \cdot \mathbf{M}(0) \rangle = M_0^2 r^{-T/(2\pi M_0^2 c^2)}$, characterized by exponent $\nu \approx T/T_M$ at temperature T. We see that the correlation length for the order parameter, $\xi_M(T) \approx e^{\kappa M_0^2 c^2/T}$, diverges exponentially as $T \to 0$. In contrast, the inelastic mean free path for electrons due to magnon scattering, $\ell_{NFL}(T) \approx T^{-2/3}$, diverges only algebraically as $T \to 0$. Hence, for temperatures well below $T_M \approx M_0^2 c^2$, we have $\xi_M \gg \ell_{NFL}$, and the NFL physics occurs on much shorter length scales than the algebraic decay of the order parameter. Our treatment is therefore largely valid despite the thermal suppression of long-range magnetic order.

The discussion on Landau damping and NFL behavior has thus far has centered on a Fermi surface with a finite density of carriers. This holds everywhere for the Rashba liquid; while there is a fine-tuned Dirac point between the annular and concentric Fermi surface regimes, it is accompanied by a large Fermi surface that leads to Landau damping and $z_b = 3$ scaling. However, tuning to the Dirac point for the TI surface does result in a vanishing density of carriers. The magnetic fluctuations couple to the Dirac point like a single vector component of a fluctuating $U(1)$ gauge field, and an emergent Lorentz symmetry dictates a low energy phase analogous to QED-3. The spin-waves are *critically* damped by the Dirac fermions (see [100]) and retain their relativistic dispersion, so that they have dynamic exponent $z_b = 1$ rather than $z_b = 3$.

4.5 Stability of the Non-Fermi Liquid Phase to Order

The NFL we have constructed from strong coupling between spin-waves and a spin-orbit coupled Fermi surface bears a number of similarities to the nematic NFL of [104]. The

subsequent analysis of [115] suggests that such a Fermi surface coupled to gapless nematic fluctuations is strongly unstable to superconductivity. The ultimate question for our non-Fermi liquid system is whether it too will be unstable to subsidiary order.

In the nematic metal, superconductivity arose because the overdamped nematic Goldstone modes mediate strong attraction between electrons on opposite sides of the Fermi surface, forming the "glue" for Cooper pairs. For the Rashba liquid, the ferromagnetic Goldstone mode mediates attractive (repulsive) interactions for fermions with the same (opposite) spin. Nonetheless, despite the mediation of attractive interactions, BCS-type superconductivity does not occur in the SOC ferromagnetic metal discussed here for two reasons: (i) the interaction between opposite sides of the Fermi surface is repulsive, and (ii) the magnetically ordered phase breaks time-reversal symmetry, energetically penalizing Cooper pairs with zero center-of-mass momentum. Spin-triplet Cooper pairing with finite center-of-mass momentum could be favored by the overdamped Goldstone modes. Ordering in a particle-hole channel, for example spin density wave (SDW) order with wavevector $2k_F^>$ or $2k_F^<$ due to boson-mediated repulsive interactions, is also a possibility.

Any such nonzero wavevector ordering, such as spin or pair density wave, would ultimately be fatal to the NFL phase because in the presence of translation symmetry-breaking order, the rotational Goldstone modes are not independent of translational Goldstone modes. The latter couple only weakly to the Fermi surface [105], resulting in ordinary Fermi liquid behavior even if the resulting phonons have soft nonrelativistic dispersions (as is the case for uniaxial density waves). Hence, whether the overdamped spin-wave interactions necessarily facilitate instability to translation symmetry-breaking order is a crucial issue for the stability of the NFL phase.

In this section, we will outline the results of calculations for the susceptibilities to finite momentum pairing and spin density wave orders. The calculations are in Section 4.9 and closely follow those of the $2k_F$ susceptibilites in [113]. However, we need to account for the presence of the multiple Fermi surfaces of the SOC metal.

A crucial issue is to justify the use of the decoupled patch theories in our case. As we saw, for the nematic metal, superconductivity arises from nested scattering of Cooper pairs with zero center-of-mass momentum between different patches. Hence, the superconducting instability is a property of the full Fermi surface and cannot be reliably obtained within a theory of decoupled patches. It requires the interpatch treatment developed in [115].

In stark contrast, in the ferromagnetic NFL scenario we are considering, the potential instabilities all have large nonzero wavevectors. The nonzero wavevector orders connect particle-particle or particle-hole pairs near the Fermi surface only in the vicinity of collinear patches lying along the ordering wavevector. For example, in the case of Cooper pairing with center-of-mass momentum $Q = k_F^> + k_F^<$, Cooper pairs with a particle each in patches 1 and 2 (Figure 4.2) have low energy but cannot remain close to the Fermi surface when scattered to other patches. Hence, the susceptibility to finite momentum order is a property of the patches connected by Q, not the full Fermi surface, and can be computed directly within the patch theory. We will see that while the susceptibilities to finite momentum pairing and SDW orders are enhanced compared to a Fermi liquid, they remain finite. In essence,

due to the breaking of time-reversal and inversion symmetries, we find that the overdamped spin-wave fluctuations lead to a mild enhancement of finite momentum susceptibilities but do not drive an instability towards order. As a corollary of our calculations for the Rashba liquid, the magnetic NFL phase of a TI surface metal is also stable against ordering, as in this context the only potential instability is towards SDW order.

Susceptibilities Within a Dual (N, ϵ) Expansion

We outline the calculations of Section 4.9. In the (N, ϵ) approach, the problem is generalized to have N flavors of fermions and modified bosonic kinetic energy $|q|^{1+\epsilon}|\phi_{\omega,\boldsymbol{q}}|^2$ (instead of the physical $q^2|\phi_{\omega,\boldsymbol{q}}|^2$ of Eq. 4.12). The expansion is justified in the joint limit of large N and small ϵ while maintaining the product $N\epsilon \sim \mathcal{O}(1)$. As a cautionary note, obtaining results for the physically relevant values $N, \epsilon = 1$ requires extrapolation beyond the safely controlled regime, as is typical for such asymptotic expansions. However, in lieu of further theoretical developments, the (N, ϵ) expansion is essentially the current state of the art.

Another potentially promising alternative is the recently developed codimension expansion [121, 122]. Despite some potential advantages, the codimension expansion clearly overestimates the stability of a Fermi surface to superconducting order (for familiar Fermi liquid interactions, the expansion suppresses the well-known BCS instability towards superconductivity). For this reason we believe the (N, ϵ) expansion better suited for our analysis of stability. Given the complexity of this strongly coupled problem, experiments which can test the validity of various theoretical approaches are highly desirable.

We evaluate the system's response to a test field of strength u_a that couples to an order parameter $\mathcal{O}_a(\boldsymbol{x}, \tau)$ in channel a. For instance, for $a = 2k_F^>$ SDW, a term $S_{\text{ext}} = \int d^2x d\tau \left[u_{2k_F^>} \psi_1^\dagger \psi_4(\boldsymbol{x}, \tau) + h.c. \right]$ would be added to the action. We are interested in the scaling form of two-point correlations of these order parameters. This can be deduced from the scaling dimension of the test field $u_a' = b^{\phi_{u_a}} u_a$, for which we compute the leading correction in ϵ (or equivalently, N^{-1}) in Section 4.9. Defining χ_a as the Fourier transform of the two-point correlation of $\mathcal{O}_a$, namely $\langle \mathcal{O}_a^*(x_\perp, x_{||}, \tau)\mathcal{O}_a(0,0,0)\rangle$, it obeys the scaling form

$$\chi_a(k_\perp, k_\parallel, \omega) = |\omega|^{\delta_a} F_a \left[\frac{|\omega|}{|k_\parallel|^{z_b}}, \frac{k_\perp}{k_\parallel^2} \right], \tag{4.18}$$

with z_b the boson dynamic critical exponent, the power $\delta_a = 1 + (3 - 4\phi_{u_a})/z_b$, and F_a is a scaling function. For the limit of physical interest $(N, \epsilon = 1)$ and taking the angle $\theta = 0$ (where the electron-boson coupling is strongest), the power is

$$\delta_a = \frac{2}{3}\left[1 - \frac{g(\sqrt{3}R_a/\pi, z_b = 3)}{R_a} \right]. \tag{4.19}$$

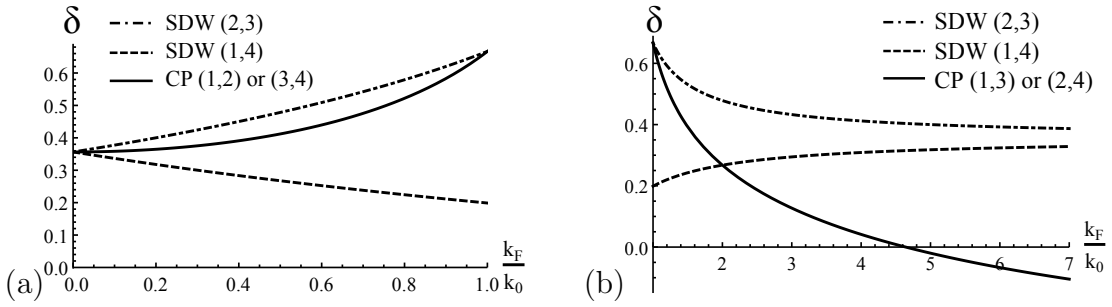

Figure 4.4: Susceptibility scaling exponents. Scaling exponents δ_a for susceptibilities $\chi_a(\omega) \sim |\omega|^{\delta_a}$ of various orders, a, that are enhanced by the interaction between electrons and overdamped spin-waves. CP/SDW (j, j') denotes Cooper pairing or spin density wave between patches j and j' (see Figure 4.2 for our patch labeling convention). Results are shown as a function of electron density, parameterized by the ratio k_F/k_0. (a) Lower doping of the Rashba liquid (annular Fermi surface), when $0 < k_F/k_0 < 1$. In this case the susceptibilities are mildly enhanced but no instability develops. Curves correspond to Cooper pairing between either $(1, 2)$ or $(3, 4)$ (solid), SDW order between $(1, 4)$ (dashed), and SDW order between $(2, 3)$ (dot-dashed). (b) Concentric Fermi surface, given by $k_F/k_0 > 1$. Curves correspond to Cooper pairing between either $(1, 3)$ or $(2, 4)$ (solid), SDW order between $(1, 4)$ (dashed), and SDW order between $(2, 3)$ (dot-dashed). At high densities $k_F \gg k_0$, nesting in the Cooper channel is approximately restored by the strong spin-orbit coupling and a superconducting instability develops (indicated by $\delta_{\text{CP}} < 0$), corresponding to diverging susceptibility.

The functional form of $g(x, z_b)$ is given in Section 4.9 and is independent of the susceptibility channel. R_a is a dimensionless ratio weighing the mass contribution in the Landau damping γ, which originates from both inner and outer Fermi surfaces, against a channel (a) dependent "effective" density of states of the two patches under consideration. δ_a is a monotonically increasing function of R_a.

Figure 4.4 shows a central result of our work. The value of the power δ_a for the four channels of interest is plotted as a function of the more tunable parameter k_F/k_0 which increases monotonically with chemical potential, $k_F/k_0 \sim \sqrt{\mu}/(\sqrt{m_0}\alpha_R)$. Evidently, the susceptibilities in the particle-hole channel, at all dopings, and Cooper channel, for the annular FS at low dopings, remain finite. Only in the case of Cooper pairing at higher dopings, in the concentric Fermi surface regime, is there potential for a singularity in the susceptibility. This is to be expected. At high dopings when $k_F \gg k_0$, one asymptotically restores the time-reversal symmetry nested Fermi surfaces which increases the susceptibility to superconductivity, though this is not the limit of physical interest. In this case, the use of a full Fermi surface RG scheme would be necessitated as in [115].

Finally, we remark that for sufficiently low densities and strong magnetization M_0, the Fermi surface has only a single "banana" shaped pocket centered at nonzero momentum perpendicular to the magnetic ordering direction (see for instance [116, 117]). In this regime

only the Cooper pairing $(1, 2)$-type channels are available, and our analysis again suggests that this regime is also a stable NFL.

4.6 Experimental Considerations

Having explained the basic phenomenology of the NFL phase, we now discuss two potential issues for observing the predicted NFL physics in real materials and indicate some potentially promising candidate systems.

Crystal Anisotropy

The assumption of continuous rotation symmetry crucial to the presence of Goldstone modes in this work is clearly broken explicitly in crystalline systems, where only discrete rotational symmetry remains. Therefore, we expect such NFL physics to be present at energy scales above that set by the crystal pinning scale, below which the Goldstone mode acquires a mass.

It is therefore desirable to minimize the effects of crystal anisotropies. To this end, materials with three- or six-fold rotation symmetries are preferable to those with four-fold rotation symmetry. For the former, crystal anisotropies enter at order $\mathcal{O}(k_0 a)^3$, where a is the lattice spacing, whereas the latter permit $\mathcal{O}(k_0 a)^2$ cubic anisotropy terms. Therefore, in the low-density regime ($k_F a \ll 1$), three- or six-fold anisotropies permit a larger parametric separation between the spin-orbit scale $\mathcal{O}(k_0 a)^2$ and the crystal pinning scale $\mathcal{O}(k_0 a)^3$.

Disorder Effects

A second practical consideration is minimizing disorder. The effects of disorder are twofold. First, at temperatures less than the elastic scattering rate τ^{-1}, elastic scattering of electrons from impurities dominates the inelastic scattering from spin-waves and the electrons obey diffusive dynamics.

Secondly, due to the spin-orbit coupling, impurities couple to the ferromagnetic spin texture as a random field. Familiar Imry-Ma arguments show that this leads to random pinning of the magnetic order parameter for temperatures below some characteristic energy scale E_{IM}. Interestingly, if $\tau^{-1} \gg E_{\mathrm{IM}}$, then there will still be a broad range where the spin-waves are overdamped by the diffusive fermions with damping rate $\sim q^2$ (rather than damping rate $\sim q^3$ characteristic of Landau damping [101]).

While disorder inevitably spoils NFL physics at asymptotically low temperatures, we estimate that, for reasonably clean systems, there can be a broad intermediate temperature range $E_{\mathrm{NFL}} \gg T \gg \tau^{-1}, E_{\mathrm{IM}}$ over which the NFL physics described above may be observed. Analysis of disorder is provided in Section 4.10.

Candidate Materials

Promising materials with strong Rashba spin-orbit coupling and six-fold rotation symmetry include surface alloys, such as Bi/Ag(111) [123–126]. A complicating detail is that these surface alloys contain not only 2D SOC surface states but also 3D bulk metallic states. However, we do not expect any important modifications from the accompanying bulk states, as the surface states inhabit regions of the surface Brillouin zone unoccupied by bulk metallic states. In particular, the bulk states lack strong spatial (as opposed to atomic) spin-orbit coupling and hence dynamically decouple from the spin-waves as for more conventional Goldstone mode problems. Moreover, the coupling of surface to bulk states is irrelevant for the NFL phase since the NFL physics arises from singular small momentum transfer scattering between electrons and spin-waves, which cannot connect bulk and surface states which are widely separated in momentum space.

Various semiconductor heterostructures [127, 128] may also be promising due to their high mobilities. We note in passing that materials with Dresselhaus spin-orbit coupling $H_D \sim \alpha_D(\sigma^x k_x - \sigma^y k_y)$ and a spin-spin coupling between electrons and an XY magnetic order parameter $\boldsymbol{M}$ are expected to give rise to similar physics. The Dresselhaus coupling preserves a continuous rotation-like symmetry of combined in-plane rotations $\mathcal{R}(\theta)$ on $\boldsymbol{M}, \boldsymbol{\sigma}$ and $\mathcal{R}(-\theta) = \mathcal{R}^T(\theta)$ on $\boldsymbol{k}$ which is spontaneously broken in the ground state, giving rise to a rotational Goldstone mode. However, the combination of both Dresselhaus and Rashba spin-orbit couplings inevitably breaks the continuous rotation symmetry and does not lead to NFL behavior.

Topological insulator (TI) surface states are also promising candidates. Since the TI surface states lack a natural tendency towards spontaneous ferromagnetism, it may be induced by proximity in heterostructure devices between TIs and a ferromagnetic insulator [129] (e.g. EuO or EuS [130]). Ferromagnetism can also be induced in TIs by magnetic dopants. Here, however, care must be taken to minimize the detrimental effects of disorder which obscure the NFL phase.

Having identified some promising experimental candidates for observing NFL behavior, we now describe how the phase may be experimentally detected.

Experimental Phenomenology

Thermodynamic Signatures

In the NFL regime, the specific heat exhibits a distinct power law temperature dependence, $C_v \sim T^{1/z_f} \sim T^{2/3}$, which follows directly from the scaling properties of the NFL phase (see e.g. [103] and references therein). This quantity may be difficult to measure for a non-layered 2D electron system as the electronic C_v is likely dominated by bulk contributions. Therefore, in subsequent sections we describe nonthermodynamic probes based on tunneling spectroscopy and electrical transport that may be more experimentally accessible.

Spectroscopic Probes

The characteristic NFL scattering rate can be directly detected by measuring the frequency dependence of linewidths in angle-resolved photoemission spectroscopy. Also, the overdamped character of the spin-waves may also be observable in inelastic spectroscopy. As for heat capacity, neutron scattering is not feasible for nonlayered 2D samples, but Raman spectroscopy could be used.

Additionally, repeated scattering between electrons and spin-waves produces a singular correction to the tunneling density of states, $N(\omega) \sim |\omega|^{\eta_f/z_f}$, [108, 113] that could be observed in tunneling experiments or by photoemission. Here, η_f is an anomalous correction to the electron operator scaling dimension which appears at three and higher loop order in field theory calculations [108, 113].

Electrical Transport

The NFL phase described above is also expected to exhibit an unusual power in the temperature dependence of the electrical resistivity. Early studies [131, 132, 102, 133] predicted $\rho(T) \sim T^{4/3}$ based on the scattering rate of electrons by overdamped bosons. However, this answer is likely incorrect, as momentum transferred between electrons to spin-waves is not necessarily dissipated [134]. Rather, in a clean system the momentum transferred to the spin-waves eventually returns to these electrons due to drag effects leading to vanishing resitivity. Nonzero resistivity develops only from translation symmetry-breaking due to impurities or umklapp scattering (the latter is typically unimportant at low temperatures [134, 135]).

Transport for a related NFL nematic quantum critical point (QCP) in a metal was recently investigated in [134] using memory matrix techniques. There, it was found that the dominant source of temperature-dependent resistivity came from indirect momentum loss of the nematic order parameter to impurities. In particular, it was shown [134] that the results of the more sophisticated memory matrix computation can be reproduced by computing a simple low-order process in which electrons scatter from spin-waves, which subsequently lose momentum to an impurity corresponding to the diagram shown in Figure 4.5. Here we expect similar physics to hold in the NFL regime. One important difference is that whereas the nematic order parameter develops a thermal mass at finite temperature, in the present context, the magnons are Goldstone modes and cannot develop a thermal mass for $T < T_M$.

As described in Section 4.10,

$$\rho_{\mathrm{NFL}}(T) \sim T^{2/3}. \tag{4.20}$$

This contribution to resistivity coexists with a constant contribution and other more conventional temperature-dependent contributions from phonon scattering ($\sim T^5$) and short-range electron-electron interactions via screened Coulomb potential ($\sim T^2$). These contributions

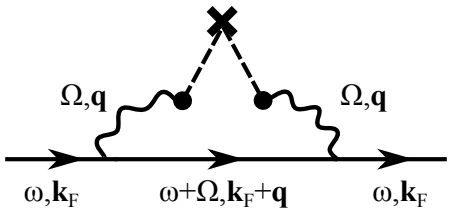

Figure 4.5: Disorder diagram for resistivity. Diagrammatic representation of the indirect disorder scattering process that is expected to set the dominant NFL correction to the temperature dependence of electrical resistivity. Here straight lines indicate electron propagators, wavy lines are spin-waves and dashed lines terminating at a cross indicate disorder vertices (the connection between two such lines arises from disorder averaging).

may be distinguished from those due to spin-wave scattering by applying an in-plane magnetic field. This pins the ferromagnetic order, gaps the spin-waves, and thereby suppresses the NFL resistivity contributions. By contrast, the phonon and electron-electron scattering contributions are expected to have only weak field dependence. Hence, by comparing resistivity with and without a field one can extract the NFL contribution.

4.7 Conclusion

In this chapter, we described how Fermi liquid theory breaks down in spin-orbit coupled metallic ferromagnets with broken continuous rotational symmetry and have highlighted experimentally testable signatures of this non-Fermi liquid phase. Most importantly, we find that this NFL is stable to subsidiary spontaneous symmetry breaking. Unlike the related nematic metal problem, the spin-orbit coupled metallic ferromagnets do not suffer an instability towards superconductivity due to the absence of time-reversal and inversion symmetries. We also analyzed instabilities in other pairing and spin density wave channels within a controlled (N, ϵ) expansion [113]. While certain susceptibilities receive nonanalytic enhancements from strong spin-wave-mediated interactions, we find that no instabilities develop over a wide range of carrier densities.

The realization of this NFL phase is likely experimentally feasible. Promising candidate materials include surface alloys, topological insulator surface states, and semiconductor heterostructures. While related NFLs are expected to arise in more exotic contexts like quantum critical points in metals or gapless spin liquids with emergent gauge fields, spin-orbit coupled metallic ferromagnets offer an experimentally accessible and comparatively simple platform for exploring the physics of correlated gapless quantum phases without quasiparticles.

4.8 Appendix A: Boson Polarization and Electron Self-Energy

Preliminaries

We first solve for the 2D Rashba band structure in the presence of a uniform magnetization and introduce notation that we will use throughout the calculations in the appendices. The Rashba Hamiltonian in the presence of a uniform magnetization $\boldsymbol{M} = M_0\hat{\boldsymbol{e}}_{\boldsymbol{M}}$ is

$$H_0 = \frac{k^2}{2m_0} - \tilde{\mu} + \alpha_R \hat{\boldsymbol{z}} \cdot (\mathbf{k} \times \boldsymbol{\sigma}) - \lambda_0 M_0 \hat{\boldsymbol{e}}_{\boldsymbol{M}} \cdot \boldsymbol{\sigma} \tag{4.21}$$

and acquires a band structure with dispersion

$$E(k,\theta) = \frac{(k - \eta' k_0)^2}{2m_0} - \mu - \eta' \lambda_0 M_0 \sin(\theta), \tag{4.22}$$

where $\eta' = +1$ (-1) denotes the lower (upper) Rashba bands, $k_0 \equiv m_0\alpha_R$, $\mu = \tilde{\mu} + m_0\alpha_R^2/2$, and θ is measured from the direction of $\hat{\boldsymbol{e}}_{\boldsymbol{M}}$. We further let $\eta = +1$ (-1) denote the outer (inner) Fermi surface. Defining $k_F(\theta) \equiv \sqrt{2m_0(\mu + \eta'\lambda_0 M_0 \sin(\theta))}$, the radius of a Fermi surface is $\eta'(k_0 + \eta k_F) > 0$ assuming there is a Fermi surface at the given angles and doping and not a Fermi pocket. As discussed previously, the calculations are greatly simplified by breaking the Fermi surface into patches, a representative set of which was shown in Figure 4.2, labeled by numbers $1 - 4$. Low-energy quasiparticles in a patch obey the dispersion $\varepsilon = vk_\perp + \frac{k_{||}^2}{2m}$, with $k_\perp, k_{||}$ coordinates that are perpendicular, parallel to the Fermi surface and are fixed with respect to a set of patches. The proper signs are accounted for with a signed velocity and effective mass $|v| = k_F/m_0$, $m = m_0(1+\eta\frac{k_0}{k_F})$. Finally, we let $k_F^{>,<}$ denote $k_F^{>,<}$ the radius of the outer and inner Fermi surfaces.

The full fluctuating magnetization is parameterized as $\boldsymbol{M} = M_0\left[\hat{\boldsymbol{e}}_{\boldsymbol{M}}\cos\phi + (\hat{\boldsymbol{z}} \times \hat{\boldsymbol{e}}_{\boldsymbol{M}})\sin\phi\right]$ and we expand for small fluctuations ϕ and replace $M_0\phi \to \phi$. We will denote $\lambda(\hat{\boldsymbol{n}}_{\boldsymbol{j}})$ the coupling to the Goldstone mode, where $\hat{\boldsymbol{n}}_{\boldsymbol{j}}$ is a unit vector in the direction of patch j. The functional dependence of $\lambda(\hat{\boldsymbol{n}}_{\boldsymbol{j}})$ is given in Eq. 4.13.

The Hamiltonian for the TI surface state is

$$H_0 = v_D \hat{\boldsymbol{z}} \cdot (\mathbf{k} \times \boldsymbol{\sigma}) - \lambda_0 M_0 \hat{\boldsymbol{e}}_{\boldsymbol{M}} \cdot \boldsymbol{\sigma} - \mu. \tag{4.23}$$

If we solve H_0 exactly, the effect of the magnetization, which couples like a gauge field to the fermions, is only to shift the center of the Dirac cone. There are in general higher order in $\boldsymbol{k}$ corrections in the Hamiltonian which will explicitly break the continuous rotational symmetry of the Fermi surface, but we neglect these. The case of the TI surface state is accounted for within the treatment of the Rashba spin-orbit coupled system. The patch

dispersion for the TI is $\varepsilon = v_D k_\perp + \frac{v_D^2 k_{||}^2}{2\mu}$, and so the special case of the TI surface state is accounted for within the treatment of the Rashba liquid if we let the patch velocity $v = v_D$ and mass $m = \mu/v_D^2$.

Lagrangian Density within the (N, ϵ) expansion

The dual (N, ϵ) expansion of [113] introduces N fermion flavors, which we index by μ, and a control parameter ϵ related to the boson dynamic critical exponent z_b as $\epsilon \equiv z_b - 2 > 0$. Our bare Euclidean action for a set of collinear patches, indexed by j ranging from $1-4$, within this expansion is

$$\begin{aligned} S_E &\equiv S_0 + S_{\text{int}}, \\ S_0 &\equiv \int \frac{d\omega d^2k}{(2\pi)^3} \left[N c^{z_b-1} |k_{||}|^{z_b-1} |\phi_{\omega,\boldsymbol{k}}|^2 + \sum_{\mu,j} \psi^{\dagger,\mu}_{j,\omega,\boldsymbol{k}} (-i\omega + v_j k_\perp + \frac{k_{||}^2}{2m_j}) \psi^{\mu}_{j,\omega,\boldsymbol{k}} \right], \\ S_{\text{int}} &\equiv \sum_{\mu,j} \int \frac{d\omega d^2k d\Omega d^2q}{(2\pi)^6} \left[\lambda(\hat{\boldsymbol{n}}_{\boldsymbol{j}}) \phi_{\Omega,\boldsymbol{q}} \psi^{\dagger\mu}_{j,\omega+\Omega,\boldsymbol{k}+\boldsymbol{q}} \psi^{\mu}_{j,\omega,\boldsymbol{k}} \right]. \end{aligned} \tag{4.24}$$

(The μ flavor index will be omitted when it is unnecessary to track.) We define our initial free propagators

$$\begin{aligned} \langle |\phi_{\omega,\boldsymbol{k}}|^2 \rangle &= \frac{(2\pi)^3}{N c^{z_b-1} |k_{||}|^{z_b-1}} \equiv (2\pi)^3 D_0(\omega, \boldsymbol{k}), \\ \langle \psi^{\mu}_{j,\omega,\boldsymbol{k}} \psi^{\dagger\mu}_{j,\omega,\boldsymbol{k}} \rangle &= \frac{(2\pi)^3}{-i\omega + \varepsilon_j} \equiv (2\pi)^3 G_0^j(\omega, \boldsymbol{k}), \\ \varepsilon_j &= v_j k_\perp + \frac{k_{||}^2}{2m_j}. \end{aligned} \tag{4.25}$$

The action Eq. 4.24 will generate the one-loop boson polarization and fermion self-energy, which will give the NFL action around which we will work perturbatively in computing the susceptibility to order in Section 4.9.

One-Loop Boson Polarization

The boson polarization is defined using Dyson's equation as $D^{-1} = D_0^{-1} + \Pi$ and its one-loop correction is

$$\Pi(\Omega, \boldsymbol{q}) = N \sum_j \lambda(\hat{\boldsymbol{n}}_{\boldsymbol{j}})^2 \int \frac{d\omega dk_{||} dk_\perp}{(2\pi)^3} G_0^j(\omega, \boldsymbol{k}) G_0^j(\omega + \Omega, \boldsymbol{k} + \boldsymbol{q}). \tag{4.26}$$

The integrals are performed in the order $k_\perp, \omega, k_{||}$ resulting in

$$\Pi(\Omega, \boldsymbol{q}) = N \sum_j \lambda(\hat{\boldsymbol{n}}_{\boldsymbol{j}})^2 \frac{|m_j|}{4\pi |v_j|} \frac{|\Omega|}{|q_{||}|} \equiv N\gamma \frac{|\Omega|}{|q_{||}|}, \tag{4.27}$$

which defines the Landau damping coefficient γ dependent on the patch velocity, mass, and effective coupling λ to the Goldstone mode.

The boson velocity is expected to be renormalized by the fermions, via e.g. the diagram in Figure 4.3, and hence acquire a component proportional to v_F. Using $\Omega \sim v_F q$, the energy scale below which damped dynamics dominates is the Landau damping energy scale $E_{\mathrm{LD}} \sim (\gamma v_F)^{\frac{1}{2}}$. Consider the patches at $\theta = 0$ for illustration, where the masses of patches $1-4$ (Figure 4.2) are $|m_1| = |m_3|, |m_2| = |m_4|$ and $\gamma \sim \lambda_0^2 \frac{(|m_1|+|m_2|)}{v_F}$. Defining $x \equiv k_F(\theta = 0)/k_0 \geq 0$, a quantity which increases monotonically with doping, we have

$$E_{\mathrm{LD}} \sim \lambda_0 \sqrt{\frac{m_0}{x}} \left[x + 1 + |x-1|\right]^{\frac{1}{2}}. \tag{4.28}$$

Varying only the chemical potential while fixing the other parameters, the Fermi momentum $k_F \sim \sqrt{\mu}$ and so the damping energy scale $E_{\mathrm{LD}} \sim \mu^{-\frac{1}{4}}$ for low doping $\mu \ll m_0 \alpha_R^2$ while it approaches a constant at high doping $\mu \gg m_0 \alpha_R^2$.

One-Loop Electron Self-Energy

We feed the Landau damped boson propagator back into the electron self-energy, focusing on a single patch j, and compute the non-Fermi liquid frequency dependence. The self-energy is defined as $(G^j)^{-1} \equiv (G_0^j)^{-1} - \Sigma_j = -i\omega + \varepsilon_j(\boldsymbol{k}) - \Sigma_j(\omega)$ at $\boldsymbol{k} = 0$. We focus on the frequency dependence because within the RPA, the momentum dependence is expected to be infrared nonsingular [113].

$$\begin{aligned}
\Sigma_j(\omega, 0) &= \lambda(\hat{\boldsymbol{n}}_{\boldsymbol{j}})^2 \int \frac{d\Omega dq_{||} dq_\perp}{(2\pi)^3} D(\Omega, \boldsymbol{q}) G_0^j(\omega - \Omega, -\boldsymbol{q}) \\
&= i \frac{\mathrm{sgn}(\omega)}{\zeta N} |\omega|^{2/z_b}, \\
\zeta &\equiv 4\pi \frac{|v_j|}{\lambda(\hat{\boldsymbol{n}}_{\boldsymbol{j}})^2} \gamma^{(z_b-2)/z_b} c^{2(1-\frac{1}{z_b})} \sin(2\pi/z_b) \qquad (4.29) \\
&\approx \left(\frac{2\pi^2 c |v_j|}{\lambda(\hat{\boldsymbol{n}}_{\boldsymbol{j}})^2}\right) \epsilon \qquad (\text{for } \epsilon \ll 1). \qquad (4.30)
\end{aligned}$$

We use the form of the propagator to estimate the scale below which NFL sets in, denoted E_{NFL}, for the physically relevant case $z_b = 3, N = 1$. This scale is $E_{\mathrm{NFL}} = \zeta^{-3}$; setting $\theta = 0$, where the coupling is maximal, and $x \equiv k_F/k_0$,

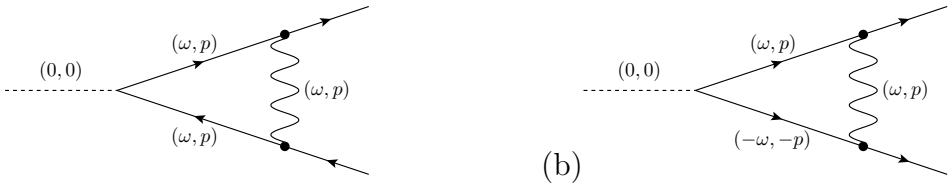

Figure 4.6: Diagrams for NFL enhancement of susceptibilities. Vertex correction for coupling to an external field u (dashed) due to the interaction between electrons (solid) and Goldstone boson (wavy). The two channels are (a) particle-hole and (b) Cooper pair.

$$E_{\rm NFL} \sim \frac{\lambda_0^4}{k_0^2 c^4} \frac{m_0}{x\left[1+x+|1-x|\right]}. \tag{4.31}$$

Since $k_F \sim \sqrt{\mu}$, $E_{\rm NFL} \sim 1/\sqrt{\mu}$ for $\mu \ll m_0 \alpha_R^2$ while $E_{\rm NFL} \sim 1/\mu$ for $\mu \gg m_0 \alpha_R^2$. As would be expected, the non-Fermi liquid energy scale vanishes as $\mu \to \infty$.

4.9 Appendix B: Patch Susceptibilities

We consider the finite momentum particle-hole and Cooper pair susceptibilities for patches within a collinear set in the Rashba system. We add a term $S_{\rm ext}$ to the action which couples an external field u to electron patch bilinears and compute the renormalization of the coupling due to the electron-boson interaction. The modified scaling dimension of the coupling will yield the scaling form for the susceptibility to ordering in a channel. The leading order in ϵ (equivalently, $1/N$ since $\epsilon N \sim O(1)$) correction comes from Figure 4.6.

The action consists of $S_0 + S_{\rm int} + S_{\rm ext}$ with $S_{\rm int}$ from Eq. 4.24 but the noninteracting boson and fermion actions modified to include Landau damping and the NFL self-energy:

$$S_0 = N \int \frac{d\omega d^2k}{(2\pi)^3} \left[c^{z_b-1} |k_{||}|^{z_b-1} + \gamma \frac{|\omega|}{|k_{||}|} \right] |\phi_{\omega,\boldsymbol{k}}|^2 \ldots + \sum_{\mu,j} \int \frac{d\omega d^2k}{(2\pi)^3} \psi_j^{\dagger\mu} \left[-\frac{i\ \mathrm{sgn}(\omega)}{\zeta N} |\omega|^{2/z_b} + v_j k_\perp + \frac{k_\parallel^2}{2m_j} \right] \psi_j^\mu. \tag{4.32}$$

$S_{\rm ext}$ has the general form $S_{\rm ext} = \int d^2x d\tau \left[u_a \mathcal{O}_a(\boldsymbol{x},\tau) + h.c. \right]$ and depends on the channel (a) under consideration. For instance, $\mathcal{O}_a(\boldsymbol{x},\tau) = \psi_1^\dagger \psi_4(\boldsymbol{x},\tau)$ for the $a = 2k_F^>$ SDW channel. The RG scheme involves integrating out low-energy electron and boson modes simultaneously. The RG scaling transformations which keep S_0 invariant are given in Eq. 4.6; note that the $\perp, ||$ directions rescale differently. To carry out the RG, we use $\int_> d\omega dk_\parallel dk_\perp$ which integrates over all $\omega, k_\perp \in (-\infty, \infty)$ but over $|k_\parallel| \in \left[\Lambda/\sqrt{b}, \Lambda\right]$.

The renormalized scaling dimension of the external field u_a can be related to the scaling form of the correlations. If $u'_a = b^{\phi_{u_a}} u_a$ under renormalization, the order parameter $\mathcal{O}_a(\boldsymbol{x}, \tau)$ to which u_a couples transforms as $\mathcal{O'}_a(\boldsymbol{x'}, \tau') = b^{\frac{(z_b+3)}{2} - \phi_{u_a}} \mathcal{O}_a(\boldsymbol{x}, \tau)$. We define χ_a as the Fourier transform of the two-point correlation $\langle \mathcal{O}^*_a(\boldsymbol{x}, \tau) \mathcal{O}_a(0,0) \rangle$ and it obeys the relation

$$\chi_a(\boldsymbol{k}, \omega) = b^{2\phi_{u_a} - \frac{(z_b+3)}{2}} \chi'_a(\boldsymbol{k'}, \omega'), \tag{4.33}$$

leading to the scaling form

$$\chi_a(k_\perp, k_\parallel, \omega) = |\omega|^{\delta_a} F_a \left[\frac{|\omega|}{|k_\parallel|^{z_b}}, \frac{k_\perp}{k_\parallel^2} \right], \tag{4.34}$$

with the power $\delta_a = 1 + \frac{(3 - 4\phi_{u_a})}{z_b}$ and scaling function F_a.

As the Goldstone mode mediates repulsive interactions in the particle-hole channel and attractive interactions in the finite momentum Cooper channel, correlations in these channels are expected to be enhanced compared to the usual Rashba Fermi liquid and hence are of interest for potential singularities. We turn to these next.

$2k_F^{<,>}$ Particle-Hole Susceptibility

We compute the one-loop correction to the coupling $S_{\text{ext}} = \int d^2x d\tau \left[u_a \psi_j^\dagger \psi_{j'} + h.c. \right]$ with $a = 2k_F^>$ or $2k_F^<$. From this, we obtain the particle-hole susceptibility to SDW order within patch pairs $(j, j') = (1, 4)$ and $(2, 3)$ in a collinear set, corresponding to finite momentum $2k_F^>$ and $2k_F^<$, respectively. This channel is relevant for both the annular and concentric Fermi surface regimes.

Fermions have dispersion $\varepsilon_j = v_j k_\perp + \frac{k_\parallel^2}{2m_j}$ for patch j at angle θ and couple via λ_j to the Goldstone mode with the opposite sign $\text{sgn}(\lambda_j) = -\text{sgn}(\lambda_{j'})$ between patches in a pair. Setting external momenta and frequencies to zero, the vertex correction gives

$$\begin{aligned} \delta u &= u \lambda_j \lambda_{j'} \int_> \frac{d\omega dk_\parallel dk_\perp}{(2\pi)^3} G^j(\omega, \boldsymbol{k}) G^{j'}(\omega, \boldsymbol{k}) D(\omega, \boldsymbol{k}) \\ &= \frac{iu}{N} \lambda_j \lambda_{j'} \int_> \frac{d\omega dk_\parallel}{(2\pi)^2} \frac{\Theta(\omega/v_j) - \Theta(\omega/v_{j'})}{\left[\frac{k_\parallel^2}{2} \left(\frac{v_j}{m_{j'}} - \frac{v_{j'}}{m_j} \right) - \frac{i \text{sgn}(\omega)}{N} \left(\frac{v_j}{\zeta'} - \frac{v_{j'}}{\zeta} \right) |\omega|^{\frac{2}{z_b}} \right] \left[\gamma \frac{|\omega|}{|k_\parallel|} + c^{z_b - 1} |k_\parallel|^{z_b - 1} \right]}. \end{aligned} \tag{4.35}$$

For the patches under consideration, the velocities $v_j, v_{j'}$ have opposite sign while $m_j, m_{j'}$ have the same sign. Defining $\alpha \equiv \frac{|v_j|}{\zeta'} + \frac{|v_{j'}|}{\zeta}$ and $\beta \equiv \frac{|v_j|}{|m_{j'}|} + \frac{|v_{j'}|}{|m_j|}$, one obtains

$$\frac{d(\delta u)}{dl} = - u \frac{\lambda_j \lambda_{j'}}{\pi^2 \gamma N} \left[\frac{|v_j|}{|m_{j'}|} + \frac{|v_{j'}|}{|m_j|} \right]^{-1} \cdot g(x, z_b),$$

$$g(x,z_b) \equiv \int_0^\infty dt \frac{x t^{2/z_b}}{(x^2+t^{4/z_b})(1+t)},$$
$$x \equiv \frac{N\beta\gamma^{2/z_b}}{2\alpha c^{2(1-1/z_b)}} > 0. \tag{4.36}$$

Both ζ, ζ' have a leading linear in ϵ behavior so $x \sim \epsilon N$. Note that $d(\delta u)/dl > 0$ so correlations will be enhanced.

The Goldstone mode also mediates repulsive interactions for other patch pair types, e.g. $(1,3)$, $(2,4)$ for the annular Fermi surface or $(1,2)$, $(3,4)$ for the concentric Fermi surface. In principle we would be interested in these on grounds that they might be enhanced. However, here patch pairs have the same sign velocity, giving rise to $k_\perp$ poles on the same side of the complex plane when external lines carry no frequency. Finite values in the external lines would contribute to a renormalization of $u(\boldsymbol{k},\omega)$ with finite arguments, which is less relevant than $u(0,0)$.

$k_F^> \pm k_F^<$ Cooper Channel Susceptibility

Similarly, we compute the vertex correction to the coupling $S_{\text{ext}} = \int d^2x d\tau \left[u_a \psi_j^\dagger \psi_{j'}^\dagger + h.c.\right]$ with $a = k_F^> \pm k_F^<$. This yields the susceptibility scaling form for superconducting order within patch pairs $(j,j') = (1,2)$ and $(3,4)$ for the annular Fermi surface and $(1,3)$ or $(2,4)$ for the concentric Fermi surface.

The coupling to the Goldstone mode has the same sign $\text{sgn}(\lambda_j) = \text{sgn}(\lambda_{j'})$ for patches in a pair. Setting external momenta and frequencies to zero gives

$$\delta u = u\lambda_j\lambda_{j'} \int_> \frac{d\omega dk_\parallel dk_\perp}{(2\pi)^3} G^j(\omega,\boldsymbol{k}) G^{j'}(-\omega,-\boldsymbol{k}) D(\omega,\boldsymbol{k}) \tag{4.37}$$
$$= +\frac{iu}{N}\lambda_j\lambda_{j'} \int_> \frac{d\omega dk_\parallel}{(2\pi)^2} \frac{\Theta(\omega/v_j) - \Theta(\omega/v_{j'})}{\left[\frac{k_\parallel^2}{2}\left(\frac{v_j}{m_{j'}} + \frac{v_{j'}}{m_j}\right) + \frac{i\text{sgn}(\omega)}{N}|\omega|^{\frac{2}{z_b}}\left(\frac{v_j}{\zeta'} - \frac{v_{j'}}{\zeta}\right)\right]\left[\gamma\frac{|\omega|}{|k_\parallel|} + c^{z_b-1}|k_\parallel|^{z_b-1}\right]}. \tag{4.38}$$

For the patches under consideration, the velocities $v_j, v_{j'}$ are opposite in sign while $m_j, m_{j'}$ may have opposite (annular Fermi surface) or the same sign (circular Fermi surface). Define $\alpha \equiv \frac{|v_j|}{\zeta'} + \frac{|v_{j'}|}{\zeta}$ and $\beta \equiv \left|\frac{|v_j|}{|m_{j'}|} \pm \frac{|v_{j'}|}{|m_j|}\right|$, where the $\pm$ is for the annular/concentric Fermi surface cases. The computation is otherwise the same as for the particle-hole channel and yields

$$\frac{d(\delta u)}{dl} = u\frac{\lambda_j\lambda_{j'}}{\pi^2\gamma N}\left|\frac{|v_j|}{|m_{j'}|} \pm \frac{|v_{j'}|}{|m_j|}\right|^{-1} \times g(x,z_b), \tag{4.39}$$

with $x, g(x,z_b)$ defined as before. Note again that $d(\delta u)/dl > 0$.

Evaluation

Within this RG scheme, we can take the limit $\epsilon \to 0, N \to \infty$ with ϵN finite. For both the particle-hole and Cooper channels, we find a modified scaling dimension $u'_a = b^{\phi_{u_a}} u_a$ (including the bare value $\phi_{u_a} = 1$) to leading order in ϵ:

$$\phi_{u_a} = 1 + \epsilon \frac{|\lambda_j \lambda_{j'}|}{\pi^2 \gamma \epsilon N} \left| \frac{|v_j|}{|m_{j'}|} \pm \frac{|v_{j'}|}{|m_j|} \right|^{-1} g(\bar{x}, z_b = 2), \tag{4.40}$$

$$\begin{aligned} g(x, z_b = 2) &= \frac{\pi x^2}{2(1+x^2)} \left[1 - \frac{2}{\pi x} \log(x) \right], \\ \bar{x} \equiv \lim_{\substack{N\to\infty \\ \epsilon \to 0}} x &= (\epsilon N) \pi^2 \gamma \left[\frac{\lambda_{j'}^2 |v_j|}{|v_{j'}|} + \frac{\lambda_j^2 |v_{j'}|}{|v_j|} \right]^{-1} \left| \frac{|v_j|}{|m_{j'}|} \pm \frac{|v_{j'}|}{|m_j|} \right|. \end{aligned} \tag{4.41}$$

Here the lower sign is for the concentric Fermi surface Cooper channel; the upper sign applies otherwise. This gives a scaling form $\chi_a(k_\parallel, k_\perp, \omega) = |\omega|^{\delta_a} F_a(|\omega|/|k_\parallel|^{z_b}, k_\perp/k_\parallel^2)$ with exponent[4]

$$\delta_a = \frac{1}{2} + \frac{\epsilon}{4} \left[1 - \frac{8|\lambda_j \lambda_{j'}|}{\pi^2 \gamma} \left| \frac{|v_j|}{|m_{j'}|} \pm \frac{|v_{j'}|}{|m_j|} \right|^{-1} \frac{g(\bar{x}, z_b = 2)}{\epsilon N} \right] + \mathcal{O}(\epsilon^2) \tag{4.42}$$

As an example, we simplify to the most important case $\theta = 0$, $|v_j| = |v_{j'}| \equiv v, |\lambda_j| = |\lambda_{j'}| \equiv \lambda$ and masses $|m_1| = |m_4|, |m_2| = |m_3|$. These patches couple most strongly to the Goldstone mode and hence will receive the strongest singular enhancement of susceptibilities. In this case, $\gamma = \lambda^2(|m_1| + |m_2|)/(2\pi v)$. It is convenient to define a dimensionless ratio R_a for each channel a,

$$R_a \equiv \frac{\pi}{4} \frac{(|m_1| + |m_2|)\,||m_j| \pm |m_{j'}||}{|m_j||m_{j'}|}, \tag{4.43}$$

where $m_j, m_{j'}$ are chosen based on the channel of interest (lower sign is for concentric Fermi surface Cooper channel, upper sign otherwise). Expressions for R_a for the various channels are given in Table 4.1 as a function of the mass ratio $r_M = |m_2|/|m_1| \in (0, 1)$. Physically, R_a can be interpreted as the ratio of the effective density of states for a given channel $\sim |\frac{1}{|m_j|} \pm \frac{1}{|m_{j'}|}|^{-1}$ to the total density of states $\sim (|m_1| + |m_2|)$ that enters the Landau damping coefficient. Qualitatively, Figure 4.7 shows that larger R_a values lead to weaker power law susceptibilities.

[4]Note that the channel a is dependent on patch pair (j, j') being considered.

SDW (1,4)	SDW (2,3)	CP annular FS	CP concentric FS
$\frac{\pi}{2}(1+r_M)$	$\frac{\pi}{2}(1+\frac{1}{r_M})$	$\frac{\pi}{4}\frac{(1+r_M)^2}{r_M}$	$\frac{\pi}{4}\frac{(1-r_M^2)}{r_M}$

Table 4.1: Value of dimensionless mass ratio R_a as a function of $r_M = |m_2|/|m_1| \in (0,1)$.

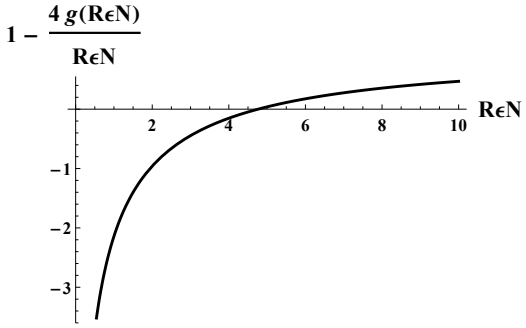

Figure 4.7: Susceptibility exponent function. Plot of $\left[1-4\cdot\frac{g(R_a\epsilon N, z_b=2)}{R_a\epsilon N}\right]$ (with channel dependence a) as a function of $R_a\epsilon N$ which leads to a singular susceptibility for sufficiently negative values. The zero crossing is at $R_a\epsilon N \approx 4.8$ and at large $R_a\epsilon N$ the asymptote is 1.

For general N and ϵ, the value of the susceptibility exponent δ_a is

$$\delta_a = \frac{1}{2} + \frac{\epsilon}{4}\left[1 - 4\cdot\frac{g(R_a\epsilon N, z_b=2)}{R_a\epsilon N}\right]. \tag{4.44}$$

A plot of the coefficient of $\epsilon/4$ is shown in Figure 4.7. The physically interesting limit $N, \epsilon = 1$ lies beyond the controlled regime explored above; we now extrapolate the above results to this case. We still consider the most important case $\theta = 0$. With R_a defined as above, the power law in the scaling form is

$$\delta_a = \frac{2}{3}\left[1 - \frac{g(\sqrt{3}R_a/\pi, z_b=3)}{R_a}\right]. \tag{4.45}$$

We plot δ_a as a function of $x \equiv k_F/k_0$ for all four channels in Figure 4.4, where $r_M = |x-1|/(x+1)$. At the angle $\theta = 0$, $x = \sqrt{2\mu}/(\sqrt{m_0}\alpha_R)$ and therefore increases monotonically with μ. $x = 1$ denotes the Dirac point.

Only the susceptibility in the Cooper channel with concentric Fermi surface has a power law divergence for sufficiently high doping in the Rashba liquid (the zero crossing is at $x \approx 4.6$). We note the Cooper pairing here is within patch pairs $(j, j') = (1,3)$ and $(2,4)$. While the difference in the radii of the two concentric Fermi surfaces stays finite as μ increases, the masses of the two patches approach the same value, mimicking the usual time-reversal symmetric BCS pairing arising from nested scattering.

All the curves except for the particle-hole channel $(1,4)$ peak at $x = 1$ when $m_2 = 0$. One can see that for these other channels, R_a depends on $1/r_M$ and $R_a \to \infty$ as $|m_2| \to 0$. This is because the "effective" density of states, which is some reduced combination of the masses of two patches, is vanishing. For the particle-hole $(1,4)$ channel, R_a instead takes it minimal value at $x = 1$.

Finally, the TI surface can be considered as a special case of the above results, where only a single spin density wave channel may occur. The TI Landau damping coefficient reads $\gamma = \lambda_0^2\mu/(2\pi v_D^3)$ and for $\epsilon \to 0, N \to \infty, \epsilon N$ finite, Eq. 4.44 holds with $R_{2k_F} = \pi/2$, choosing the upper sign. For the case $N, \epsilon = 1$, Eq. 4.45 applies with $R_{2k_F} = \pi/2$ giving $\gamma \approx 0.2$. That is, within the (N, ϵ) approximation the TI surface state is stable against spin density wave formation.

4.10 Appendix C: Disorder Effects and Calculation of Resistivity

In this section, we introduce a model for the impurity and spin-wave coupling and include details of the computation of the temperature dependence of electrical resistivity.

Disorder Model

Symmetry-allowed disorder coupling to the Goldstone mode gives rise to an energy scale E_{IM} near which the physics discussed in this paper break down. We estimate this energy scale below in terms of microscopic quantities and show that for material realizations there will nonetheless be a large energy regime in which NFL physics may still be observed.

A scalar impurity potential $V_{\mathrm{imp}}(r)$ can induce a spin polarization $\mathbf{S}(\mathbf{r}) = \int d^2r' \boldsymbol{\chi}_{S,n}(\mathbf{r} - \mathbf{r}')V_{\mathrm{imp}}(\mathbf{r}')$. $\boldsymbol{\chi}_{S,n}(\mathbf{r})$ is odd under time-reversal and hence must be proportional to the magnetization, approximately $\lambda_0 M_0/\varepsilon_{\mathrm{so}}$ (where $\varepsilon_{\mathrm{so}} = \alpha k_0$, and we have assumed $\lambda_0 M_0 \ll \varepsilon_{\mathrm{so}}$). There is also a mirror symmetry $x \to -x$, where x is the axis of the ordered magnetization, which dictates $\chi^y_{S,n}(\mathbf{r}) \sim \hat{\boldsymbol{x}} \cdot \hat{\boldsymbol{r}}$.

If we consider Coulomb impurities whose atomic-scale internal electric field structures have very short length scale compared to k_F of the electrons (relevant e.g. for semiconductors), then the induced spin density will exhibit $2k_F$ Friedel oscillations, e.g.

$$\langle S^y(\mathbf{r})\rangle \approx \frac{\lambda_0 M_0}{\varepsilon_{\mathrm{so}}} \int d^2r' \frac{k_F^2}{2\pi} F(2k_F|r - r'|)\delta\rho_{\mathrm{imp}}(r') \cdot \left(\hat{M} \cdot \frac{(\mathbf{r} - \mathbf{r}')}{|r - r'|}\right), \tag{4.46}$$

where the last directional factor is required by the mirror symmetry $\langle \mathbf{M}\rangle \to -\langle \mathbf{M}\rangle$, $\delta\rho_{\mathrm{imp}}$ is the density of impurities (with the mean subtracted), and $F(x) \equiv (x\cos x - \sin x)/x^2$ is the oscillatory Friedel screening cloud function. Here, for simplicity we have written expressions valid in the large density limit and, moreover, ignored the NFL corrections to the $2k_F$ susceptibility.

Hence, we can approximately treat the impurities as a random field, coupled to the Goldstone field ϕ,

$$\mathcal{L}_{\text{M-imp}} = -h(\mathbf{r})\phi(\mathbf{r}), \tag{4.47}$$

where $h(\mathbf{r}) \approx \lambda_0 \langle S^y(\mathbf{r})\rangle$.

Therefore, the RMS value of h is

$$\begin{aligned}\overline{h(\mathbf{r_1})h(\mathbf{r_2})} &\approx \left(\frac{\lambda_0^2 M_0}{\varepsilon_{\text{so}}}\right)^2 \rho_{\text{imp}} \delta^2(\mathbf{r_1} - \mathbf{r_2}) \\ &\equiv h_0^2 \delta(\mathbf{r_1} - \mathbf{r_2})\end{aligned} \tag{4.48}$$

Here, we have approximated the rapidly oscillatory $2k_F$ functions with different arguments as zero if $|r_1 - r_2|k_F \gtrsim 1$, which on length scales much longer than k_F^{-1} can be approximately replaced by $k_F^{-2}\delta^2(\mathbf{r_1} - \mathbf{r_2})$.

Temperature Dependence of Resistivity

For simplicity, we treat the random field $h(\mathbf{r})$ as being normally distributed independently for each position $\mathbf{r}$,

$$\overline{h(\mathbf{r})h(\mathbf{r'})} = h_0^2 \delta^2(\boldsymbol{r} - \boldsymbol{r'}), \tag{4.49}$$

where $\overline{(\ldots)}$ indicates averaging over disorder configurations. This approximation is reasonable for weak or dilute impurities and is expected to reproduce universal behavior, such as the temperature dependence of resistivity, for more generic impurity distributions. We now estimate the contribution to resistivity from random impurities scattering magnons via the linear coupling Eq. 4.47.

It was shown in [134], for the closely related problem of a nematic quantum critical point in a metal, that the dominant temperature dependence of resistivity comes from impurity scattering of the Landau damped bosons (in our case spin-waves). Moreover, it was shown that the results of the more sophisticated memory matrix formalism could be reproduced by perturbatively computing the effective momentum loss rate by the process equivalent to the imaginary part of the diagram shown in Figure 4.5, in which an incoming electron emits an overdamped boson which loses momentum to the impurites. In this section, we compute the analogous diagram for the NFL described in the main text.

Evaluating the diagram shown in Figure 4.5 gives:

$$\begin{aligned}\Sigma_{\text{tr}}(\omega) &\approx h_0^2 \int d\Omega dq_\perp dq_{||} (1 - \cos\theta_{\backslash q}) D(\Omega, \boldsymbol{q})^2 G(\omega + \Omega, \mathbf{q}) \\ &\underbrace{\approx}_{\int dq_\perp} h_0^2 \int d\Omega dq_\parallel \left[q_\parallel^2 \times i \ \text{sgn}(\omega + \Omega) \frac{q_\parallel^2}{(|\Omega| + |q_\parallel|^3)^2} \right]\end{aligned}$$

$$\approx i h_0^2 \ \mathrm{sgn}(\omega) \ |\omega|^{2/3}. \tag{4.50}$$

Here, as is typical for the computation of transport scattering rates (see also [134]), we have included a factor of $(1-\cos\theta_{\boldsymbol{q}}) \approx (q_\parallel/k_F)^2$ to appropriately weigh small angle scattering that does not substantially change the electron momentum. Analytically continuing to retarded frequency $i\omega \to \omega + i0^+$ and trading the low frequency cutoff ω for temperature T gives the temperature dependence $\rho(T)_{\mathrm{NFL}} \sim T^{2/3}$ quoted in the main text.

Imry-Ma Scale

We next review the Imry-Ma estimate for the disorder energy scale. Consider a region of linear size L. We estimate the RMS value of the field energy as

$$\delta E_{RMS}^2 \approx \overline{\left[\int d^2 r h(\boldsymbol{r})\phi(\boldsymbol{r})\right]^2} \approx (M_0 h_0)^2 L^d, \tag{4.51}$$

setting $\overline{\phi^2(\boldsymbol{r})} \approx M_0^2$. The spin-gradient energy cost is $(M_0 c)^2 L^{d-2}$. The random field energy dominates at long length scales, while the stiffness cost dominates at short length scales. Setting them equal gives an estimate for the scale L_{IM} at which the magnetization transitions from ordered to disordered due to the impurities,

$$L_{\mathrm{IM}}^{2-\frac{d}{2}} \sim \frac{M_0 c^2}{h_0}, \tag{4.52}$$

which gives (in $d = 2$) $L_{\mathrm{IM}} \sim (M_0 c^2)/h_0$. Substituting for h_0, this results in

$$L_{\mathrm{IM}} = (c^2 \varepsilon_{\mathrm{so}})/(\sqrt{\rho_{\mathrm{imp}}}\lambda_0^2). \tag{4.53}$$

The NFL physics described in the above text occurs in the intermediate temperature range $E_{\mathrm{LD}} \gg T \gg E_{\mathrm{IM}}$ over which the spin-wave dynamics are dominated by Landau damping from the electrons, rather than the the disorder pinning, where we define $E_{\mathrm{IM}} = c/L_{\mathrm{IM}}$ (which we can view as the mass gap acquired by the Goldstone bosons). In order to observe this physics over a broad range of energies, we require $E_{\mathrm{LD}}/E_{\mathrm{IM}} \gg 1$. Using Eq. 4.28, noting $M_0 c \approx T_M$ (the magnetic transition temperature), and approximating $\rho_{\mathrm{imp}} = \ell_{\mathrm{MF}}^{-2}$ (where ℓ_{MF} is the elastic mean-free path related to the elastic scattering time by $\tau = \ell_{\mathrm{MF}}/v_F$), we obtain

$$\frac{E_{\mathrm{IM}}}{E_{\mathrm{LD}}} \sim \left(\frac{\lambda_0 M_0}{\varepsilon_{\mathrm{so}}}\right)\sqrt{\frac{E_F}{T_M}}(E_F\tau)^{-1}. \tag{4.54}$$

These quantities are highly material- and realization-dependent, but as a specific example we may consider a scenario in which a spin orbit coupled metal, such as the giant Rashba

state found in Bi/Ag(111) surface alloys [123, 125, 124, 126], is coupled by proximity to a ferromagnetic insulator (such as EuO [130]). Here, we estimate $T_M \approx 100\text{K}$, $\varepsilon_{\text{so}} \approx E_F \approx 1\text{eV}$, and exchange energy $\lambda_0 M_0 \approx 0.5\text{eV}$ [136]. In a clean metal $E_F\tau$ can be as large as $10^2 - 10^3$, giving $E_{\text{LD}}/E_{\text{IM}} \approx 10 - 100$, indicating a moderate regime over which NFL physics may be observed. We expect this regime to be even more accessible for semiconductor heterostructure based implementations, which can exhibit orders of magnitude longer mean-free paths.

Chapter 5

A Mechanical Analogue of Topological Nodal Semimetals

There has been immense interest in recent years in the properties of electronic systems protected by topology [137]. Robust zero-energy surface states are one manifestation of this, which can be understood through the bulk-boundary correspondence. The latter dictates the appearance of protected gapless excitations at the boundary between two systems with differing values in a topological invariant computed in the bulk. Within topological band theory, such invariants are associated with the occupied Bloch bands of electrons.

The underlying mathematical ideas originate in topology and do not necessarily require a quantum mechanical setting. One may wonder, therefore, whether topologically protected excitations may arise in other domains. Curiously, certain mechanical systems, consisting of lattices of masses coupled by central-force springs, were observed to host boundary-localized zero-energy modes which appeared to be robust [138]. The lattices were *isostatic*, where the number of degrees of freedom and constraints are just balanced and the system is on the edge of mechanical instability. In 2014 [139], Kane and Lubensky discovered that indeed, such lattices can host vibrational modes whose origin is rooted in topology. Furthermore, they identified a relationship between topological protection in the mechanical and free fermion settings. Kane and Lubensky's work initiated a new direction of inquiry, which we refer to as *topological mechanics*, and constitutes the backdrop of this chapter.

Why should a classical problem of springs and masses have any relationship to the topological band theory of electrons? Mechanical systems are governed by Newton's laws, and their dynamics is determined by the spectrum of the dynamical matrix D. As we will see, this matrix is positive semidefinite, $D = R^T R$, and is effectively the "square" of a matrix R which arises naturally in the statement of the spring-mass problem. A single-particle Hamiltonian for fermions has no such positivity constraints, but the square of its energy spectrum will be positive semidefinite. It seems plausible, therefore, that one might use R and R^T to construct a free fermion Hamiltonian. This will indeed be the case, and the Hamiltonian will fall into a class which can exhibit topologically nontrivial properties. We will elaborate on this further in discussing a subset of Kane and Lubensky's work [139] in Section 5.1.

Restricting entirely to the quantum mechanical setting, there is already a sense in which some problems can be viewed as the "square" of another. For instance, the single-particle Hamiltonian for bosons is required to be positive semidefinite due to stability. Elements of this idea have been used before in connecting bosonic and fermionic problems [140, 141]. However, the connection between free fermion Hamiltonians and normal modes of a spring-mass network is a bit more direct, because the factorization of the matrix D into two pieces, R and R^T, already originates rather naturally in the problem definition.

Kane and Lubensky address the origin of robust mechanical modes in systems with a gapped spectrum in the bulk.[1] The mechanical systems which they treat in one dimension can be viewed as analogues of topological insulators. The nontrivial topological properties manifest as zero-frequency modes or states of self-stress (to be defined in Section 5.1) localized at boundaries [139] or defects [142]. Research in topologically protected electronic systems has uncovered phases that extend beyond topological insulators. For instance, topological nodal semimetals (TNS) feature gapless bulk nodes protected by nontrivial band topology and interesting surface Fermi arcs [143]. Could analogues of these also exist in the classical, mechanical setting? Identifying mechanical models with topologically protected *bulk*, rather than edge, gaplessness is a natural step forward. In this chapter, we discuss our work in constructing the first mechanical model that is a TNS analogue [144].

Beginning in Section 5.2, we introduce our model consisting of pinned, periodic spring-mass networks of a particular parametrization.[2] The pinning gaps out the acoustic phonon modes arising from broken translation symmetry. We show that a bulk node with $\omega(\boldsymbol{k}_c) = 0$, with wavevector $\boldsymbol{k}_c$, can in fact appear without fine-tuning. The wavevector $\boldsymbol{k}_c$ can be adjusted in a simple way in the mechanical model. To demonstrate the root of these bulk nodes in topology, we analyze the corresponding fermionic TNS and the relevant topological invariants. While previous works have demonstrated the construction of TNS analogues in bosonic systems, such as photonic crystals [145], acoustic systems [146], and even spring-mass models [147], we stress that those associated band touchings occur at nonzero frequencies. This is physically quite different from the protected bulk modes that appear in our model, which occur at zero energy.

5.1 Introduction to Topological Mechanics

A mechanical system of coupled springs and masses can be described as follows. Extended springs give rise to a potential energy

$$U = \frac{1}{2}\kappa \sum_{m=1}^{N_b} s_m^2, \tag{5.1}$$

[1] Gapless acoustic modes can safely be ignored. It is clear that their origin lies in broken translation symmetry, and they can be gapped out without affecting the topological properties of the model.

[2] We will interchangeably refer to our construction as a phonon model. While the latter suggests a more quantum mechanical interpretation, the difference between these will not be relevant to our primary discussion.

where s_m is the extension of the m-th spring and the sum runs over all N_b bonds in the lattice. The scalar spring extensions $\{s_m\}$ are functions of the mass displacements $\{x_i\}$, which for a lattice of N sites in d dimensions runs over dN components. For convenience, we set all the masses and spring constant κ to unity unless otherwise specified. Within the harmonic approximation, the extensions can be expanded to linear order in the mass displacements, $\boldsymbol{S} = R\boldsymbol{X} + \mathcal{O}(\boldsymbol{X}^2)$, where $\boldsymbol{X}$ and $\boldsymbol{S}$ are dN and N_b dimensional vectors, respectively, aggregating the displacements and extensions. The potential energy can be rewritten,

$$U = \frac{1}{2}\boldsymbol{X}^T R^T R \boldsymbol{X}. \tag{5.2}$$

An additional useful relationship is the one between forces $\boldsymbol{F}$ on the masses and spring tensions $\boldsymbol{T}$, which are related by the transpose of R, $\boldsymbol{F} = R^T\boldsymbol{T}$.

We will primarily be interested in isostatic lattices, as in [139]. These are models where the number of bonds N_b is equal to the number of degrees of freedom, dN. As an example, lattices with coordination number $z = 2d$ will be isostatic; this includes the square and kagome lattices in two dimensions and the cubic and pyrochlore in three dimensions. In the isostatic case, R will be a square matrix.

An application of Newton's second law yields $\ddot{\boldsymbol{X}} = -R^T R\boldsymbol{X}$, identifying $D = R^T R$ as the real-space dynamical matrix. The phonon modes are solutions to the eigenvalue problem $D\xi_i = R^T R\xi_i = \omega_i^2\xi$, where ω_i is the eigenfrequency of the i^{th} mode with $i = 1, \ldots, dN$.

Displacements that do not stretch any springs satisfy $R\boldsymbol{X} = 0$ and hence are parameterized by the kernel of R. Such modes do not cost any energy: they are zero-energy modes. However, they are not the only interesting mechanical vibrations. A lattice may also give rise to states of self-stress, configurations in which the springs are stretched or compressed but there are no net forces on the masses, $R^T\boldsymbol{T} = 0$. The self-stress modes are therefore described by the kernel of R^T.

Bringing these together gives rise to a simple but powerful relation, first studied by Maxwell [148] and later generalized by Calladine [149]. It amounts to a combined application of the rank-nullity theorem to the matrices R and R^T to yield

$$\nu \equiv N_0 - N_{ss} = dN - N_b. \tag{5.3}$$

N_0 and N_{ss} denote the number of zero modes and states of self-stress, respectively. ν denotes the index of R^T, which is defined as $\nu \equiv$ dim ker $R -$ dim ker R^T, the difference in the dimensionality of the two kernels. The generalized Maxwell relation Eq. 5.3, valid for infinitesimal distortations, states that the difference in the count of zero modes and self-stress states is determined by the balance between the number of sites and bonds.

The generalized Maxwell relation originates from a global count over the entire lattice. While this can help in identifying the number of zero modes, it does not pinpoint scenarios in which the vibrational modes are protected by topology. One of the ingenious observations in Kane and Lubensky's work [139] is that some properties of the dynamical matrix $D = R^T R$

can be understood by factoring, or taking the "square root," of the mechanical problem and introducing the Hamiltonian

$$\mathcal{H} = \begin{pmatrix} 0 & R^T \\ R & 0 \end{pmatrix}. \tag{5.4}$$

The square of $\mathcal{H}$ reveals that the spectrum of $\mathcal{H}$ is related to that of D. However, the fermionic zero-energy modes of $\mathcal{H}$ will include both the kernel of R and R^T, and therefore both the zero-energy modes and the states of self-stress of the mechanical problem. The two types are distinguished in the fermionic setting by their eigenvalue under the matrix $\tau^z = \mathrm{diag}(1_{dN}, -1_{N_b})$.

The significance of Eq. 5.4 is that $\mathcal{H}$ can be viewed as a fermionic Hamiltonian and treated within topological band theory. Since it is a real-valued matrix and satisfies $\{\mathcal{H}, \tau^z\} = 0$, it has time-reversal and particle-hole symmetries and falls into symmetry class BDI in the Altland-Zirnbauer classification of free fermion Hamiltonians [150, 9]. In one dimension, such models exhibit an integer topological invariant $n \in \mathbb{Z}$. Kane and Lubensky used this to dissect a *local* version of the generalized Maxwell relation. They consider the index for a region S embedded in a larger system, $\nu^S = N_0^S - N_{ss}^S$, which measures the difference in the number of zero modes and self-stress states *localized in S*. It can be separated into two contributions, $\nu^S = \nu_L^S + \nu_T^S$. ν_L^S is a local count in S dependent on the numbers of springs and masses. On the other hand, ν_T^S has a topological origin and can be computed from topological invariants along one-dimensional cuts. As a consequence, the boundary between models with two different topological invariants will host either topologically protected zero-energy modes or topologically protected states of self-stress.

5.2 Construction of our Model

We turn to the construction of a mechanical analogue of a TNS. We impose periodic boundary conditions as we are interested in the bulk modes. To recount, the mechanical problem is defined by a relationship between spring extensions and mass displacements specified by R. In mapping to the fermionic problem, we will mainly use Majorana fermion operators $\boldsymbol{\chi}, \bar{\boldsymbol{\chi}}$ which satisfy $\{\chi_l, \chi_m\} = \{\bar{\chi}_l, \bar{\chi}_m\} = \delta_{lm}$ and all other anticommutators vanish. Under time-reversal (TR) symmetry, χ ($\bar{\chi}$) is even (odd). Written in a Majorana basis, the fermionic problem is given by matrix $\mathcal{H}_F$ and the associated Hamiltonian H_F [139–141],

$$\mathcal{H}_F = \begin{pmatrix} 0 & -iR^T \\ iR & 0 \end{pmatrix}, \; H_F = \begin{pmatrix} \bar{\boldsymbol{\chi}} & \boldsymbol{\chi} \end{pmatrix} \mathcal{H}_F \begin{pmatrix} \bar{\boldsymbol{\chi}} \\ \boldsymbol{\chi} \end{pmatrix}. \tag{5.5}$$

Consider the phonon spectrum arising from a spring-mass model defined on the square lattice ($d = 2$). For a regular mechanical problem, the form of R is constrained by global continuous translation invariance and spatial symmetries of the underlying lattice. For the square lattice, one simply finds $\omega_j(\boldsymbol{k}) \propto |\sin k_j|$, where $j = 1, 2$ labels the two orthogonal

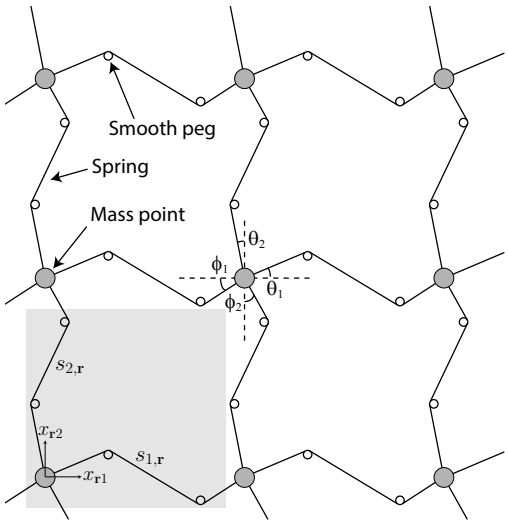

Figure 5.1: A possible realization of the phonon problem. The dependence of the spring extensions on the displacements of the masses can be modified by bending the springs with fixed, smooth pegs which serve as a pinning potential and gap out the acoustic modes. The spring extensions are then characterized by Eq. (5.7) to linear order in mass displacements. The shaded region indicates the unit cell convention adopted.

directions. Although $\omega_j(k_j = 0) = 0$, these nodal lines are not topologically protected as they can be gapped out by explicitly breaking continuous translation symmetry. To expose the potential topological zero modes, will relax these symmetry constraints and assume they are explicitly broken.

Instead, we propose a class of models depicted in Figure 5.1, parameterized by four angles: θ_1, ϕ_1, θ_2, and ϕ_2. The springs have been tweaked with fixed, smooth pegs that serve as an external pinning potential. The form of R is constrained by the geometrical relations between the spring extensions and mass displacements. For a spring connecting the masses at equilibrium positions $\boldsymbol{r} = \boldsymbol{a}$ and $\boldsymbol{b}$, the spring extension should satisfy $|s| \leq |\boldsymbol{x_a}| + |\boldsymbol{x_b}|$. In particular, we assume there is a special spatial direction $\boldsymbol{v} = \cos\theta_a \hat{\boldsymbol{e}}_1 + \sin\theta_a \hat{\boldsymbol{e}}_2$ such that the inequality is saturated for $\boldsymbol{x_a} = |\boldsymbol{x_a}|\boldsymbol{v}$ and $\boldsymbol{x_b} = \boldsymbol{0}$. Equivalently, this implies $\partial_{x_{\boldsymbol{a}1}} s = \cos\theta_a$ and $\partial_{x_{\boldsymbol{a}2}} s = \sin\theta_a$ in the original basis. Assuming a similar dependence of s on $\boldsymbol{x_b}$, characterized by $\boldsymbol{w} = \cos\theta_b \hat{\boldsymbol{e}}_1 + \sin\theta_b \hat{\boldsymbol{e}}_2$, one finds $s = \boldsymbol{v}\cdot\boldsymbol{x_a} + \boldsymbol{w}\cdot\boldsymbol{x_b} + \mathcal{O}(\boldsymbol{x}^2)$.

For a clean system, all springs that are equivalent under lattice translations are characterized by the same parameters and in momentum space one finds the following matrix,

$$R(\boldsymbol{k}) = \begin{pmatrix} v_{11} + w_{11}e^{-ik_1} & v_{12} + w_{12}e^{-ik_1} \\ v_{21} + w_{21}e^{-ik_2} & v_{22} + w_{22}e^{-ik_2} \end{pmatrix}, \tag{5.6}$$

where $\boldsymbol{k} = (k_1, k_2)$ lies in the first Brillouin zone (BZ). v_{lm} (w_{lm}) denotes the m-th component of the vector $\boldsymbol{v}_l$ ($\boldsymbol{w}_l$) relating the spring extension to the displacements $\boldsymbol{x_r}$ and $\boldsymbol{x}_{\boldsymbol{r}+\hat{\boldsymbol{e}}_l}$.

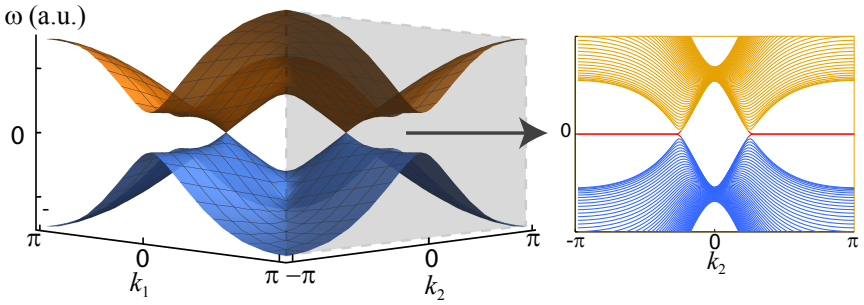

Figure 5.2: Typical spectrum of a 2D TNS hosting a pair of topological nodes at $\omega = 0$ (only the two bands close to $\omega = 0$ are shown). The spectrum is computed for the fermionic problem defined in Eq. 5.5 with R defined in Eqs. (5.6) and (5.7). The parameters $(\theta_1, \phi_1, \theta_2, \phi_2) = (1/4, 0, 1/8, -1/8)\pi$ are used. The inset shows the edge spectrum when open and periodic boundary conditions are enforced for the $\hat{\boldsymbol{e}}_1$ and $\hat{\boldsymbol{e}}_2$ directions respectively, featuring a line of zero modes connecting the projections of the bulk topological nodes onto the surface Brillouin zone.

Enforcing the geometric constraints, the vectors can be parameterized by

$$\begin{aligned} \boldsymbol{v}_1 &= \begin{pmatrix} -\cos\theta_1 \\ -\sin\theta_1 \end{pmatrix}, \ \boldsymbol{v}_2 = \begin{pmatrix} \sin\theta_2 \\ -\cos\theta_2 \end{pmatrix}, \\ \boldsymbol{w}_1 &= \begin{pmatrix} \cos\phi_1 \\ \sin\phi_1 \end{pmatrix}, \ \boldsymbol{w}_2 = \begin{pmatrix} -\sin\phi_2 \\ \cos\phi_2 \end{pmatrix}. \end{aligned} \tag{5.7}$$

The sign convention of the angles is chosen to match the parameterization in Figure 5.1. An example of the gapless bulk nodes is illustrated in Figure 5.2.

Let us analyze the problem in the fermionic variables. The Hamiltonian, as defined in Eq. 5.5 in the Majorana basis, is given by

$$H_F = 2i \sum_{\boldsymbol{r}} \sum_{l,m=1}^{2} \left(v_{lm} \chi^l_{\boldsymbol{r}} \bar{\chi}^m_{\boldsymbol{r}} + w_{lm} \chi^l_{\boldsymbol{r}} \bar{\chi}^m_{\boldsymbol{r}+\hat{\boldsymbol{e}}_l} \right). \tag{5.8}$$

By construction, the fermionic problem is in the symmetry class BDI [150, 9]. It is topologically trivial in 2D but nontrivial in 1D. A topologically nontrivial system can be obtained in 2D by stacking identical 1D chains, as in a weak symmetry-protected topological phase. To this end, we introduce Fourier-transformed variables,

$$\chi^l_{\boldsymbol{r}} = \frac{1}{\sqrt{N_2}} \sum_{k_2} \chi^l_{x_1,k_2} e^{-ik_2 x_2}, \ \chi^l_{x_1,k_2} = \frac{1}{\sqrt{N_2}} \sum_{x_2} \chi^l_{\boldsymbol{r}} e^{ik_2 x_2}, \tag{5.9}$$

where N_j is the number of sites along the $\hat{\boldsymbol{e}}_j$ direction, and $\bar{\chi}^l_{x_1,k_2}$ is similarly defined. Since $(\chi^l_{x_1,k_2})^\dagger = \chi^l_{x_1,-k_2}$ is complex, one can define Majorana operators for $k_2 \in (0, \pi)$,

$$\lambda_{x_1,|k_2|} = \frac{\chi^l_{x_1,k_2} + \chi^l_{x_1,-k_2}}{2}, \quad \eta_{x_1,|k_2|} = \frac{\chi^l_{x_1,k_2} - \chi^l_{x_1,-k_2}}{2i}, \tag{5.10}$$

which are both even under TR. $\bar{\lambda}_{x_1,|k_2|}$ and $\bar{\eta}_{x_1,|k_2|}$, similarly defined for $\bar{\chi}_{x_1,k_2}$, are odd under TR. Since Eq. 5.8 only couples χ to $\bar{\chi}$, upon Fourier transform $H_F(k_2)$ will only couple (λ,η) to $(\bar{\lambda},\bar{\eta})$ and each such 1D system is in the BDI class. While the BDI class is classified by $\mathbb{Z}$ in 1D, the indexes of the 1D chains here are always even: the original lattice translation symmetry along $\hat{\boldsymbol{x}}_2$, reflected as a local $\mathcal{O}(2)$ rotation between $(\lambda_{x_1,|k_2|},\eta_{x_1,|k_2|})$, guarantees that the Majorana zero modes at each edge occur in pairs. This can also be understood from the doubling of Majorana modes for each $k_2 \in (0,\pi)$, as $\chi^l_{x_1,k_2}$ and $\chi^l_{x_1,-k_2}$ are now Hermitian conjugates of each other. Such a property of the system is more manifest by relabeling the operators as

$$c^A_{l,x,k_2} \equiv \chi^l_{x_1,k_2}, \quad c^B_{l,x,k_2} \equiv \bar{\chi}^l_{x_1,k_2}, \ k_2 \in (0,\pi), \tag{5.11}$$

so that the c_l are complex fermions. Eq. 5.8 is then decoupled into a series of 1D fermionic Hamiltonians, each labeled by $k_2 \in (0,\pi)$,

$$\begin{aligned} H_F(k_2) = 2\sum_x \Big(& iv_{11}c^{A\dagger}_{1,x}c^B_{1,x} + iv_{12}c^{A\dagger}_{1,x}c^B_{2,x} + iw_{11}c^{A\dagger}_{1,x}c^B_{1,x+1} + iw_{12}c^{A\dagger}_{1,x}c^B_{2,x+1} \\ & + i(v_{21}+w_{21}e^{-ik_2})c^{A\dagger}_{2,x}c^B_{1,x} + i(v_{22}+w_{22}e^{-ik_2})c^{A\dagger}_{2,x}c^B_{2,x} + h.c.\Big), \end{aligned} \tag{5.12}$$

where we have suppressed the subscript k_2 on the operators. The original symmetry is manifest in this notation as a sublattice (A-B) symmetry.

To characterize these 1D systems, we further Fourier transform on x, which gives

$$H_F(k_2) = 2\sum_{k_1} \begin{pmatrix} \boldsymbol{c}^{A\dagger} & \boldsymbol{c}^{B\dagger} \end{pmatrix} \begin{pmatrix} 0 & iR_{\boldsymbol{k}} \\ -iR^\dagger_{\boldsymbol{k}} & 0 \end{pmatrix} \begin{pmatrix} \boldsymbol{c}^A \\ \boldsymbol{c}^B \end{pmatrix}, \tag{5.13}$$

where the subscript $\boldsymbol{k}$ of the operators is suppressed, $\boldsymbol{c}^A = (c^A_1, c^A_2)^T$, and similarly for $\boldsymbol{c}^B$. The bulk topological invariant of $\mathcal{H}_F(k_2)$ is given by the winding number of $\det(iR_{\boldsymbol{k}})$ as k_1 is varied from $-\pi$ to π [137]. More explicitly, we have

$$\begin{aligned} \det(iR_{\boldsymbol{k}}) =& -\left([\boldsymbol{v}_1 \wedge \boldsymbol{v}_2] + [\boldsymbol{v}_1 \wedge \boldsymbol{w}_2]e^{-ik_2}\right) \\ & -\left([\boldsymbol{w}_1 \wedge \boldsymbol{v}_2] + [\boldsymbol{w}_1 \wedge \boldsymbol{w}_2]e^{-ik_2}\right)e^{-ik_1} \\ \equiv & r_1(k_2) + r_2(k_2)e^{-ik_1}, \end{aligned} \tag{5.14}$$

where $[\boldsymbol{v} \wedge \boldsymbol{w}]$ denotes the component of the wedge product $\boldsymbol{v} \wedge \boldsymbol{w}$ in the $\hat{\boldsymbol{e}}_1 \wedge \hat{\boldsymbol{e}}_2$ direction and $r_1(k_2)$, $r_2(k_2)$ are introduced to simplify the expressions. The winding number $\mathcal{W}_{k_2}$ is determined by the relative magnitude of $|r_1(k_2)|$ and $|r_2(k_2)|$. The case of particular interest is when the winding numbers $\mathcal{W}_{k_2\to 0^+} \neq \mathcal{W}_{k_2\to\pi^-}$, which implies there must be a topological phase transition as k_2 is changed from 0 to π. Such a phase transition occurs when

$$\frac{|r_1(0)r_1(\pi)| + |r_2(0)r_2(\pi)|}{|r_1(0)r_2(\pi)| + |r_2(0)r_1(\pi)|} < 1, \tag{5.15}$$

and when this is satisfied the gap at $E = 0$ must close at some critical quasimomentum $\boldsymbol{k}_c$, giving rise to a topological node. Such nodes in the fermionic picture are reflected in the original bosonic problem as a pair of isolated points $\pm\boldsymbol{k}_c$ at which the phonon frequency vanishes, corresponding to a bulk zero mode in the linearized spectrum.

For a system parameterized as in Eq. 5.7, we have

$$\frac{|r_1(0)r_1(\pi)| + |r_2(0)r_2(\pi)|}{|r_1(0)r_2(\pi)| + |r_2(0)r_1(\pi)|} = \max\left\{|\cos(\theta_1 - \phi_1)|, |\cos(\theta_1 + \phi_1 - \theta_2 - \phi_2)|\right\}, \tag{5.16}$$

which implies that, for general parameters, its linearized phonon spectrum always contains a topologically protected bulk zero mode. Note that if $\theta_1 + \phi_1 - \theta_2 - \phi_2$ is an integer multiple of π, then ω accidentally vanishes on a pair of arcs in the BZ, rendering $\mathcal{H}_F(|k_2|)$ gapless for all $|k_2|$. For generic parameters, the critical quasimomentum is

$$\boldsymbol{k}_c = (\theta_1 - \phi_1)\hat{\boldsymbol{x}} + (\theta_2 - \phi_2)\hat{\boldsymbol{y}}, \tag{5.17}$$

and therefore the quasimomentum associated with the protected bulk zero mode can be adjusted simply by tuning the angles θ_j and ϕ_j.

5.3 Dispersion and Robustness of Zero Modes

Conical phonon dispersion for the smooth peg model

For a stable system, the phonon frequencies satisfy $\omega_\pm^2(\boldsymbol{k}) \geq 0$, where the $\pm$ sign corresponds to the two branches arising from diagonalization of the 2×2 dynamical matrix $D_{\boldsymbol{k}}$. As such $\omega_-^2(\boldsymbol{k})$ attains a global minimum at $\boldsymbol{k}_c$ and therefore $\boldsymbol{\nabla}_{\boldsymbol{k}}\omega_-|_{\boldsymbol{k}_c} = \boldsymbol{0}$. Expanding $\omega_-^2(\boldsymbol{k})$ around the nodal point $\boldsymbol{k}_c$, we have

$$\omega_-^2(\boldsymbol{k}_c + \delta\boldsymbol{k}) \approx \frac{1}{2}\sum_{ij} \left.\frac{\partial^2(\omega_-^2)}{\partial k_i \partial k_j}\right|_{\boldsymbol{k}_c} \delta k_i \delta k_j. \tag{5.18}$$

The phonon speeds around the conical dispersion are given by

$$\frac{1}{2}\left.\left(\frac{\partial^2(\omega_-^2)}{\partial k_i \partial k_j}\right)\right|_{\boldsymbol{k}_c} = \frac{\kappa_1\kappa_2}{2(\kappa_1\mathcal{S}_1^2 + \kappa_2\mathcal{S}_2^2)} \begin{pmatrix} \mathcal{S}_2^2 & \mathcal{S}_1\mathcal{S}_2\mathcal{C}_\delta \\ \mathcal{S}_1\mathcal{S}_2\mathcal{C}_\delta & \mathcal{S}_1^2 \end{pmatrix}, \tag{5.19}$$

where we let $\mathcal{S}_j = \sin k_{cj}$ with $k_{cj} = \theta_j - \phi_j$ for $j = 1, 2$, and $\mathcal{S}_\delta = \sin\delta$, $\mathcal{C}_\delta = \cos\delta$ with $\delta = \theta_1 + \phi_1 - \theta_2 - \phi_2$. The characteristic speeds around the nodal point are therefore given by

$$c_\pm^2 = \frac{\kappa_1\kappa_2(\mathcal{S}_1^2 + \mathcal{S}_2^2)}{4(\kappa_1\mathcal{S}_1^2 + \kappa_2\mathcal{S}_2^2)} \left(1 \pm \sqrt{1 - \left(\frac{2\mathcal{S}_1\mathcal{S}_2\mathcal{S}_\delta}{\mathcal{S}_1^2 + \mathcal{S}_2^2}\right)^2}\right). \tag{5.20}$$

It is clear that when $\delta = 0$, we have $c_- = 0$, corresponding to the softening of the phonon mode due to the line node; when $\delta = \pi/2$ and $\mathcal{S}_1^2 = \mathcal{S}_2^2$, we have $c_+ = c_-$ and this gives an isotropic conical dispersion (Figure 5.3).

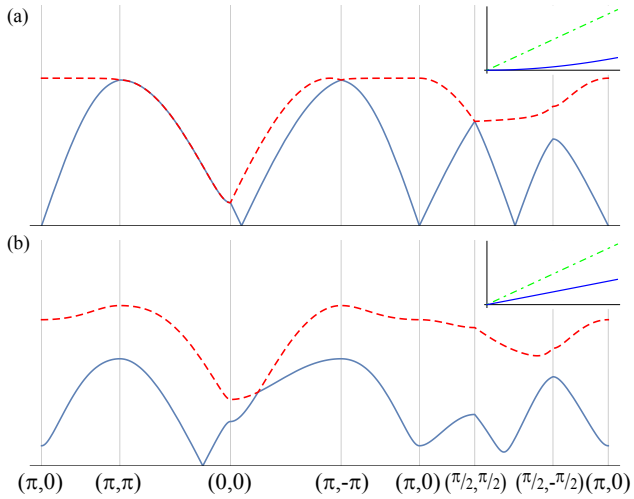

Figure 5.3: Linearized phonon spectrum for the smooth peg model along different paths in the 2D BZ. The insets show the dispersion of the two independent phonon modes around the critical quasimomentum $\boldsymbol{k}_c$. We have set $m = \kappa_1 = \kappa_2 = 1$. (a) The parameters $(\theta_1, \phi_1, \theta_2, \phi_2) = (0.1, 0.2, 0.2, 0.1)\pi$ are used. As such, $\theta_1 + \phi_1 - \theta_2 - \phi_2 = 0$, which gives rise to an accidental vanishing of ω along a pair of arcs in BZ. This is seen in the vanishing of ω at multiple values of $\boldsymbol{k}$ as well as the existence of a quadratic phonon mode around $\boldsymbol{k}_c$. (b) The parameters $(\theta_1, \phi_1, \theta_2, \phi_2) = (1/4, 0, 1/8, -1/8)\pi$ are used (same as Figure 5.2), which corresponds to the generic case in which the linearized phonon spectrum contains a pair of isolated bulk nodal points at $\pm\boldsymbol{k}_c$ with conical dispersion around them.

Robustness

Since the two topological nodes located at $\pm\boldsymbol{k}_c \neq \boldsymbol{0}$ are isolated in momentum space, they are robust, in the fermionic picture, against small perturbations respecting the symmetry. This implies the phonon analogue is robust against weak arbitrary perturbations to the rigidity matrix R, accommodating all the natural perturbations in a spring-mass model. To test this, we study the effect of disorder. We add small random perturbations to the parameters at each site and evaluate the disorder-averaged lowest phonon frequency found by numerically diagonalizing the linearized dynamical matrix. The robustness is demonstrated in the finite-size scaling of Figure 5.4. The sharp dips at $N = 40^2$ and 80^2 originate from the commensuration between the finite momentum mesh and $\boldsymbol{k}_c = \pm(1/4, 1/4)\pi$. In the presence of disorder, the quasimomentum ceases to be a good quantum number, but the bulk zero mode remains, as demonstrated by the decrease of $\langle\omega^2_{min}\rangle$ as system size increases.

With disorder, however, one can reasonably question whether the zero mode observed is really an extended bulk mode or corresponds to local "rattlers." In Figure 5.5, we plot the disorder average of the variance of the center-of-mass for the state found. The various curves with different disorder strengths collapse to the disorder-free one, indicating the mode

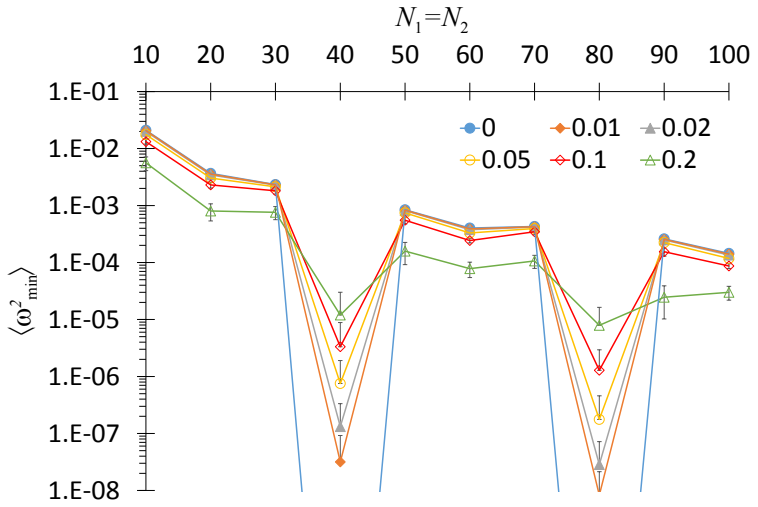

Figure 5.4: Finite-size scaling of the lowest eigenvalue of the disordered dynamical matrix. The linearized dynamical matrix for systems with size $N = N_1 N_2$ and site-dependent couplings is numerically diagonalized to find the smallest eigenvalue ω^2_{min}. The clean system is defined by the same set of parameters used in Figure 5.2. Disorder is incorporated by adding to each parameter at each site a small, independent deviation drawn from a normal distribution with standard deviation σ (κ and m are kept nonnegative by taking absolute values). For each σ, the mean value $\langle\omega^2_{\text{min}}\rangle$ is obtained from 200 disorder realizations. Error bars represent standard deviation in the disorder averages, and solid lines are guides for the eye.

remains extended in nature for the disorder strengths considered.

Since the extended soft modes demonstrated here are protected by the topological properties of the linearized problem, one expects these modes to be only infinitesimal instead of finite. In addition, when the spring-mass description is only a model for a more general system, natural perturbations like the inclusion of small further neighbor couplings correspond to perturbations to the dynamical matrix instead of the rigidity matrix. Such perturbations can render the problem at hand nonisostatic and completely alter the structure of the analysis. The topological protection of the modes is generally lost when confronted with such perturbations. Therefore, it is important to distinguish between the usefulness of this mapping when the problem is interpreted in a mechanical context, as done here, where local isostaticity is a binary question, as opposed to a quantum mechanical problem obtained after quantization, for which local isostaticity may only be an approximation [151].

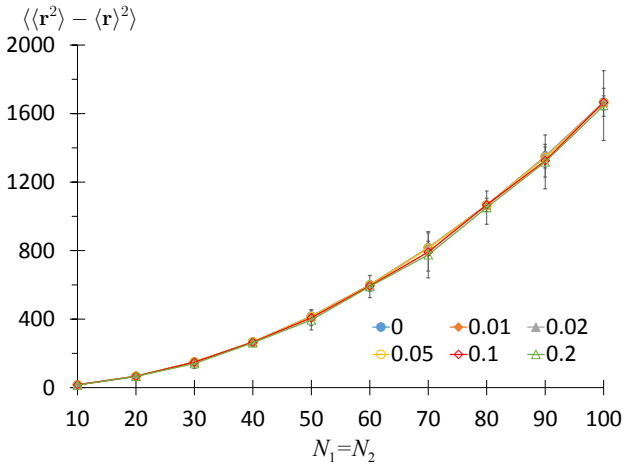

Figure 5.5: Disorder average of the spatial profile of the lowest-frequency mode. Error bars indicate standard deviation from the disorder averaging.

5.4 An Alternative Model

Having analyzed a simple example model in detail, we provide here an alternative model that is both more realistic and also exhibits a richer phase diagram. Rather than connecting adjacent mass points by springs sliding over smooth pegs, we connect them via pinned, rigid rotors similar to those discussed in [139] (Figure 5.6(a)). The term "rotor" refers to a mass point restricted to rotate on a circle by a rigid rod of negligible mass. Each rotor introduces one extra degree-of-freedom together with one extra spring. Altogether, the balance between the number of degrees of freedom and constraints is maintained, and isostaticity is preserved.

Each rotor introduced can be characterized by four parameters: mass m, radius r of the circle it sweeps out, and the coordinate (a, b) of the pinning point relative to the origin of the unit cell. While these parameters can be different for the two rotors in the unit cell, for simplicity we characterize them by the same set of parameter (m, r, a, b) (see Figure 5.6(a)). In particular, we set the mass m to be the same as that of the mass points, the spring constants to all be the same value κ, and the lattice constant to 1. As such, there are still two system parameters: θ_0 and ϕ_0, which characterize the tilt of the rotors with respect to the coordinate axes at equilibrium. The equilibrium lengths of the springs (assuming no prestress), ℓ_{lm}, can then be written in terms of these parameters:

$$\begin{aligned} \ell_{11} &= \sqrt{(b + r\cos\theta_0)^2 + (a + r\sin\theta_0)^2}, \\ \ell_{12} &= \sqrt{(b + r\cos\theta_0)^2 + (1 - a - r\sin\theta_0)^2}, \end{aligned} \tag{5.21}$$

and ℓ_{21}, ℓ_{22} take the same form as ℓ_{11}, ℓ_{12} but with $\theta_0 \to \phi_0$.

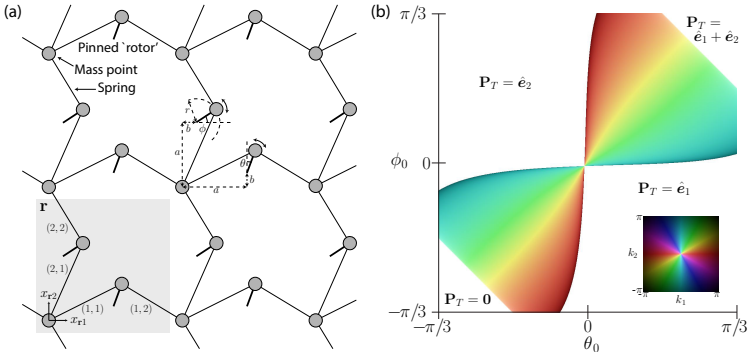

Figure 5.6: An alternative model in which the smooth pegs are replaced by pinned rotors, which preserves isostaticity. (a) Schematic of the model indicating the different parameters. The shaded region indicates the choice of the unit cell, and each spring in the cell is labeled by a pair of numbers (l, m). (b) Example phase diagram with $a = 0.4$, $b = -0.15$, $r = 0.1$ and $\theta_0,\ \phi_0 \in [-\pi/3, \pi/3]$. The colored region corresponds to the TNS phase, with the color (inset) encoding the value of $\pm\boldsymbol{k}_c$. The white regions correspond to a gapped phonon spectrum, which can still have different topological polarization $\boldsymbol{P}_T$.

The energy of the system is

$$E = \frac{m}{2}\sum_{\boldsymbol{r}}\left(\dot{x}^2_{\boldsymbol{r}1} + \dot{x}^2_{\boldsymbol{r}2} + r^2(\dot{\theta}^2_{\boldsymbol{r}} + \dot{\phi}^2_{\boldsymbol{r}})\right) + \frac{\kappa}{2}\sum_{\boldsymbol{r}}\sum_{l,m=1}^{2} s^2_{lm,\boldsymbol{r}}, \tag{5.22}$$

where $x_{l\boldsymbol{r}}$ denotes the displacement in the $\hat{\boldsymbol{e}}_l$ direction for the mass point in the unit cell labeled by $\boldsymbol{r}$, and $s_{lm,\boldsymbol{r}}$ denotes the spring extension of the (l, m)-th spring in the unit cell, as indicated in Figure 5.6(a). As in Section 5.1, we linearize $s_{lm,\boldsymbol{r}}$ and obtain the rigidity matrix via $\boldsymbol{S} = R\boldsymbol{X} + \mathcal{O}(\boldsymbol{X}^2)$, where $\boldsymbol{X}$ is the collective vector for the small fluctuations $\{x_{\boldsymbol{r}1}, x_{\boldsymbol{r}2}, r\delta\theta_{\boldsymbol{r}}, r\delta\phi_{\boldsymbol{r}}\}$ with $\delta\theta_{\boldsymbol{r}} = \theta_{\boldsymbol{r}} - \theta_0$ and $\delta\phi_{\boldsymbol{r}} = \phi_{\boldsymbol{r}} - \theta_0$. After Fourier transform, one finds

$$R_{\boldsymbol{k}} = \ell^{-1}\begin{pmatrix} cccc{-}a{-}r\sin\theta_0 & -b{-}r\cos\theta_0 & a\cos\theta_0{-}b\sin\theta_0 & 0 \\ (1{-}a{-}r\sin\theta_0)e^{-ik_1} & -(b{+}r\cos\theta_0)e^{-ik_1} & -(1{-}a)\cos\theta_0{-}b\sin\theta_0 & 0 \\ -b{-}r\cos\phi_0 & -a{-}r\sin\phi_0 & 0 & a\cos\phi_0{-}b\sin\phi_0 \\ -(b{+}r\cos\phi_0)e^{-ik_2} & (1{-}a{-}r\sin\phi_0)e^{-ik_2} & 0 & -(1{-}a)\cos\phi_0{-}b\sin\phi_0 \end{pmatrix}, \tag{5.23}$$

where $\ell = \mathrm{diag}(\ell_{11}, \ell_{12}, \ell_{21}, \ell_{22})$.

The phase of the system is encoded in the winding numbers of the corresponding fermionic Hamiltonians $\mathcal{H}_F(k_2)$, which we write as

$$\begin{aligned}\det(iR_{\boldsymbol{k}}) &= \left(\tilde{v}_1 + \tilde{v}_2\, e^{-ik_2}\right) + \left(\tilde{w}_1 + \tilde{w}_2\, e^{-ik_2}\right) e^{-ik_1} \\ &\equiv \tilde{r}_1(k_2) + \tilde{r}_2(k_2)\, e^{-ik_1}.\end{aligned} \tag{5.24}$$

The winding number $\mathcal{W}_{k_2}$ is determined by $|\tilde{r}_1(k_2)|/|\tilde{r}_2(k_2)|$. After some algebra, one sees that it is determined by the sign of

$$\begin{aligned}\tilde{f}(k_2) =&(\tilde{v}_1^2+\tilde{v}_2^2-\tilde{w}_1^2-\tilde{w}_2^2)+2(\tilde{v}_1\tilde{v}_2-\tilde{w}_1\tilde{w}_2)\cos(k_2)\\ \equiv&\tilde{f}_1+\tilde{f}_2\cos(k_2),\end{aligned} \tag{5.25}$$

where $\tilde{f}_1$ and $\tilde{f}_2$ are both real. More concretely, $\mathcal{W}_{k_2}=0\ \forall k_2$ if $\tilde{f}_1>|\tilde{f}_2|$; $\mathcal{W}_{k_2}=-1\ \forall k_2$ if $\tilde{f}_1<-|\tilde{f}_2|$; and $\mathcal{W}_{k_2\to 0+}\neq\mathcal{W}_{k_2\to\pi-}$ otherwise, indicating the system is in the TNS phase. For the first two cases, $\mathcal{W}_{k_2}$ is independent of k_2, and it is meaningful to define the integer $n_1=-\mathcal{W}_{k_2}$.

The same analysis can be performed with the role of k_1 and k_2 interchanged, giving the winding number $\mathcal{W}_{k_1}$. When the phonon spectrum is gapped, the topological polarization $\boldsymbol{P}_T=n_1\hat{\boldsymbol{e}}_1+n_2\hat{\boldsymbol{e}}_2$ is well defined [139, 142]. We plot in Figure 5.6(b) an example phase diagram of the system, demonstrating that all the described phases with different topological polarizations can be accessed in this model.

5.5 Conclusion

We have constructed an explicit example of a parameterized family of 2D mechanical models which host a tunable extended vibrational mode in their linearized bulk phonon spectrum. The quasimomentum at which the bulk node exists can be chosen by tuning the parameterization angles, shown in Figure 5.1. It is important to note that if a full phonon spectrum analysis incorporating anharmonicity were to be performed, these gapless modes may be expected to be gapped: the harmonic approximation is required in making the connection to topological properties of free fermion Hamiltonians. However, as long as the harmonic approximation is justified, the real phonon spectrum still contains such bulk soft modes at finite wavevector.

Topological mechanics is still in the early stages of being studied, but it seems plausible that mechanical models with topologically protected vibrational modes – be they in the bulk or the surface – could find a plethora of material and engineering applications. The ability to tune the topological properties rather easily (for instance, in tuning the parameterization angles in our model) is quite advantageous. The topological protection provides fault tolerance, which is highly desirable for applications in which different mechanical parts are coupled to perform nontrivial maneuvers. Models with robust extended soft modes could also be employed as building blocks of more complex structures which need both rigidity for stability and flexibility for functionality [152, 142]. Our construction can also be applied to engineer acoustic or mechanical metamaterials with programmable response to external excitations [153, 154].

Bibliography

1. Bahri, Y. & Vishwanath, A. Detecting Majorana fermions in quasi-one-dimensional topological phases using nonlocal order parameters. *Phys. Rev. B* **89** (2014).
2. Zeng, B., Chen, X., Zhou, D.-L. & Wen, X.-G. Quantum information meets quantum matter from quantum entanglement to topological phase in many-body systems. *ArXiv e-prints.* arXiv: `1508.02595 [cond-mat.str-el]` (2015).
3. Haldane, F. Continuum dynamics of the 1-D Heisenberg antiferromagnet: Identification with the O(3) nonlinear sigma model. *Phys. Lett. A* **93,** 464–468 (1983).
4. Haldane, F. Nonlinear field theory of large-spin Heisenberg antiferromagnets: semiclassically quantized solitons of the one-dimensional easy-axis Néel state. *Phys. Rev. Lett.* **50,** 1153–1156 (1983).
5. Affleck, I., Kennedy, T., Lieb, E. H. & Tasaki, H. Rigorous results on valence-bond ground states in antiferromagnets. *Phys. Rev. Lett.* **59,** 799–802 (1987).
6. Oshikawa, M. Hidden $\mathbb{Z}_2 \times \mathbb{Z}_2$ symmetry in quantum spin chains with arbitrary integer spin. *J. Phys. Condens. Matter* **4,** 7469 (1992).
7. Pollmann, F., Turner, A. M., Berg, E. & Oshikawa, M. Entanglement spectrum of a topological phase in one dimension. *Phys. Rev. B* **81,** 064439 (2010).
8. Pollmann, F., Berg, E., Turner, A. M. & Oshikawa, M. Symmetry protection of topological phases in one-dimensional quantum spin systems. *Phys. Rev. B* **85,** 075125 (2012).
9. Schnyder, A. P., Ryu, S., Furusaki, A. & Ludwig, A. W. W. Classification of topological insulators and superconductors in three spatial dimensions. *Phys. Rev. B* **78,** 195125 (2008).
10. Kitaev, A. Periodic table for topological insulators and superconductors. *ArXiv e-prints.* arXiv: `0901.2686 [cond-mat.mes-hall]` (2009).
11. Fidkowski, L. & Kitaev, A. Effects of interactions on the topological classification of free fermion systems. *Phys. Rev. B* **81,** 134509 (2010).
12. Fidkowski, L. & Kitaev, A. Topological phases of fermions in one dimension. *Phys. Rev. B* **83,** 075103 (2011).

13. Turner, A. M., Pollmann, F. & Berg, E. Topological phases of one-dimensional fermions: an entanglement point of view. *Phys. Rev. B* **83,** 075102 (2011).

14. Burnell, F. J., Chen, X., Fidkowski, L. & Vishwanath, A. Exactly soluble model of a three-dimensional symmetry-protected topological phase of bosons with surface topological order. *Phys. Rev. B* **90,** 245122 (2014).

15. Fidkowski, L., Chen, X. & Vishwanath, A. Non-abelian topological order on the surface of a 3D topological superconductor from an exactly solved model. *Phys. Rev. X* **3,** 041016 (2013).

16. Chen, X., Fidkowski, L. & Vishwanath, A. Symmetry enforced non-abelian topological order at the surface of a topological insulator. *Phys. Rev. B* **89,** 165132 (2014).

17. Wang, C. & Senthil, T. Boson topological insulators: a window into highly entangled quantum phases. *Phys. Rev. B* **87,** 235122 (2013).

18. Wang, C., Potter, A. C. & Senthil, T. Gapped symmetry-preserving surface-state for the electron topological insulator. *Phys. Rev. B* **88,** 115137 (2013).

19. Chen, X., Gu, Z.-C. & Wen, X.-G. Classification of gapped symmetric phases in one-dimensional spin systems. *Phys. Rev. B* **83,** 035107 (2011).

20. Chen, X., Gu, Z.-C. & Wen, X.-G. Complete classification of one-dimensional gapped quantum phases in interacting spin systems. *Phys. Rev. B* **84,** 235128 (2011).

21. Chen, X., Gu, Z.-C., Liu, Z.-X. & Wen, X.-G. Symmetry protected topological orders and the group cohomology of their symmetry group. *Phys. Rev. B* **87,** 155114 (2013).

22. Chen, X., Gu, Z.-C., Liu, Z.-X. & Wen, X.-G. Symmetry protected topological orders in interacting bosonic systems. *Science* **338,** 1604–1606 (2012).

23. Schuch, N., Perez-Garcia, D. & Cirac, I. Classifying quantum phases using matrix product states and projected entangled pair states. *Phys. Rev. B* **84,** 165139 (2011).

24. Gu, Z.-C. & Wen, X.-G. Symmetry-protected topological orders for interacting fermions: fermionic topological nonlinear σ models and a special group supercohomology theory. *Phys. Rev. B* **90,** 115141 (2014).

25. Lu, Y.-M. & Vishwanath, A. Theory and classification of interacting integer topological phases in two dimensions: a Chern-Simons approach. *Phys. Rev. B* **86,** 125119 (2012).

26. Vishwanath, A. & Senthil, T. Physics of three-dimensional bosonic topological insulators: surface-deconfined criticality and quantized magnetoelectric effect. *Phys. Rev. X* **3,** 011016 (2013).

27. Wang, C., Potter, A. C. & Senthil, T. Classification of interacting electronic topological insulators in three dimensions. *Science* **343,** 629–631 (2014).

28. Fannes, M., Nachtergaele, B. & Werner, R. Finitely correlated states on quantum spin chains. *Commun. Math. Phys.* **144,** 443–490 (1992).

29. Vidal, G. Efficient classical simulation of slightly entangled quantum computations. *Phys. Rev. Lett.* **91,** 147902 (2003).

30. Vidal, G. Classical simulation of infinite-size quantum lattice systems in one spatial dimension. *Phys. Rev. Lett.* **98,** 070201 (2007).

31. Verstraete, F., Cirac, J. I., Latorre, J. I., Rico, E. & Wolf, M. M. Renormalization-Group Transformations on Quantum States. *Phys. Rev. Lett.* **94** (2005).

32. Chen, X., Liu, Z.-X. & Wen, X.-G. Two-dimensional symmetry-protected topological orders and their protected gapless edge excitations. *Phys. Rev. B* **84,** 235141 (2011).

33. Den Nijs, M. & Rommelse, K. Preroughening transitions in crystal surfaces and valence-bond phases in quantum spin chains. *Phys. Rev. B* **40,** 4709–4734 (1989).

34. Kennedy, T. & Tasaki, H. Hidden $\mathbb{Z}_2 \times \mathbb{Z}_2$ symmetry breaking in Haldane-gap antiferromagnets. *Phys. Rev. B* **45,** 304–307 (1992).

35. Haegeman, J., Perez-Garcia, D., Cirac, I. & Schuch, N. Order parameter for symmetry-protected phases in one dimension. *Phys. Rev. Lett.* **109,** 050402 (2012).

36. Pollmann, F. & Turner, A. M. Detection of symmetry-protected topological phases in one dimension. *Phys. Rev. B* **86,** 125441 (2012).

37. Zaletel, M. P. Detecting two-dimensional symmetry-protected topological order in a ground-state wave function. *Phys. Rev. B* **90,** 235113 (2014).

38. Perez-Garcia, D., Wolf, M. M., Sanz, M., Verstraete, F. & Cirac, J. I. String order and symmetries in quantum spin lattices. *Phys. Rev. Lett.* **100,** 167202 (2008).

39. Endres, M. *et al.* Observation of correlated particle-hole pairs and string order in low-dimensional Mott insulators. *Science* **334,** 200–203 (2011).

40. Berg, E., Dalla Torre, E. G., Giamarchi, T. & Altman, E. Rise and fall of hidden string order of lattice bosons. *Phys. Rev. B* **77,** 245119 (2008).

41. Dalla Torre, E. G., Berg, E. & Altman, E. Hidden order in 1D Bose insulators. *Phys. Rev. Lett.* **97,** 260401 (2006).

42. Anfuso, F. & Rosch, A. String order and adiabatic continuity of Haldane chains and band insulators. *Phys. Rev. B* **75,** 144420 (2007).

43. Anfuso, F. & Rosch, A. Fragility of string orders. *Phys. Rev. B* **76,** 085124 (2007).

44. Bakr, W., Gillen, J. I., Peng, A., Fölling, S. & Greiner, M. A quantum gas microscope for detecting single atoms in a Hubbard-regime optical lattice. *Nature* **462,** 74–77 (2009).

45. Bakr, W. *et al.* Probing the superfluid-to-Mott insulator transition at the single atom level. *Science* **329,** 547–550 (2010).

46. Alba, E., Fernandez-Gonzalvo, X., Mur-Petit, J., Pachos, J. K. & Garcia-Ripoll, J. J. Seeing topological order in time-of-flight measurements. *Phys. Rev. Lett.* **107,** 235301 (2011).

47. Zhao, E., Bray-Ali, N., Williams, C. J., Spielman, I. B. & Satija, I. I. Chern numbers hiding in time-of-flight images. *Phys. Rev. A* **84,** 063629 (2011).

48. Goldman, N. *et al.* Measuring topology in a laser-coupled honeycomb lattice: from Chern insulators to topological semi-metals. *New J. Phys.* **15,** 013025 (2013).

49. Price, H. M. & Cooper, N. R. Mapping the Berry curvature from semiclassical dynamics in optical lattices. *Phys. Rev. A* **85,** 033620 (2012).

50. Atala, M. *et al.* Direct measurement of the Zak phase in topological Bloch bands. *Nat. Phys.* **9,** 795–800 (2013).

51. Kitaev, A. Unpaired Majorana fermions in quantum wires. *ArXiv e-prints.* eprint: `cond-mat/0010440` (cond-mat.mes-hall) (2001).

52. Asahi, D. & Nagaosa, N. Topological indices, defects, and Majorana fermions in chiral superconductors. *Phys. Rev. B* **86,** 100504 (2012).

53. Chen, X., Lu, Y.-M. & Vishwanath, A. Symmetry-protected topological phases from decorated domain walls. *Nat. Commun.* **5** (2014).

54. Kohmoto, M., den Nijs, M. & Kadanoff, L. P. Hamiltonian studies of the $d = 2$ Ashkin-Teller model. *Phys. Rev. B* **24,** 5229–5241 (1981).

55. Yamanaka, M. & Kohmoto, M. Line of continuously varying criticality in the Ashkin-Teller quantum chain. *Phys. Rev. B* **52,** 1138–1143 (1995).

56. Son, W., Amico, L. & Vedral, V. Topological order in 1D cluster state protected by symmetry. *Quantum Inf. Process.* **11,** 1961–1968 (2012).

57. Anderson, P. W. Absence of diffusion in certain random lattices. *Phys. Rev.* **109,** 1492 (1958).

58. Mott, N. & Twose, W. The theory of impurity conduction. *Adv. Phys.* **10** (1961).

59. Abrahams, E., Anderson, P., Licciardello, D. C & Ramakrishnan, T. Scaling theory of localization: absence of quantum diffusion in two dimensions. *Phys. Rev. Lett.* **42** (1979).

60. Mott, N. Conduction in non-crystalline materials. *Phil. Mag.* **19** (1969).

61. Basko, D., Aliener, I. & Altschuler, B. Metal-insulator transition in a weakly interacting many-electron system with localized single-particle states. *Ann. Phys.* **321** (2006).

62. Nandkishore, R. & Huse, D. A. Many-body localization and thermalization in quantum statistical mechanics. *Annu. Rev. Condens. Matter Phys.* **6** (2015).

63. Deutsch, J. Quantum statistical mechanics in a closed system. *Phys. Rev. A* **43** (1991).

64. Srednicki, M. Chaos and quantum thermalization. *Phys. Rev. E* **50** (1994).

65. Tasaki, H. From quantum dynamics to the canonical distribution: general picture and a rigorous example. *Phys. Rev. Lett.* **80** (1998).

66. Rigol, M., Dunjko, V. & Olshanii, M. Thermalization and its mechanicsm for generic isolated quantum systems. *Nature* **452** (2008).

67. Oganesyan, V. & Huse, D. A. Localization of interacting fermions at high temperature. *Phys. Rev. B* **75** (2007).

68. Pal, A. & Huse, D. A. Many-body localization phase transition. *Phys. Rev. B* **82** (2010).

69. Vosk, R. & Altman, E. Many-body localization in one dimension as a dynamical renormalization group fixed point. *Phys. Rev. Lett.* **110** (2013).

70. Dasgupta, C. & Ma, S.-k. Low-temperature properties of the random Heisenberg antiferromagnetic chain. *Phys. Rev. B* **22** (1980).

71. Bhatt, R. N. & Lee, P. A. Scaling studies of highly disordered spin-1/2 antiferromagnetic systems. *Phys. Rev. Lett.* **48** (1982).

72. Fisher, D. S. Random antiferromagnetic quantum spin chains. *Phys. Rev. B* **50** (1994).

73. Schreiber, M. *et al.* Observation of many-body localization of interacting fermions in a quasirandom optical lattice. *Science* **349** (2015).

74. Huse, D. A., Nandkishore, R. & Oganesyan, V. Phenomenology of fully many-body-localized systems. *Phys. Rev. B* **90** (2014).

75. Serbyn, M., Papic, Z. & Abanin, D. A. Local conservation laws and the structure of the many-body localized states. *Phys. Rev. Lett.* **111** (2013).

76. Swingle, B. A simple model of many-body localization. *ArXiv e-prints.* arXiv: `1307.0507 [cond-mat.dis-nn]` (2013).

77. Chandran, A., Kim, I. H., Vidal, G. & Abanin, D. A. Constructing local integrals of motion in the many-body localized phase. *Phys. Rev. B* **91** (2015).

78. Imbrie, J. Z. On many-body localization for quantum spin chains. *J. Stat. Phys.* **163** (2016).

79. Imbrie, J. Z. Diagonalization and many-body localization for a disordered quantum spin chain. *Phys. Rev. Lett.* **117** (2016).

80. Bahri, Y., Vosk, R., Altman, E. & Vishwanath, A. Localization and topology protected quantum coherence at the edge of hot matter. *Nat. Commun.* **6** (2015).

81. Serbyn, M. *et al.* Interferometeric probes of many-body localization. *Phys. Rev. Lett.* **113** (2014).

82. Bardarson, J. H., Pollmann, F. & Moore, J. E. Unbounded growth of entanglement in models of many-body localization. *Phys. Rev. Lett.* **109** (2012).

83. Bauer, B. & Nayak, C. Area laws in a many-body localized state and its implications for topological order. *J. Stat. Mech* **P09005** (2013).

84. Huse, D. A., Nandkishore, R., Oganesyan, V., Pal, A. & Sondhi, S. L. Localization protected quantum order. *Phys. Rev. B* **88** (2013).

85. Chandran, A., Khemani, V., Laumann, C. R. & Sondhi, S. L. Many-body localization and symmetry-protected topological order. *Phys. Rev. B* **89** (2014).

86. Potter, A. C. & Vishwanath, A. Protection of topological order by symmetry and many-body localization. *ArXiv e-prints.* arXiv: `1506.00592 [cond-mat.dis-nn]` (2015).

87. Kopp, A. & Chakravarty, S. Criticality in correlated quantum matter. *Nat. Phys.* **1** (2005).

88. Smacchia, P. *et al.* Statistical mechanics of the cluster Ising model. *Phys. Rev. A* **84** (2011).

89. Yao, N., Laumann, C. R. & Vishwanath, A. Many-body localization protected quantum state transfer. *ArXiv e-prints.* arXiv: `1508.06995 [quant-ph]` (2015).

90. Landau, L. The theory of a Fermi liquid. *Sov. Phys. JETP* **3** (1957).

91. Landau, L. Oscillations in a Fermi liquid. *Sov. Phys. JETP* **5** (1957).

92. Landau, L. On the theory of the Fermi liquid. *Sov. Phys. JETP* **8** (1959).

93. Bahri, Y. & Potter, A. C. Stable non-Fermi-liquid phase of itinerant spin-orbit coupled ferromagnets. *Phys. Rev. B* **92** (2015).

94. Schofield, A. J. Non-Fermi liquids. *Contemp. Phys.* **40** (1999).

95. Anderson, P. *Basics Notions of Condensed Matter Physics* (Benjamin-Cummings, 1984).

96. Shankar, R. Renormalization group for interacting fermions in $d > 1$. *Phys. A* **177** (1991).

97. Polchinski, J. Effective field theory and the Fermi surface. *ArXiv e-prints.* arXiv: `hep-th/9210046` (1992).

98. Shankar, R. Renormalization-group approach to interacting fermions. *Rev. Mod. Phys.* **66** (1994).

99. Affleck, I. Non-Fermi liquid behavior in Kondo models. *J. Phys. Soc. Jpn.* **74** (2005).

100. Ioffe, L. & Larkin, A. Gapless fermions and gauge fields in dielectrics. *Phys. Rev. B* **39** (1989).

101. Halperin, B., Lee, P. A. & Read, N. Theory of the half-filled Landau level. *Phys. Rev. B* **47** (1993).

102. Lee, S.-S. & Lee, P. A. U(1) gauge theory of the Hubbard model: Spin liquid states and possible application to $\kappa-(\mathrm{BEDT-TTF})_2\mathrm{Cu}_2(\mathrm{CN})_3$. *Phys. Rev. Lett.* **95** (2005).

103. Senthil, T. Theory of a continuous Mott transition in two dimensions. *Phys. Rev. B* **78** (2008).

104. Oganesyan, V., Kivelson, S. A. & Fradkin, E. Quantum theory of a nematic Fermi fluid. *Phys. Rev. B* **64** (2001).

105. Watanabe, H. & Vishwanath, A. Criterion for stability of Goldstone modes and Fermi liquid behavior in a metal with broken symmetry. *Proc. Natl. Acad. Sci. U.S.A.* **111** (2014).

106. Hertz, J. A. Quantum critical phenomena. *Phys. Rev. B* **14** (1976).

107. Abanov, A. & Chubukov, A. Anomalous scaling at the quantum critical point in itinerant antiferromagnets. *Phys. Rev. Lett.* **93** (2004).

108. Metlitski, M. A. & Sachdev, S. Quantum phase transitions of metals in two spatial dimensions. I. Ising-nematic order. *Phys. Rev. B* **82** (2010).

109. Polchinski, J. Low-energy dynamics of the spinon-gauge system. *Nucl. Phys. B* **422** (1994).

110. Altshuler, B., Ioffe, L. & Millis, A. Low-energy properties of fermions with singular interactions. *Phys. Rev. B* **50** (1994).

111. Lee, S.-S. Stability of the U(1) spin liquid with a spinon Fermi surface in 2+1 dimensions. *Phys. Rev. B* **78** (2008).

112. Lee, S.-S. Low-energy effective theory of Fermi surface coupled with U(1) gauge field in 2+1 dimensions. *Phys. Rev. B* **80** (2009).

113. Mross, D. F., McGreevy, J., Liu, H. & Senthil, T. Controlled expansion for certain non-Fermi-liquid metals. *Phys. Rev. B* **82** (2010).

114. Son, D. Superconductivity by long-range color magnetic interaction in high-density quark matter. *Phys. Rev. D* **59** (1999).

115. Metlitski, M. A., Mross, D. F., Sachdev, S. & Senthil, T. Cooper pairing in non-Fermi liquids. *Phys. Rev. B* **91** (2015).

116. Berg, E., Rudner, M. S. & Kivelson, S. A. Electronic liquid crystalline phases in a spin-orbit coupled two-dimensional electron gas. *Phys. Rev. B* **85** (2012).

117. Ruhman, J. & Berg, E. Ferromagnetic and nematic non-Fermi liquids in spin-orbit-coupled two-dimensional Fermi gases. *Phys. Rev. B* **90** (2014).

118. Xu, C. Quantum critical points of helical Fermi liquids. *Phys. Rev. B* **81** (2010).

119. Kim, Y. B., Furusaki, A., Wen, X.-G. & Lee, P. A. Gauge-invariant response functions of fermions coupled to a gauge field. *Phys. Rev. B* **50** (2014).

120. Rech, J., Pepin, C. & Chubukov, A. V. Quantum critical behavior in itinerant electron systems: Eliashberg theory and instability of a ferromagnetic quantum critical point. *Phys. Rev. B* **74** (2006).

121. Dalidovich, D. & Lee, S.-S. Perturbative non-Fermi liquids from dimensional regularization. *Phys. Rev. B* **88** (2013).

122. Sur, S. & Lee, S.-S. Chiral non-Fermi liquids. *Phys. Rev. B* **90** (2014).

123. Ast, C. R. *et al.* Giant spin splitting through surface alloying. *Phys. Rev. Lett.* **98** (2007).

124. Bihlmayer, G, Blügel, S & Chulkov, E. Enhanced Rashba spin-orbit splitting in Bi/Ag (111) and Pb/Ag (111) surface alloys from first principles. *Phys. Rev. B* **75** (2007).

125. Ast, C. R. *et al.* Spin-orbit split two-dimensional electron gas with tunable Rashba and Fermi energy. *Phys. Rev. B* **77** (2008).

126. Meier, F., Dil, H., Lobo-Checa, J., Patthey, L. & Osterwalder, J. Quantitative vectorial spin analysis in angle-resolved photoemission: Bi/Ag(111) and Pb/Ag(111). *Phys. Rev. B* **77** (2008).

127. Lommer, G, Malcher, F & Rossler, U. Spin splitting in semiconductor heterostructures for B→0. *Phys. Rev. Lett.* **60** (1988).

128. Luo, J, Munekata, H, Fang, F. & Stiles, P. Effects of inversion asymmetry on electron energy band structures in GaSb/InAs/GaSb quantum wells. *Phys. Rev. B* **41** (1990).

129. Wei, P. *et al.* Exchange-coupling-induced symmetry breaking in topological insulators. *Phys. Rev. Lett.* **110** (2013).

130. Matthias, B. T., Bozorth, R. M. & Van Vleck, J. H. Ferromagnetic Interaction in EuO. *Phys. Rev. Lett.* **7** (1961).

131. Lee, P. A. & Nagaosa, N. Gauge theory of the normal state of high-T_c superconductors. *Phys. Rev. B* **46** (1992).

132. Kim, Y. B., Lee, P. A. & Wen, X.-G. Quantum Boltzmann equation of composite fermions interacting with a gauge field. *Phys. Rev. B* **52** (1995).

133. Nave, C. P. & Lee, P. A. Transport properties of a spinon Fermi surface coupled to a U(1) gauge field. *Phys. Rev. B* **76** (2007).

134. Hartnoll, S. A., Mahajan, R., Punk, M. & Sachdev, S. Transport near the Ising-nematic quantum critical point of metals in two dimensions. *Phys. Rev. B* **89** (2014).

135. Giamarchi, T. Umklapp process and resistivity in one-dimensional fermion systems. *Phys. Rev. B* **44** (1991).

136. Santos, T. S. & Moodera, J. S. Observation of spin filtering with a ferromagnetic EuO tunnel barrier. *Phys. Rev. B* **69** (2004).

137. *Topological Insulators* (eds Franz, M. & Molenkamp, L.) (Elsevier, 2013).

138. Sun, K., Souslov, A., Mao, X. & Lubensky, T. C. Surface phonons, elastic response, and conformal invariance in twisted kagome lattices. *Proc. Natl. Acad. Sci. U.S.A.* **109,** 12369–12374 (2012).

139. Kane, C. L. & Lubensky, T. C. Topological boundary modes in isostatic lattices. *Nat. Phys.* **10,** 39–45 (2014).

140. Gurarie, V. & Chalker, J. T. Some generic aspects of bosonic excitations in disordered systems. *Phys. Rev. Lett.* **89,** 136801 (2002).

141. Gurarie, V. & Chalker, J. T. Bosonic excitations in random media. *Phys. Rev. B* **68,** 134207 (2003).

142. Paulose, J., Chen, B. G.-g. & Vitelli, V. Topological modes bound to dislocations in mechanical metamaterials. *Nat. Phys.* **11,** 153–156 (2015).

143. Vafek, O. & Vishwanath, A. Dirac fermions in solids: from high-Tc Cuprates and Graphene to topological insulators and Weyl semimetals. *Annu. Rev. Condens. Matter Phys.* **5,** 83–112 (2014).

144. Po, H. C., Bahri, Y. & Vishwanath, A. Phonon analog of topological nodal semimetals. *Phys. Rev. B* **93,** 205158 (2016).

145. Lu, L., Fu, L., Joannopoulos, J. D. & Soljacic, M. Weyl points and line nodes in gyroid photonic crystals. *Nat. Photon.* **7,** 294–299 (2013).

146. Xiao, M., Chen, W.-J., He, W.-Y. & Chan, C. T. Synthetic gauge flux and Weyl points in acoustic systems. *Nat. Phys.* **11,** 920–924 (2015).

147. Wang, Y.-T., Luan, P.-G. & Zhang, S. Coriolis force induced topological order for classical mechanical vibrations. *New J. Phys.* **17,** 073031 (2015).

148. Maxwell, J. C. On the calculation of the equilibrium stiffness of frames. *Phil. Mag.* **27,** 294–299 (1864).

149. Calladine, C. Buckminster Fuller's "Tensegrity" structures and Clerk Maxwell's rules for the construction of stiff frames. *Int. J. Solids. Struct.* **14,** 161–172 (1978).

150. Altland, A. & Zirnbauer, M. R. Nonstandard symmetry classes in mesoscopic normal-superconducting hybrid structures. *Phys. Rev. B* **55,** 1142–1161 (1997).

151. Lawler, M. J. Supersymmetry protected topological phases of isostatic lattices and kagome antiferromagnets. *Phys. Rev. B* **94,** 165101 (2016).

152. Chen, B. G.-g., Upadhyaya, N. & Vitelli, V. Nonlinear conduction via solitons in a topological mechanical insulator. *Proc. Natl. Acad. Sci. U.S.A.* **111,** 13004–13009 (2014).

153. Craster, R. & Guenneau, S. *Acoustic Metamaterials: Negative Refraction, Imaging, Lensing and Cloaking* ISBN: 9789400748132 (Springer, 2012).

154. Florijn, B., Coulais, C. & van Hecke, M. Programmable mechanical metamaterials. *Phys. Rev. Lett.* **113,** 175503 (2014).